Testing lepton flavor universality at future Z factories

Tin Seng Manfred Ho,[1,*] Xu-Hui Jiang,[1,†] Tsz Hong Kwok,[1,‡] Lingfeng Li,[2,3,§] and Tao Liu[1,2,‖]

[1]*Department of Physics, The Hong Kong University of Science and Technology, Hong Kong SAR, People's Republic of China*

[2]*Jockey Club Institute for Advanced Study, The Hong Kong University of Science and Technology, Hong Kong SAR, People's Republic of China*

[3]*Department of Physics, Brown University, Providence, Rhode Island 02912, USA*

(Received 17 January 2023; accepted 5 May 2024; published 24 May 2024)

As one of the hypothetical principles in the Standard Model (SM), lepton flavor universality (LFU) should be tested with a precision as high as possible such that the physics violating this principle can be fully examined. The run of a Z factory at a future e^+e^- collider, such as the Circular Electron-Positron Collider or Future Circular Collider (electron/positron), provides a great opportunity to perform this task because of the large statistics and high reconstruction efficiencies for b hadrons at the Z pole. In this paper, we present a systematic study on the LFU test in future Z factories. The goal is threefold. First, we study the sensitivities of measuring the LFU-violating observables of $b \to c\tau\nu$, i.e., $R_{J/\psi}$, R_{D_s}, $R_{D_s^*}$, and R_{Λ_c}, where τ decays muonically. For this purpose, we develop the strategies for event reconstruction, based on the track information significantly. Second, we explore the sensitivity robustness against detector performance and its potential improvement with the message of event shape or beyond the b-hadron decays. A picture is drawn on the variation of analysis sensitivities with the detector tracking resolution and soft photon detectability, and the impact of Fox-Wolfram moments is studied on the measurement of relevant flavor events. Finally, we interpret the projected sensitivities in the SM effective field theory, by combining the LFU tests of $b \to c\tau\nu$ and the measurements of $b \to s\tau^+\tau^-$ and $b \to s\bar{\nu}\nu$. We show that the limits on the LFU-violating energy scale can be pushed up to $\sim\mathcal{O}(10)$ TeV for $\lesssim\mathcal{O}(1)$ Wilson coefficients at Tera-Z.

DOI: 10.1103/PhysRevD.109.093004

I. INTRODUCTION

Lepton flavor universality (LFU), as one of the hypothetical principles in the Standard Model (SM), requires the leptons of all three generations to couple to gauge bosons universally. Any deviation from the LFU would be an unambiguously signal for physics beyond the SM. So, the LFU should be tested with a precision as high as possible such that the relevant physics can be fully explored.

Given its significance in particle physics, the LFU has been tested in various experiments. One class of such tests involves the $b \to c\tau\nu$ transitions mediated by flavor changing charged current (FCCC). The relevant observables are usually defined as

$$R_{H_c} \equiv \frac{\mathrm{BR}(H_b \to H_c\tau\nu)}{\mathrm{BR}(H_b \to H_c\ell\nu)}, \tag{1.1}$$

where H_b and H_c refer to exclusive b- and c-hadron states, and "BR" denotes branching ratio.[1] Since systematic errors from hadron physics tend to be canceled for the observables defined in such a way, any noteworthy deviation from the SM predictions in statistics may indicate the existence of LFU-violating new physics. In Table I, we have summarized SM predictions and experimental measurements for a set of R_{H_c} observables. Notably, some anomalies in relation to R_{H_c} were reported in the last years. Addressing these anomalies further strengthens the necessity and significance of performing dedicated and more complete LFU measurements.

Future Z factories, namely the Z-pole runs of next-generation e^+e^- colliders [20–22], would provide a great

*tsmho@connect.ust.hk
†xjiangaj@connect.ust.hk
‡thkwokae@connect.ust.hk
§lingfeng_li@brown.edu
‖taoliu@ust.hk

[1]Throughout this paper, we take a notation implicitly including the relevant charge-conjugation mode.

TABLE I. SM prediction and experimental measurement for R_{H_c} observables.

	H_b	H_c	SM prediction[a]	Experimental average
R_D	B^0, $B^\pm$	D^0, $D^\pm$	0.307 [1,2]	0.340 ± 0.030 [3]
R_{D^*}	B^0, $B^\pm$	D^{*0}, $D^{*\pm}$	0.253 [1,2]	0.295 ± 0.014 [3]
$R_{J/\psi}$	B_c	J/ψ	0.289 [4–6]	$0.71 \pm 0.17 \pm 0.18$ [7]
R_{D_s}	B_s	D_s	0.393 [2,8–13]	⋯
$R_{D_s^*}$	B_s	D_s^*	0.303 [2,8,10,13]	⋯
R_{Λ_c}	Λ_b	Λ_c	0.334 [14–18]	0.242 ± 0.076 [19]

[a]The calculation of $R_{J/\psi}$, R_{D_s}, $R_{D_s^*}$, and R_{Λ_c} and the relevant references are shown in the Appendix. The results listed in Table I are slightly different from those in the literature, due to the update of form factor values or the variation of parameter setup.

opportunity for performing this task. Their advantages are generic, manifested as relatively high production rate and reconstruction efficiency of heavy-flavored hadrons.

Consider first the expected b-hadron yields in Belle II, LHCb, and two representative future Z factories (see Table II). At Tera-Z, the statistics of $B^0/\bar{B}^0$ and $B^\pm$ are $\sim 1.2 \times 10^{11}$, about twice of those in Belle II [23]. However, for the heavier $B_s/\bar{B}_s$, the difference in statistics between the Tera-Z and Belle II increases to nearly 2 orders of magnitude. The future Z factories are thus especially suitable for studying flavor physics involving such heavy b hadrons. Unlike Belle II and Z factories, LHCb produces b hadrons mainly through parton-level QCD processes. However, although the expected yields can be even larger at LHCb [24], the event reconstruction efficiency is significantly limited by its noisy data environment.

The boosted kinematics of b hadrons at Z pole and the relatively clean environment for their production represent another set of advantages for the future Z factories to measure the $b \to c\tau\nu$ transitions. The b hadrons produced at Z pole tend to be energetic. This feature weakens the multiple scattering of charged particles, such as the ones from the τ-lepton and c-hadron decays inside the tracker, improving their energy-momentum [26] and motion direction [20,21] resolutions. Moreover, the boosted particles tend to displace more before decay, which may further reduce the uncertainties of reconstructing their decay vertexes. Several recent studies [27–43] have illustrated the potential of the future Z factories in measuring the τ-related physics. Separately, the clean data environment can benefit the measurement of missing energy, a crucial observable for reconstructing the $b \to c\tau\nu$ events. With relatively few particles in final states, negligible pileup effect, and fixed $\sqrt{s}$ value, the measurement of missing energy is expected to be significantly improved at Z pole [29]. In this paper, we will focus on the four representative measurements of R_{H_c} listed in Table I: $R_{J/\psi}$, R_{D_s}, $R_{D_s^*}$, and R_{Λ_c}. Currently, the experimental constraints on these observables are either weak or unavailable.

TABLE II. Expected b-hadron yields in Belle II, LHCb, and the Tera-Z, $10 \times$ Tera-Z factories [25]. There are no statistics on the $B_c^\pm$ and $\Lambda_b/\bar{\Lambda}_b$ productions at Belle II because of the limitation of energy threshold.

	Belle II	LHCb	Tera-Z	$10 \times$ Tera-Z
B^0, $\bar{B}^0$	5.3×10^{10}	6×10^{13}	1.2×10^{11}	1.2×10^{12}
$B^\pm$	5.6×10^{10}	6×10^{13}	1.2×10^{11}	1.2×10^{12}
B_s, $\bar{B}_s$	5.7×10^{8}	2×10^{13}	3.1×10^{10}	3.1×10^{11}
$B_c^\pm$	⋯	4×10^{11}	1.8×10^{8}	1.8×10^{9}
Λ_b, $\bar{\Lambda}_b$	⋯	2×10^{13}	2.5×10^{10}	2.5×10^{11}

From a broader perspective, the LFU can be tested also in the $b \to s\ell_3^+\ell_3^-$ transitions mediated by flavor changing neutral current (FCNC). Here $\ell_3^\pm$ denotes the charged leptons of all three generations. Different from the FCCC, the FCNC in the SM is loop suppressed, with the leading contributions arising from electroweak (EW) penguin and box diagrams. So the width of the FCNC-mediated b-hadron decays is typically smaller than that of the FCCC-mediated ones by a factor $\sim\mathcal{O}(\alpha^2/16\pi^2)$. This fact has motivated the measurements of

$$R_{H_s} \equiv \frac{\mathrm{BR}(H_b \to H_s \mu^+\mu^-)}{\mathrm{BR}(H_b \to H_s e^+ e^-)}, \tag{1.2}$$

where H_b and H_s stand for the exclusive b and s hadronic states and the first two generations of leptons are involved. While the recent LHCb analyses indicated that the values of R_K and R_{K^*}, where $H_b = B$ and $H_s = K^{(*)}$, are compatible with the SM predictions [44], to extend the measurements from R_{H_s} to the $b \to s\tau^+\tau^-$ transitions is intrinsically required, since no known first principle exists which forbids a deviation of the FCNC amplitudes for the third lepton generation from their SM values (see, e.g., [45,46]). Yet, the measurements of the $b \to s\tau^+\tau^-$ transitions are highly challenging, given the complexity of reconstructing multiple-τ events. None of the $b \to s\tau^+\tau^-$ channels have been experimentally observed so far. However, the future Z factories could perform the $b \to s\tau^+\tau^-$ measurements, as explored at detector level recently [42], with a precision sufficient for probing the SM predictions.

In addition to $b \to s\ell_3^+\ell_3^-$, another class of FCNC measurements relevant to the LFU test involves the $b \to s\nu\bar{\nu}$ transitions. These measurements cannot be applied to

probe the LFU violation directly since neutrino flavor is untagged at colliders. However, the inclusive signal rate contributed by the neutrinos of all three flavors is still relevant, which can yield an overall constraint on the possible LFU-violating couplings. Notably, neutrinos do not couple with gluons or photons directly. The $b \to s\nu\bar{\nu}$ processes receive weak radiative corrections only and thus enjoy a lower theoretical uncertainty for their SM predictions. Currently, the upper limits for the $b \to s\nu\bar{\nu}$ branching ratios are $\sim\mathcal{O}(10^{-4}$–$10^{-5})$, not far from their SM predictions [47].

Each of these FCCC and FCNC measurements provides an independent test of LFU in experiments. Any deviation in data from their SM predictions could be a hint or indication of the violation of this principle. Theoretically, the LFU-violating physics could either yield a signal correlating these observables or leave an imprint in only a subset of these measurements. For example, the $SU(2)$ gauge symmetry may relate the $b \to s\nu\bar{\nu}$ amplitudes with those of $b \to c\tau\nu$ or $b \to s\tau\tau$ or both of them. More discussions about these issues can be found in Sec. VII. So the LFU measurements should be performed with a coverage broad enough and a precision as high as possible. The future Z factories allow us to extend the existing measurements to the more challenging ones, which suffer from either a small production rate in Belle II or low reconstruction efficiency at LHCb, of heavy-flavored hadrons. To demonstrate the potential capability of these machines in testing the LFU, in this paper, we will take a sensitivity interpretation in the SM effective field theory (SMEFT), where the SM gauge symmetries are respected. We will focus on a subset of 6D operators which encode the LFU violation arising from the third generation only to converge the discussions. Especially, considering the possible hierarchy between the measurement scale and the new physics scale, the effects of renormalization of the relevant Wilson coefficients will be taken into account.

This paper is organized as follows. In Sec. II, we introduce general strategies for our simulations and analyses. The analysis of measuring $R_{J/\psi}$ is taken in Sec. III, while the ones for measuring $R_{D_s^{(*)}}$ and R_{Λ_c} are performed in Secs. IV and V, respectively. The sensitivity robustness against detector resolution and potential improvements from event shape for these analyses are then explored in Sec. VI. We present the SMEFT interpretations for the projected sensitivities at the future Z factories in Sec. VII and finally conclude in Sec. VIII.

II. STRATEGY FOR EVENT SIMULATION

We use PYTHIA8 [48] to simulate both signal and background events for the R_{H_c} measurements.[2] In each of them, two signal modes are involved, namely, $H_b \to H_c\tau^+\nu_\tau$ and $H_b \to H_c\mu^+\nu_\mu$. The signal events of these two modes contribute as the mutual backgrounds also in their respective measurements. Signal samples are generated via the $Z \to b\bar{b}$ production at the Z pole, forcing the b hadrons (together with H_c) to decay into the relevant states exclusively. These events are then reweighted according to the $d\Gamma/dq^2$ differential cross section obtained in the Appendix to reproduce the correct kinematic distributions. Background samples are generated via the $Z \to b\bar{b}$ process also.

The detector effects are simulated using DELPHES3 [52]. Given that the relative impact on the results is of percent level and hence tiny between the International Large Detector [53] and Innovative Detector for Electron–positron Accelerators concepts [54], we take the former detector profile as our benchmark in the analyses below. Notably, some features, such as particle identification (ID) efficiency and impact-parameter resolution for tracks, are not hard coded in these profiles. As these features may play a crucial role in our analysis, we simulate them with a set of benchmark values and discuss the potential impacts of their variance in Sec. VI A.

One such feature is muon ID. Our study relies on muon tagging significantly. The four R_{H_c} analyses are either based on the three-muon system or requesting at least one tagged muon. However, due to the comparable mass of $\pi^\pm$ with muons and their large multiplicity in hadronic final states [55], the $\pi^\pm$ could be misidentified as muons and yield visible negative impact for the H_b reconstruction. So we will consider this effect in our analysis. A full simulation of particle ID performance is beyond the scope of this study. Instead we approximate the muon mis-ID probability $\epsilon_{\mu\pi}$ to be 1% [55], an optimal value which is expected to be achieved at the Future Circular Collider (electron/positron) [56] and Circular Electron-Positron Collider (CEPC) [20] by the time of their operation. The muon mis-ID by other hadrons is much less significant due to their larger masses and lower multiplicities and hence will not be considered in our simulation. As for the mis-ID between charged hadrons (e.g., π/K, K/p, and π/p), it may bring in fake H_c resonances, yielding a sideband around the physical resonance peak. Its impacts will be evaluated from the current experimental data instead (see the discussions below on "fake H_c backgrounds"). At last, to simulate the effects of finite spatial resolution, we smear the decay vertex of particles by turning on independent and isotropic Gaussian noise in the tracker. Such smearing is also applied to the impact parameter of the muon tracks, which arise from (semi)leptonic hadron and τ decays. We set the overall noise level to be 10 μm, a typical tracker resolution suggested in [20,56].

The background analysis is highly involved for the R_{H_c} measurements. Because of the complexity of the b-hadron decay chains, it is not realistic to make an exhaustive list of the backgrounds, but it is beneficial to understand the general background sources and their characteristics first.

[2]Aiming to set up the benchmarks for measuring lepton flavor universality at future Z factories, we will perform this study based on fast simulations. Alternatively, more sophisticated e^+e^- event generators such as KKMC [49,50] and Whizard [51] can be applied to achieve a higher simulation accuracy. This, however, is beyond the scope of this study and will be left to a refined work in the future.

TABLE III. Estimation of the fake H_c backgrounds. The first column represents the estimated yield ratio of the fake H_c background over the real H_c resonance from the reference studies. The second and third columns are the reconstructed H_c resonance standard deviation values of the reference and our study, respectively. The last one is the estimated yield ratio of the fake H_c over the real H_c resonance contributing to our studies.

H_c	Fake H_c ratio (%)	H_c width$_{\text{Ref}}$ (MeV)	H_c width$_{Z\text{ factory}}$ (MeV)	Estimated (%)
$J/\psi(\to\mu^+\mu^-)$	4.5	9.1 [7]	8.3	$\lesssim$2.3
$D_s^-(\to\phi\pi^-)$	3.8	7.6 [57]	6.1	$\lesssim$3.8
$\Lambda_c^-(\to\bar{p}K^+\pi^-)$	1.5	5.5 [58]	4.5	$\lesssim$0.3

Motivated by this, we classify these backgrounds into five categories: inclusive, cascade, combinatoric, muon mis-ID, and fake-H_c resonance backgrounds.

Inclusive backgrounds. We refer to $H_b \to H_c\tau(\mu)\nu + X$ as "inclusive backgrounds." Here H_b decays semileptonically. X arises from either resonant H_c^* decay or nonresonant contribution. In the simulation, any nonsignal b-hadron events, if containing the $H_c + \mu$ produced via semileptonic b-hadron decays at the truth level, will be recognized as inclusive backgrounds.

Cascade backgrounds. We refer to $H_b \to H_c\tau(\mu)\nu + X$ as "cascade backgrounds." Here H_b decays hadronically. In the simulation, any nonsignal b-hadron events, if containing the $H_c + \mu$ produced not via semileptonic b-hadron decay at truth level, will be recognized as the cascade backgrounds.

Combinatoric backgrounds. We refer to $H_c\tau(\mu)\nu + X$ as "combinatoric backgrounds." Here H_c and $\tau(\mu)$ do not share a parent particle at the truth level. In the simulation, any reconstructed b-hadron events, if containing the $H_c + \mu$ but not identified as the inclusive and cascade backgrounds, will be recognized as the combinatoric backgrounds.

Muon mis-ID backgrounds. We refer to $H_c\mu_\pi + X$ as "muon mis-ID backgrounds." Here μ_π denotes the muon misidentified from pion. In the simulation, any $H_c\pi + X$ events will be recognized as the mis-ID background, weighted by the mis-ID probability $\epsilon_{\mu\pi} = 1\%$ as mentioned above.

Fake H_c backgrounds. We refer to $H_{c,F}\mu + X$ as fake H_c backgrounds. Here $H_{c,F}$ denotes the fake H_c resonance, with the latter decaying as $J/\psi \to \mu^+\mu^-$, $D_s^- \to K^+K^-\pi^-$, or $\Lambda_c^- \to \bar{p}K^+\pi^-$ in this study. These backgrounds represent the chance that the remnants for reconstructing H_c are not from H_c decays at the truth level. In the analysis, they appear as a continuous distribution of the reconstructed m_{H_c}. A good width resolution of resonance is thus essential for suppressing these backgrounds. In practice, the resonance width is determined by the resolution of the tracking system, given $\Gamma_{H_c} \lesssim \mathcal{O}(\text{keV}) \ll \Delta_{\text{track}}$, where Δ_{track} denotes the tracker smearing effect. We can estimate the level of these backgrounds from the relevant LHCb studies [7,57,58]. As summarized in Table III, the rations of the H_c events and the continuous backgrounds in the resonant bin for the reconstructed m_{H_c} are at most a few percent. The reconstructed resonance widths are expected to be further improved at the future Z factories [7,57,58]. Furthermore, the fake H_c background sizes can easily be extrapolated by sideband m_{H_c} distributions. So the effect of this type of background can be safely neglected in R_{H_c} precision projections.

III. MEASUREMENT OF $R_{J/\psi}$

A. Method

To measure $R_{J/\psi}$, we consider the exclusive B_c^+ decays, i.e., $B_c^+ \to J/\psi(\to\mu^+\mu^-)\mu^+\nu_\mu$ and $B_c^+ \to J/\psi(\to\mu^+\mu^-) \times \tau^+(\to\mu^+\nu_\mu\bar{\nu}_\tau)\nu_\tau$, as the signals. Both signal modes contain 3μ in their final states. The schematic of the $B_c^+ \to J/\psi\tau^+\nu_\tau$ process is shown in Fig. 1. The same decay modes have been considered in the $R_{J/\psi}$ measurement at LHCb also [7]. We also show the schematics of several topologies for the universal backgrounds in Fig. 2. Below are a set of cuts applied to preselect such events.

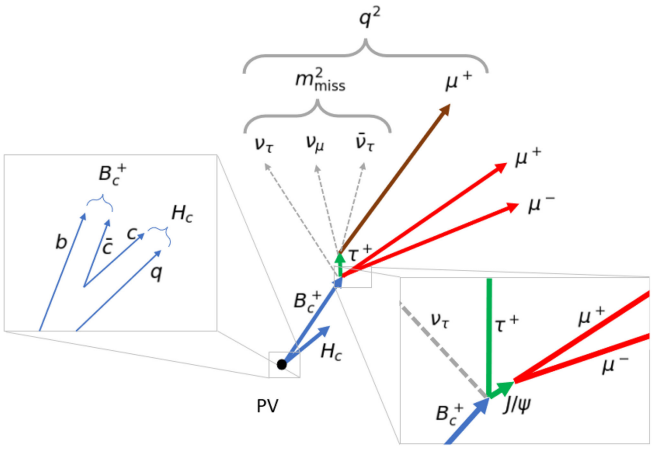

FIG. 1. Schematic of the $B_c^+ \to J/\psi\tau^+\nu_\tau$ process. Since J/ψ is short-lived, its decay vertex can serve as a good approximation of the B_c^+ decay vertex. Additionally, the c quark paired produced with the B_c^+ is hadronized to another c hadron (H_c), which tends to move along with the B_c^+.

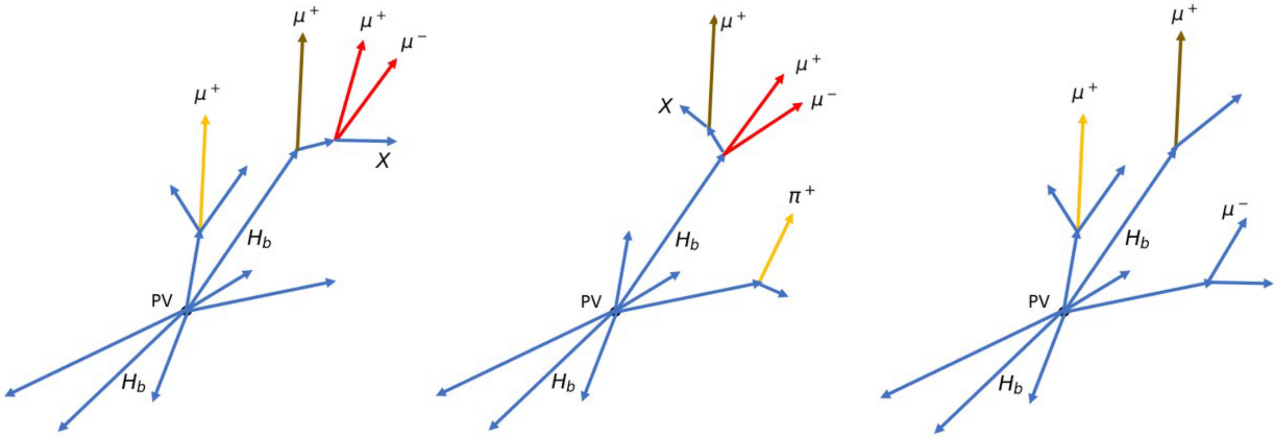

FIG. 2. Schematics of the universal backgrounds in the $R_{J/\psi}$ measurement. Left: the typical topology for the inclusive backgrounds and the combinatoric backgrounds, where B_c^+ is reconstructed combining muons produced by the J/ψ (red), and the unpaired muon from semileptonic H_b decay (brown) or irrelevant particle decay (orange), respectively. Middle: the typical topology for the cascade backgrounds and the Mis-ID backgrounds, where B_c^+ is reconstructed combining the muons decayed from J/ψ (red), and the unpaired muon from intermediate hadron decay (brown) and pion misidentification (orange), respectively. Right: the typical topology for the fake H_c backgrounds, where the muons that do not share a parent particle (brown and orange) are used to reconstruct J/ψ.

(i) The 3μ selection. The events with exactly three muon tracks ($p_T > 0.1$ GeV), with at least two of them sharing the same vertex, are selected.
(ii) The J/ψ selection. Two of the three muons need to be oppositely charged. Their momentum satisfies $|\vec{p}| > 2.5$ GeV. The leading transverse momentum must be > 0.75 GeV, while their total p_T must be > 1 GeV. These two muons form a common vertex, with its distance to the primary vertex (PV) > 0.1 mm. Additionally, these two muons must have an invariant mass with $|m_{\mu^+\mu^-} - m_{J/\psi}| < 27.5$ MeV for them to be considered as the J/ψ decay products.
(iii) The B_c^+ selection. We divide the space into signal and tag hemispheres with a plane perpendicular to the displacement of the reconstructed J/ψ. The J/ψ vertex appears in the signal hemisphere. The unpaired third muon (μ_3) appears in the signal hemisphere also and has $p_T > 0.375$ and $|\vec{p}| > 1.5$ GeV. The 3μ system needs to have an invariant mass smaller than $m_{B_c^+}$.

The Tera-Z yields for the preselected signals and the backgrounds are summarized in Table IV. The requirement of narrow J/ψ and B_c^+ reconstruction excludes most of the backgrounds except the inclusive ones, as expected.

The preselected events are then subjected to the B_c^+ reconstruction. Such a task is highly involved since the signal events contain at least one neutrino. For reconstructing the four-momentum of B_c^+ ($p_{B_c^+}$), we will take several approximations. First, as J/ψ decays promptly, we will use the J/ψ decay vertex to approximate the B_c^+ decay vertex and define its displacement from the PV as the $\vec{p}_{B_c^+}$ direction. Second, we calculate the total energy of the particles inside the signal hemisphere $E_{\rm sig}$ with the relation

$$E_{\rm sig} = \frac{m_{\rm tag}^2 + m_Z^2 - m_{\rm sig}^2}{2m_Z}, \tag{3.1}$$

where $m_{\rm sig}$ and $m_{\rm tag}$ are the invariant masses of visible particles in the signal and tag hemispheres, respectively. This relation is generated by applying the energy- and momentum-conservation conditions to the two-body decay of a Z boson at rest [29]. No missing particles are involved in this case. To calculate $E_{\rm sig}$, we have mimicked these two

TABLE IV. Tera-Z yields for the preselected signals and the backgrounds in the $R_{J/\psi}$ measurement. The preselection criteria are defined in the text.

Channel	Events at Tera-Z	$N(3\mu)$	$N(J/\psi)$	$N(B_c^+)$	Total eff. (%)
$B_c^+ \to J/\psi\tau^+\nu_\tau$	9.83×10^3	6.53×10^3	3.83×10^3	3.08×10^3	31.34
$B_c^+ \to J/\psi\mu^+\nu_\mu$	2.39×10^5	1.63×10^5	9.66×10^4	8.40×10^4	35.13
Inclusive bkg.	1.27×10^4	8.20×10^3	5.29×10^3	3.90×10^3	30.63
Cascade bkg.	1.81×10^4	4.89×10^3	3.32×10^3	1.84×10^3	10.15
Combinatoric bkg.	4.64×10^7	3.93×10^7	2.66×10^7	7.78×10^4	0.17
Mis-ID bkg.	$\epsilon_{\mu\pi} \times 1.45 \times 10^9$	$\epsilon_{\mu\pi} \times 1.03 \times 10^9$	$\epsilon_{\mu\pi} \times 6.96 \times 10^8$	$\epsilon_{\mu\pi} \times 1.10 \times 10^8$	7.61

bodies with the collection of particles in the signal and tag hemispheres and replaced their invariant masses with $m_{\rm sig}$ and $m_{\rm tag}$. Clearly, this relation becomes exact only if no neutrinos have been produced. With this calculation, the B_c^+ energy $E_{B_c^+}$ is reconstructed as

$$E_{B_c^+} = E_{\rm sig} - \sum_{i \in \text{sig-hem}} E_i + E_{J/\psi} + E_{\mu_3}, \qquad (3.2)$$

where the index i goes over all visible particles inside the signal hemisphere. With the direction message of $\vec{p}_{B_c^+}$ and the value of $E_{B_c^+}$, the four-momentum $p_{B_c^+}$ can be completely determined using the B_c^+ on-shell condition. We show the distributions of the reconstructed $E_{B_c^+}$ for the $B_c^+ \to J/\psi\tau^+\nu_\tau$ and $B_c^+ \to J/\psi\mu^+\nu_\mu$ signals and their common backgrounds in Fig. 3. A sharp edge at $m_Z/2$ can be seen for the signal distributions where the $Z \to b\bar{b}$ events tend to be hadronized into two b hadrons only.

With the reconstructed four-momentum of B_c^+, we are able to define two Lorentz-invariant observables,

$$q^2 \equiv (p_{B_c^+} - p_{J/\psi})^2,$$
$$m^2_{\rm miss} \equiv (p_{B_c^+} - p_{J/\psi} - p_{\text{unpaired }\mu})^2. \qquad (3.3)$$

These two observables are visualized in Fig. 1. For the SM events, they measure the mass of off-shell W boson and produced neutrinos, respectively. Similar observables can be defined for the other R_{H_c} measurements. As q^2 and $m^2_{\rm miss}$ receive contributions from more neutrinos for the signal events of $B_c^+ \to J/\psi\tau^+\nu_\tau$, compared to the ones of $B_c^+ \to J/\psi\mu^+\nu_\mu$, their values and variances tend to be bigger in the former case. This feature is important since the signal events of these two modes can serve as the backgrounds mutually in their measurements. Finally, we have the reconstruction errors of q^2 and $m^2_{\rm miss}$: 1.88(1.80) and 1.90(1.61) GeV^2. Here the numbers outside and inside the brackets are for the τ and μ modes, respectively. Other than the reconstructed B_c^+ kinematics, the signal events of the τ and μ modes can be further separated using the message on τ-lepton displacement. The lifetime of the τ lepton is relatively long. It may travel a detectable distance before it decays to other particles. The minimal distance ($S_{\rm SV}$, in millimeters) between the μ_3 track and the secondary vertex (SV) (i.e., the B_c^+ decay vertex) thus can be applied to discriminate the signal events of $B_c^+ \to J/\psi\tau^+\nu_\tau$ from the $B_c^+ \to J/\psi\mu^+\nu_\mu$ ones. We demonstrate these features in Fig. 3.

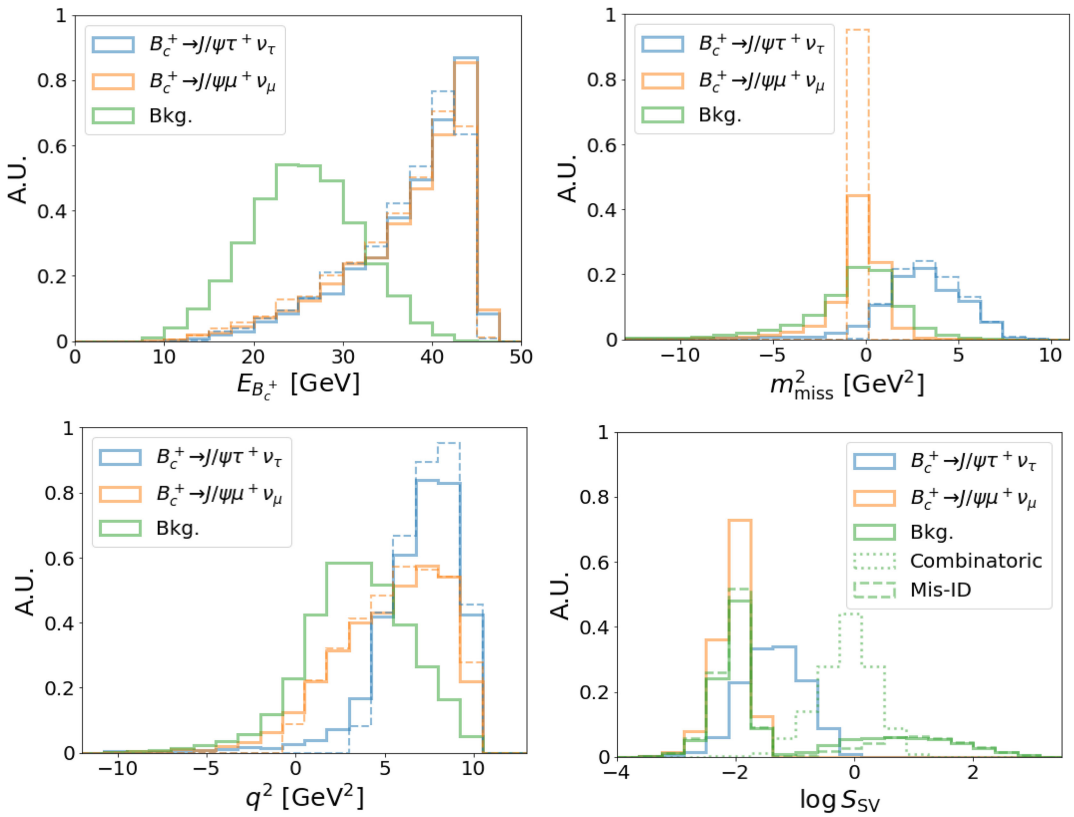

FIG. 3. Distributions of the reconstructed $E_{B_c^+}$, q^2, $m^2_{\rm miss}$, and log $S_{\rm SV}$ in the $R_{J/\psi}$ measurement. The solid and dashed lines represent the simulated and truth-level messages, respectively.

The observables introduced above can also separate the signals of different modes from the universal backgrounds to various extents. To further suppress these backgrounds, we may use the message on the signal b-hadron (B_c^+ here) isolation. Different from the reconstructed background events, the signal B_c^+ mesons tend to be isolated. Thus, we can introduce the isolation observables $I_N(\Omega)$ and $I_T(\Omega)$ to facilitate the selection of the signal events. Here I is the total energy of some specific particles within a cone around the reconstructed momentum of B_c^+. Ω denotes the angular size of this cone. N represents neutral particles such as neutral hadrons (I_H) and photons (I_γ), while T represents tracks that can be either from the PV ($I_{T,\mathrm{PV}}$) or away from the PV ($I_{T,\mathrm{dis}}$). This feature is demonstrated in Fig. 4 with $I_N(0.3\ \mathrm{rad})$. Note that, while these observables can bring in systematic uncertainties via the simulation of hadronization processes, these systematics could be mitigated with Z pole calibrations by utilizing the processes such as $B^+ \to J/\psi K^+$ or $B_c^+ \to J/\psi\pi^+$, where the presence of a distinct resonance accompanied by narrow sidebands will facilitate precise calibrations.

To optimize the sensitivity of measuring $R_{J/\psi}$, we apply the boosted decision tree (BDT) tool in this analysis and the subsequent ones for the $R_{D_s^{(*)}}$ and R_{Λ_c} measurements. We include more observables on the track impact parameter other than the ones discussed above and some observables used in [59] as the BDT discriminators. The BDT classifier is trained in a three-class mode to address its two signal patterns. The full list of the discriminators is summarized below:

(1) Kinematics of the three-muon system:
   (a) Invariant mass $m_{3\mu}$.
   (b) Energy and momentum of the reconstructed J/ψ and the unpaired muon μ_3: $E_{J/\psi}, |\vec{p}_{J/\psi}|, E_{\mu_3}, |\vec{p}_{\mu_3}|$.

(2) Observables of the reconstructed B_c^+:
   (a) Energy and momentum of the reconstructed B_c^+: $E_{B_c^+}$, $|\vec{p}_{B_c^+}|$.
   (b) Lorentz-invariant observables: m^2_{miss}, q^2.

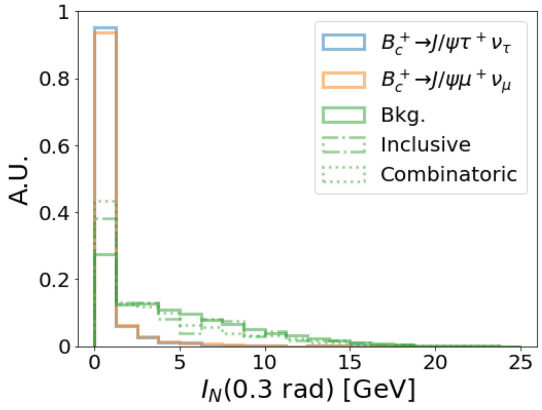

FIG. 4. Distributions of $I_N(0.3\ \mathrm{rad})$ in the $R_{J/\psi}$ measurement.

(3) Vertex information:
   (a) Minimal distance between the B_c^+ (or J/ψ) decay vertex and the μ_3 track (S_{SV}).
   (b) Minimal distance between the μ_3 track and its closest track.
   (c) Minimal distance between the reconstructed J/ψ trajectory and its closest track.
   (d) Distance between the J/ψ decay vertex and the PV.

(4) Isolation observables of B_c^+:
   (a) Neutral particles: $I_N(0.3\ \mathrm{rad})$, $I_N(0.6\ \mathrm{rad})$.
   (b) Neutral hadrons: $I_H(0.3\ \mathrm{rad})$, $I_H(0.6\ \mathrm{rad})$.
   (c) Photons: $I_\gamma(0.3\ \mathrm{rad})$, $I_\gamma(0.6\ \mathrm{rad})$.
   (d) Charged particles: $I_T(0.3\ \mathrm{rad})$, $I_T(0.6\ \mathrm{rad})$.
   (e) Tracks from the PV: $I_{T,\mathrm{PV}}(0.3\ \mathrm{rad})$, $I_{T,\mathrm{PV}}(0.6\ \mathrm{rad})$.
   (f) Tracks not from the PV: $I_{T,\mathrm{dis}}(0.3\ \mathrm{rad})$, $I_{T,\mathrm{dis}}(0.6\ \mathrm{rad})$.

(5) Impact parameter of the tracks in the signal hemisphere:
   (a) Maximum and sum of transverse impact parameters.
   (b) Maximum and sum of longitudinal impact parameters.

(6) Some other discriminators [59]:
   (a) $J/\psi\mu^+$ momentum transverse to the B_c^+ moving direction: $p_\perp(J/\psi\mu^+)$.
   (b) Corrected mass: $m_{\mathrm{corr}} = \sqrt{m^2(J/\psi\mu^+) + p_\perp^2(J/\psi\mu^+)} + p_\perp(J/\psi\mu^+)$.

While this list is relatively long, its comprehensiveness can help us to avoid missing potentially important kinematic variables in the analyses.

B. Results

In Fig. 5, we show the distributions of BDT response in favor of $B_c^+ \to J/\psi\tau^+\nu_\tau$ and $B_c^+ \to J/\psi\mu^+\nu_\mu$ in the $R_{J/\psi}$ measurement. The two classes of signal events also serve as the mutual backgrounds of their measurements. Unless otherwise specified, in this paper the BDT thresholds are always defined to be the ones maximizing the statistical analysis sensitivity. We summarize the event counts in the relevant signal regions in Table V and the expected precisions of measuring $R_{J/\psi}$ at Tera-Z and $10\times$ Tera-Z in Table VI accordingly. Essentially, the precisions of measuring $R_{J/\psi}$ are limited by the relatively low counts of the $B_c^+ \to J/\psi\tau^+\nu_\tau$ events. Signal events are recognized to be of high or low q^2 by comparing their reconstructed q^2 with the 7.15 GeV^2 reference value [7]. As shown in Table VI, in the high q^2 region where a larger $R_{J/\psi}$ has been predicted, a better precision can be achieved compared to the low q^2 region. At last, we point out that the relatively high S/B ratios in all scenarios ensure the robustness of the sensitivity analysis of measuring $R_{J/\psi}$ against the potential systematic uncertainties.

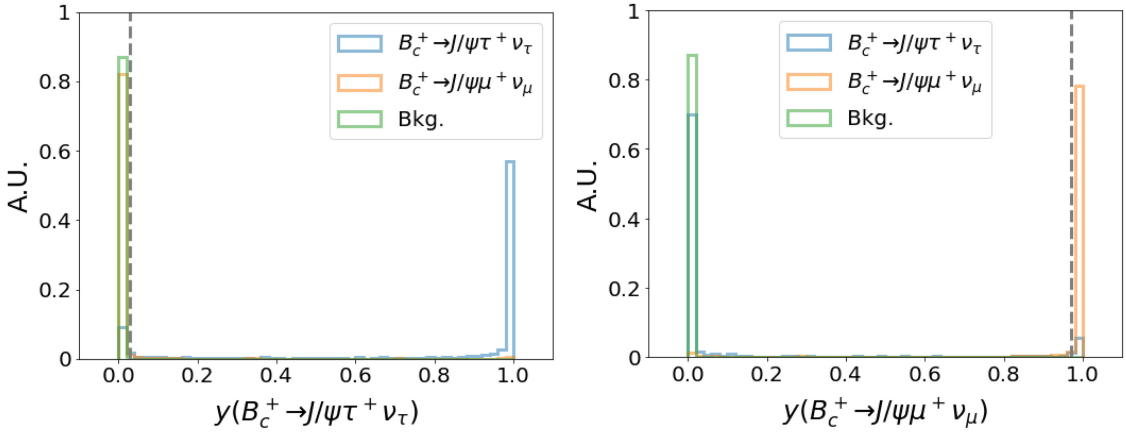

FIG. 5. Distributions of BDT response in favor of $B_c^+ \to J/\psi\tau^+\nu_\tau$ ($y^\tau_{J/\psi}$) and $B_c^+ \to J/\psi\mu^+\nu_\mu$ ($y^\mu_{J/\psi}$) in the $R_{J/\psi}$ measurement. The vertical dashed lines represent optimal thresholds for sensitivity analysis.

IV. MEASUREMENT OF $R_{D_s^{(*)}}$

A. Method

To measure $R_{D_s^{(*)}}$, we consider the exclusive B_s^0 decays, i.e., $B_s^0 \to D_s^- \mu^+ \nu_\mu$ and $B_s^0 \to D_s^- \tau^+ \nu_\tau$ with $D_s^- \to \phi(\to K^+K^-)\pi^-$, as the signals. All signal modes contain $K^+K^-\pi^-\mu^+$ in their final states. The schematic of the $B_s^0 \to D_s^{*-}\tau^+\nu_\tau$ process is shown in Fig. 6. Below are a set of cuts applied to preselect such events.

(i) The $K^+K^-\pi^-\mu^+$ selection. The events with two oppositely charged kaon tracks, one charged pion track sharing a secondary vertex, and exactly one muon track with a charge opposite to the identified pion track are selected. All tracks need to have $p_T > 0.1$ GeV.

(ii) The D_s^- selection. The two kaons should satisfy $|m_{K^+K^-} - m_\phi| < 12$ MeV, with the displacement of their vertex from the PV being greater than 0.5 mm. Moreover, we require the reconstructed $K^+K^-\pi^-$ system to have $|m_{K^+K^-\pi^-} - m_{D_s}| < 25$ MeV. The D_s trajectory is inferred from the system's momentum $p_{K^+K^-\pi^-}$ and its vertex. The minimum distance between the reconstructed D_s trajectory and any other tracks (except the muon one) needs to be > 0.02 mm.

(iii) The B_s^0 selection. We divide the space into signal and tag hemispheres with a plane perpendicular to the

TABLE V. Event counts in the signal regions of $B_c^+ \to J/\psi\tau^+\nu_\tau$ and $B_c^+ \to J/\psi\mu^+\nu_\mu$ for the $R_{J/\psi}$ measurement at Tera-Z.

	$y^\tau_{J/\psi} \geq 0.03 \cap y^\mu_{J/\psi} < 0.97$	$y^\tau_{J/\psi} < 0.03 \cap y^\mu_{J/\psi} \geq 0.97$
$B_c^+ \to J/\psi\tau^+\nu_\tau$	2.68×10^3	2.14×10^2
$B_c^+ \to J/\psi\mu^+\nu_\mu$	4.30×10^3	7.62×10^4
Inclusive bkg.	3.17×10^2	4.08×10^2
Cascade bkg.	6.21×10^2	8.87×10^1
Combinatoric bkg.	2.04×10^3	2.66×10^2
Mis-ID bkg.	$\epsilon_{\mu\pi} \times 2.09 \times 10^5$	$\epsilon_{\mu\pi} \times 3.30 \times 10^4$

TABLE VI. Expected BDT (relative) precisions of measuring $R_{J/\psi}$ at Tera-Z ($10 \times$ Tera-Z).

	$B_c^+ \to J/\psi\tau^+\nu_\tau$		$B_c^+ \to J/\psi\mu^+\nu_\mu$		$R_{J/\psi}$
q^2 range	Rel. precision	S/B	Rel. precision	S/B	Rel. precision
$q^2 < 7.15$ GeV^2	8.19×10^{-2} (2.59×10^{-2})	0.18	5.18×10^{-3} (1.64×10^{-3})	48.80	8.20×10^{-2} (2.59×10^{-2})
$q^2 \geq 7.15$ GeV^2	4.56×10^{-2} (1.44×10^{-2})	0.47	6.93×10^{-3} (2.19×10^{-3})	96.27	4.61×10^{-2} (1.46×10^{-2})
Full q^2	4.23×10^{-2} (1.34×10^{-2})	0.29	4.15×10^{-3} (1.31×10^{-3})	58.31	4.25×10^{-2} (1.35×10^{-2})

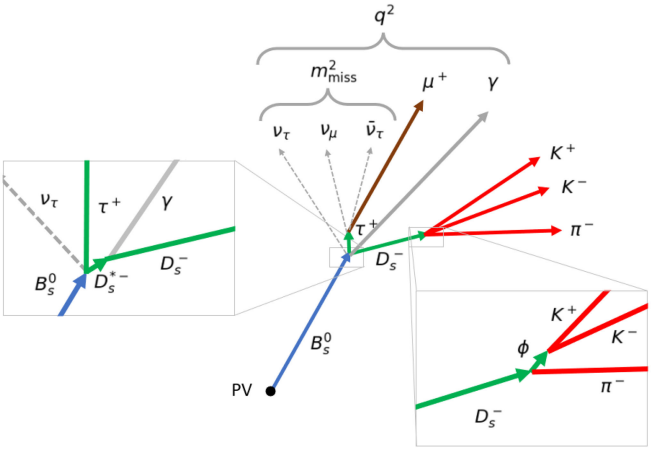

FIG. 6. Schematic of the $B_s^0 \to D_s^{*-}\tau^+\nu$ process. D_s^{*-} decays to D_s^- with extra photon. Compared to that of J/ψ in the $R_{J/\psi}$ measurement, the lifetime of D_s^- here is longer.

displacement of the reconstructed D_s^-. The D_s^- vertex appears in the signal hemisphere. The muon track must appear in the signal hemisphere, having $p_T > 1.2$ GeV and a minimal distance greater than 0.02 mm from all tracks except the reconstructed D_s trajectory. The $K^+K^-\pi^-\mu^+$ system needs to have an invariant mass smaller than m_{B_s}.

The Tera-Z yields for the preselected signals and the backgrounds are summarized in Table VII. The requirement of narrow D_s^- and B_s^0 resonances excludes most of the backgrounds except the inclusive ones, as expected.

The B_s^0 four-momentum can be reconstructed using the method introduced in Sec. III A. However, the D_s^- decay vertex does not approximate the B_s^0 one well, as shown in Fig. 6, due to its macroscopic D_s^- decay length. So we determine the B_s^0 decay vertex instead as the point on the D_s^- track closest to the muon track. Here the D_s^- tack is deduced from its decay vertex and momentum. Then, the B_s^0 four-momentum gets reconstructed by combining its displacement from the PV, total energy[3] (see Fig. 7 for its distribution)

$$E_{B_s^0} = E_{\rm sig} - \sum_{i\in \text{sig-hem}} E_i + E_{D_s^-} + E_\mu, \qquad (4.1)$$

and B_s^0 on-shell condition.

As done for the $R_{J/\psi}$ measurement, we introduce the kinematic variables q^2, $m^2_{\rm miss}$ and the minimal distance between the μ track and the secondary vertex $S_{\rm SV}$ to distinguish the signal events of the τ and μ modes. Their distributions are shown in Fig. 7. The events of the τ modes tend to have larger q^2, $m^2_{\rm miss}$, and $S_{\rm SV}$, compared to those of the μ modes. Notably, the reconstruction errors of q^2 [1.49(1.25) GeV^2 for R_{D_s} and 1.54(1.34) GeV^2 for $R_{D_s^*}$] and $m^2_{\rm miss}$ [1.46(1.12) GeV^2 for R_{D_s} and 1.46(1.23) GeV^2 for $R_{D_s^*}$] in this analysis are smaller than those of the $R_{J/\psi}$ measurement; the peaks for the $\log S_{\rm SV}$ distributions here are also shifted slightly to the left of those in the latter case. This is because the B_s^0 lifetime is about 3 times as long as B_c^+. A larger displacement from the PV can reduce the uncertainty in determining the b-hadron momentum direction.

The D_s^- and D_s^{*-} signal events are mutually the major backgrounds in their respective measurements (see Table VII). Nevertheless, they can be distinguished by the photon from the D_s^{*-} decay. For this purpose, we circulate all electromagnetic calorimeter (ECAL) photons in the signal hemisphere to identify the one that yields a $\Delta m \equiv m(K^+K^-\pi^-\gamma) - m(K^+K^-\pi^-)$ value closest to $m_{D_s^{*-}} - m_{D_s^-} = 143.8$ MeV [47]. The normalized Δm distributions for the signal and background events are shown in Fig. 8. A clear resonant structure forms for the D_s^{*-} signals, but not for the D_s^- signals. Notably, D_s^{*-} mesons can be produced in the cascade and inclusive backgrounds efficiently, so a resonant structure forms in their distribution also.

As shown in Figs. 7 and 8, the observables introduced above can separate the signals of different modes from the universal backgrounds to various extents. As before, we introduce a set of isolation observables with the cone size $\Omega = 0.3$ and 0.6 to further suppress these backgrounds. We show the distributions of $I_N(0.3\text{ rad})$ and $I_\gamma(0.3\text{ rad})$ in Fig. 9. In both cases, the signal events tend to concentrate around zero, while the universal backgrounds are distributed more broadly.

In this analysis, we train the BDT classifier in the five-class mode to address its four signal patterns ($D_s\mu$, $D_s\tau$, $D_s^*\mu$, $D_s^*\tau$). The full list of the discriminators is summarized below:

(1) Kinematics of the $K^+K^-\pi^-\mu^+$ system:
  (a) Invariant mass: $m_{KK\pi\mu}$.
  (b) Energy and momentum of the reconstructed D_s^- and muon: $E_{D_s^-}$, $|\vec{p}_{D_s^-}|$, E_μ, $|\vec{p}_\mu|$.
  (c) Mass difference: $\Delta m = m_{KK\pi\gamma} - m_{KK\pi}$.

(2) Observables of the reconstructed B_s^0:
  (a) Energy and momentum of the reconstructed B_s^0: $E_{B_s^0}$, $|\vec{p}_{B_s^0}|$.
  (b) Lorentz-invariant observables: $m^2_{\rm miss}$, q^2.

(3) Vertex information:
  (a) Minimal distance between the D_s^- decay vertex and the muon track.
  (b) Minimal distance between the deduced B_s^0 decay vertex and the muon track ($S_{\rm SV}$).
  (c) Minimal distance between the muon track and its closest track.
  (d) Minimal distance between the reconstructed D_s^- trajectory and its closest track.

[3]As a universal treatment, the energy of the D_s^* photon has not been included in the $E_{B_s^0}$ reconstruction. However, one can do so for a more dedicated analysis of R_{D^*} to improve the reconstruction quality of $E_{B_s^0}$.

TABLE VII. Tera-Z yields for the preselected signals and the backgrounds in the $R_{D_s^*}$ and R_{D_s} measurements. The preselection criteria are defined in the text.

Channel	Events at Tera-Z	$N(KK\pi\mu)$	$N(D_s^-)$	$N(B_s^0)$	Total eff. (%)
$B_s^0 \to D_s^- \tau^+ \nu_\tau$	1.03×10^6	7.92×10^5	6.45×10^5	4.81×10^5	46.77
$B_s^0 \to D_s^- \mu^+ \nu_\mu$	1.50×10^7	1.18×10^7	9.93×10^6	8.41×10^6	56.08
$B_s^0 \to D_s^{*-} \tau^+ \nu_\tau$	1.72×10^6	1.30×10^6	1.05×10^6	7.65×10^5	44.61
$B_s^0 \to D_s^{*-} \mu^+ \nu_\mu$	3.35×10^7	2.56×10^7	2.11×10^7	1.78×10^7	53.11
Inclusive bkg.	5.78×10^6	4.28×10^6	3.28×10^6	2.72×10^6	47.03
Cascade bkg.	8.44×10^7	6.20×10^7	2.33×10^7	8.71×10^6	10.33
Combinatoric bkg.	1.36×10^8	1.16×10^8	2.24×10^7	2.17×10^4	0.02
Mis-ID bkg.	$\epsilon_{\mu\pi} \times 1.05 \times 10^{10}$	$\epsilon_{\mu\pi} \times 4.33 \times 10^9$	$\epsilon_{\mu\pi} \times 8.41 \times 10^8$	$\epsilon_{\mu\pi} \times 8.50 \times 10^7$	0.81

(e) Distance between the D_s^- decay vertex and the PV.

(4) Isolation observables:
   (a) Neutral particles: $I_N(0.3\text{ rad})$, $I_N(0.6\text{ rad})$.
   (b) Neutral hadrons: $I_H(0.3\text{ rad})$, $I_H(0.6\text{ rad})$.
   (c) Photons: $I_\gamma(0.3\text{ rad})$, $I_\gamma(0.6\text{ rad})$.
   (d) Charged particles: $I_T(0.3\text{ rad})$, $I_T(0.6\text{ rad})$.
   (e) Tracks from the PV: $I_{T,\mathrm{PV}}(0.3\text{ rad})$, $I_{T,\mathrm{PV}}(0.6\text{ rad})$.
   (f) Tracks not from the PV: $I_{T,\mathrm{dis}}(0.3\text{ rad})$, $I_{T,\mathrm{dis}}(0.6\text{ rad})$.
(5) Impact parameter of the tracks in the signal hemisphere:
   (a) Maximum and sum of transverse impact parameters.
   (b) Maximum and sum of longitudinal impact parameters.
(6) Some other discriminators [59]:

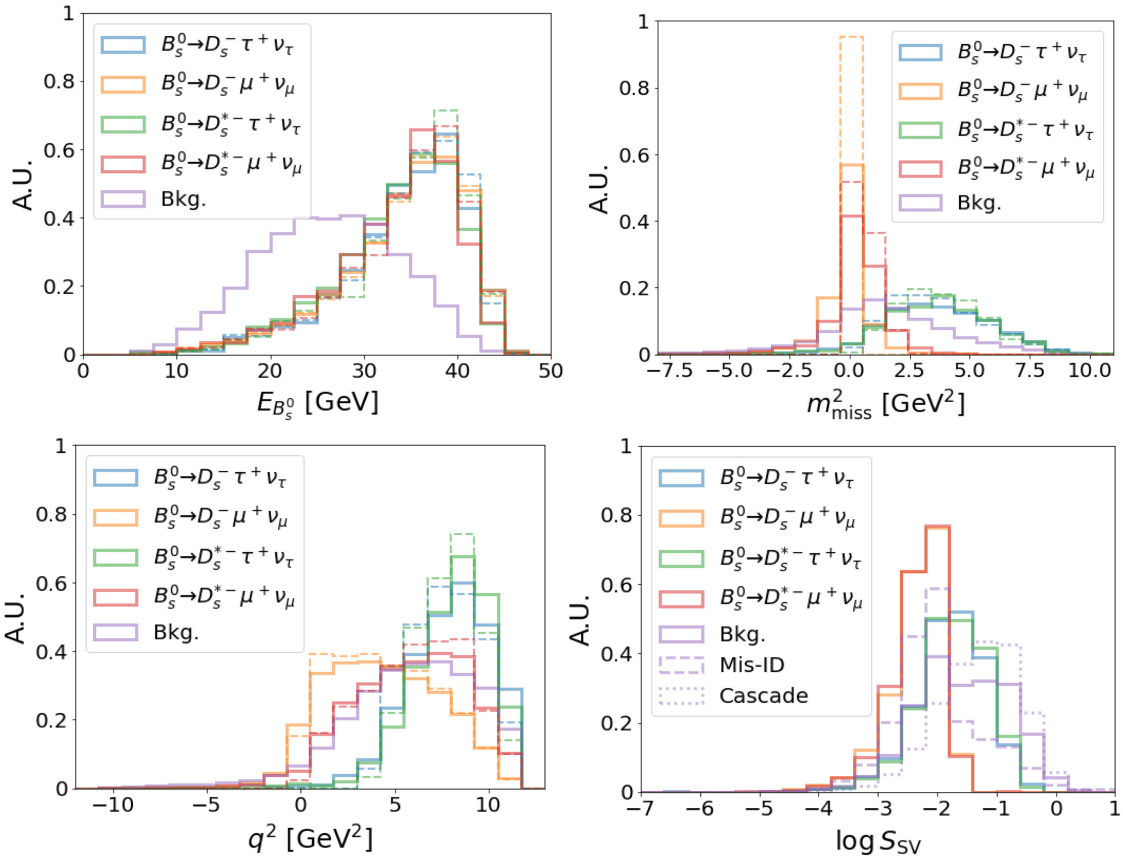

FIG. 7. Distributions of the reconstructed $E_{B_s^0}$, q^2, m^2_{miss}, and log S_{SV} in the $R_{D_s^{(*)}}$ measurement. The solid and dashed lines represent the simulated and truth-level values, respectively.

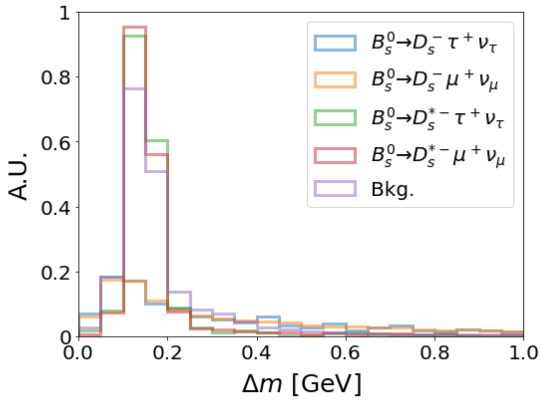

FIG. 8. Normalized distributions of Δm in the $R_{D_s^{(*)}}$ measurement.

(a) $D_s^- \mu^+$ momentum transverse to the B_s^0 moving direction: $p_\perp(D_s^- \mu^+)$.
(b) Corrected mass: $m_{\rm corr} = \sqrt{m^2(D_s^- \mu^+) + p_\perp^2(D_s^- \mu^+)} + p_\perp(D_s^- \mu^+)$.

B. Results

In Fig. 10, we show the distributions of BDT response in favor of $B_s^0 \to D_s^- \tau^+ \nu_\tau$, $B_s^0 \to D_s^- \mu^+ \nu_\mu$, $B_s^0 \to D_s^{*-} \tau^+ \nu_\tau$, and $B_s^0 \to D_s^{*-} \mu^+ \nu_\mu$. We summarize the event counts in the four signal regions in Table VIII and the expected precisions of R_{D_s} and $R_{D_s^*}$ measurements at Tera-Z ($10 \times$ Tera-Z) in Tables IX and X. As before, the precisions of measuring $R_{D_s^{(*)}}$ are limited by the relatively low counts of the τ-mode signal events. The two tables also show that, in the high q^2 region where a larger $R_{D_s^{(*)}}$ has been predicted, a better precision can be achieved compared to the low q^2 region. Meanwhile, the relatively high S/B ratios in all scenarios ensure the robustness of the sensitivity analysis of measuring $R_{D_s^{(*)}}$ against the potential systematic uncertainties. At last, we point out that the imperfect discrimination between the D_s and D_s^* modes induces negative correlations between the R_{D_s} and $R_{D_s^*}$ measurements (see Tables IX and X). We will discuss this feature in more detail in Sec. VI B.

V. MEASUREMENT OF R_{Λ_c}

A. Method

To measure R_{Λ_c}, we consider the exclusive Λ_b^0 decays, i.e., $\Lambda_b^0 \to \Lambda_c^- \tau^+ \nu_\tau$ and $\Lambda_b^0 \to \Lambda_c^- \mu^+ \nu_\mu$ with $\Lambda_c^- \to \bar{p} K^+ \pi^-$, as the signals. Both signal modes contain $\bar{p} K^+ \pi^- \mu^+$ in their final states. The schematic of the $\Lambda_b^0 \to \Lambda_c^- \tau^+ \nu_\tau$ process is shown in Fig. 11. Below are a set of cuts applied to preselect such events.

(i) The $\bar{p} K^+ \pi^- \mu^+$ selection. Candidates events that have $\bar{p}$, K^+, and π^- tracks ($p_T > 0.1$ GeV) sharing the same displaced decay vertex are selected. We also require exactly one muon track ($p_T > 0.1$ GeV) with the same charge as the identified charged Kaon.
(ii) The Λ_c^- selection. The $\bar{p} K^+ \pi^-$ vertex's distance from the PV must be greater than 0.5 mm, with its invariant mass $|m_{\bar{p} K^+ \pi^-} - m_{\Lambda_c}| < 14$ MeV. The Λ_c trajectory is reconstructed based on $p_{\bar{p} K^+ \pi^-}$ and its decay vertex. The closest distance between the reconstructed Λ_c system and any other track beside the identified muon must be > 0.02 mm.
(iii) The Λ_b^0 selection. Once the Λ_c^- candidate is identified, two hemispheres are divided by the plane perpendicular to the displacement of Λ_c^- decay vertex, with the signal hemisphere containing the Λ_c^- decay vertex. The muon candidate must be found in the signal hemisphere. Similar to the requirement in Sec. IV, its minimal distance from other tracks, except the tagged $\bar{p} K^+ \pi^-$ tracks, needs to be greater than 0.02 mm. Also, its p_T has to be larger than 1.2 GeV. Finally, the invariant mass of $\bar{p} K^+ \pi^- \mu^+$ has to be smaller than $m_{\Lambda_b^0}$.

The expected Tera-Z yields after the preliminary cuts are shown in Table XI.

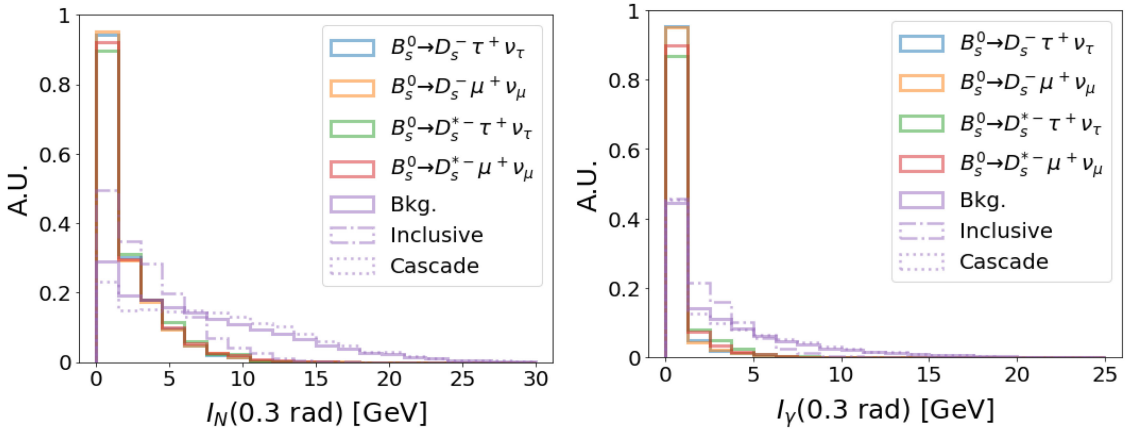

FIG. 9. Distributions of $I_N(0.3\ \text{rad})$ and $I_\gamma(0.3\ \text{rad})$ in the $R_{D_s^{(*)}}$ measurement.

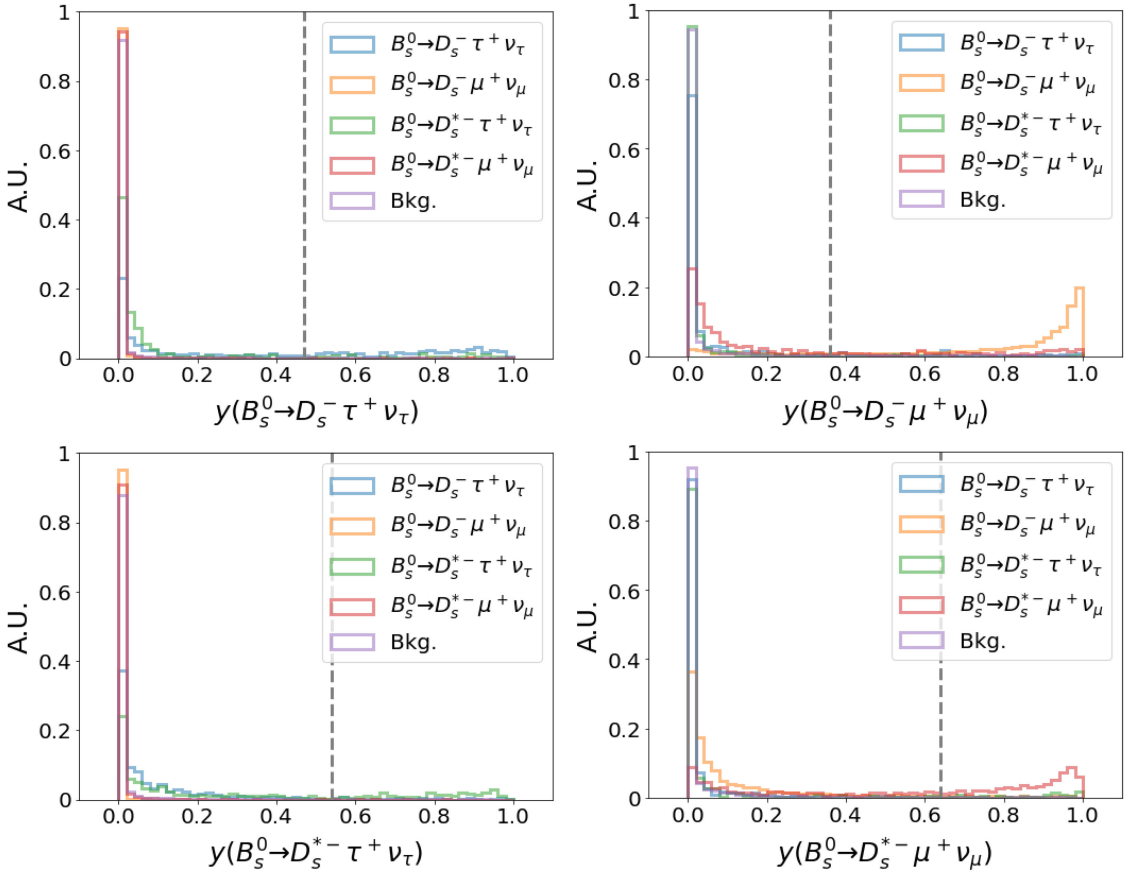

FIG. 10. Distributions of BDT response in favor of $B_s^0 \to D_s^- \tau^+ \nu_\tau$ ($y_{D_s}^\tau$), $B_s^0 \to D_s^- \mu^+ \nu_\mu$ ($y_{D_s}^\mu$), $B_s^0 \to D_s^{*-} \tau^+ \nu_\tau$ ($y_{D_s^*}^\tau$), and $B_s^0 \to D_s^{*-} \mu^+ \nu_\mu$ ($y_{D_s^*}^\mu$) in the $R_{D_s^{(*)}}$ measurement. The vertical dashed lines represent optimal thresholds for sensitivity analysis.

As has been done for other signal b hadrons, we can reconstruct the Λ_b^0 four-momentum using its decay vertex (or the $p_{\Lambda_b^0}$ direction) inferred from the Λ_c^- and μ lepton kinematics, total energy

$$E_{\Lambda_b^0} = E_{\rm sig} - \sum_{i \in \text{sig-hem}} E_i + E_{\Lambda_c^-} + E_\mu, \qquad (5.1)$$

and on-shell condition. Then we can introduce the Lorentz-invariant observables q^2 and $m_{\rm miss}^2$ and the minimal distance between the μ track and the secondary vertex $S_{\rm SV}$ to separate the signals of the τ and μ modes and the set of isolation observables of Λ_b^0 to suppress the universal backgrounds. We show the distributions of these observables in Figs. 12 and 13. The reconstruction errors of q^2 and

TABLE VIII. Event counts in the signal regions of $B_s^0 \to D_s^- \tau^+ \nu_\tau$, $B_s^0 \to D_s^- \mu^+ \nu_\mu$, $B_s^0 \to D_s^{*-} \tau^+ \nu_\tau$, and $B_s^0 \to D_s^{*-} \mu^+ \nu_\mu$ for the $R_{D_s^{(*)}}$ measurement at Tera-Z.

	$y_{D_s}^\tau \geq 0.47$ $\cap\, y_{D_s}^\mu < 0.36$ $\cap\, y_{D_s^*}^\tau < 0.54$ $\cap\, y_{D_s^*}^\mu < 0.64$	$y_{D_s}^\tau < 0.47$ $\cap\, y_{D_s}^\mu \geq 0.36$ $\cap\, y_{D_s^*}^\tau < 0.54$ $\cap\, y_{D_s^*}^\mu < 0.64$	$y_{D_s}^\tau < 0.47$ $\cap\, y_{D_s}^\mu < 0.36$ $\cap\, y_{D_s^*}^\tau \geq 0.54$ $\cap\, y_{D_s^*}^\mu < 0.64$	$y_{D_s}^\tau < 0.47$ $\cap\, y_{D_s}^\mu < 0.36$ $\cap\, y_{D_s^*}^\tau < 0.54$ $\cap\, y_{D_s^*}^\mu \geq 0.64$
$B_s^0 \to D_s^- \tau^+ \nu_\tau$	2.05×10^5	5.58×10^4	2.76×10^4	1.13×10^4
$B_s^0 \to D_s^- \mu^+ \nu_\mu$	2.43×10^4	7.11×10^6	$\lesssim 8.70 \times 10^2$	5.14×10^5
$B_s^0 \to D_s^{*-} \tau^+ \nu_\tau$	9.38×10^4	2.53×10^4	2.22×10^5	6.00×10^4
$B_s^0 \to D_s^{*-} \mu^+ \nu_\mu$	1.10×10^5	4.88×10^6	1.22×10^5	9.03×10^6
Inclusive bkg.	4.12×10^4	3.99×10^5	4.35×10^4	2.61×10^5
Cascade bkg.	6.63×10^4	1.35×10^5	3.66×10^4	4.80×10^4
Combinatoric bkg.	$\lesssim 3.43 \times 10^3$	$\lesssim 3.43 \times 10^3$	$\lesssim 3.43 \times 10^3$	$\lesssim 3.43 \times 10^3$
Mis-ID bkg.	$\epsilon_{\mu\pi} \times 4.21 \times 10^5$	$\epsilon_{\mu\pi} \times 6.22 \times 10^6$	$\epsilon_{\mu\pi} \times 3.82 \times 10^5$	$\epsilon_{\mu\pi} \times 1.41 \times 10^6$

TABLE IX. Expected BDT (relative) precisions of measuring R_{D_s} at Tera-Z ($10 \times$ Tera-Z).

	$B_s^0 \to D_s^- \tau^+ \nu_\tau$		$B_s^0 \to D_s^- \mu^+ \nu_\mu$		R_{D_s}	Correlation
q^2 range	Rel. precision	S/B	Rel. precision	S/B	Rel. precision	ρ w/$R_{D_s^*}$
$q^2 < 7.15$ GeV^2	8.17×10^{-3} (2.58×10^{-3})	0.49	5.83×10^{-4} (1.84×10^{-4})	1.57	9.37×10^{-3} (2.96×10^{-3})	−0.56
$q^2 \geq 7.15$ GeV^2	4.43×10^{-3} (1.40×10^{-3})	0.62	1.39×10^{-3} (4.38×10^{-4})	0.74	4.72×10^{-3} (1.49×10^{-3})	−0.48
Full q^2	3.81×10^{-3} (1.21×10^{-3})	0.60	5.42×10^{-4} (1.72×10^{-4})	1.28	4.09×10^{-3} (1.30×10^{-3})	−0.49

TABLE X. Expected BDT (relative) precisions of measuring $R_{D_s^*}$ at Tera-Z ($10 \times$ Tera-Z).

	$B_s^0 \to D_s^{*-} \tau^+ \nu_\tau$		$B_s^0 \to D_s^{*-} \mu^+ \nu_\mu$		$R_{D_s^*}$	Correlation
q^2 range	Rel. precision	S/B	Rel. precision	S/B	Rel. precision	ρ w/R_{D_s}
$q^2 < 7.15$ GeV^2	9.93×10^{-3} (3.14×10^{-3})	0.53	5.24×10^{-4} (1.66×10^{-4})	7.90	9.93×10^{-3} (3.14×10^{-3})	−0.56
$q^2 \geq 7.15$ GeV^2	3.50×10^{-3} (1.11×10^{-3})	1.04	5.94×10^{-4} (1.88×10^{-4})	15.25	3.49×10^{-3} (1.10×10^{-3})	−0.48
Full q^2	3.27×10^{-3} (1.03×10^{-3})	0.95	3.94×10^{-4} (1.24×10^{-4})	9.93	3.26×10^{-3} (1.03×10^{-3})	−0.49

m^2_{miss} are given by 1.37(1.23) and 1.33(1.18) GeV^2, respectively.

In this analysis, we train the BDT classifier in the three-class mode to address its two signal patterns. The full list of the discriminators is summarized below:

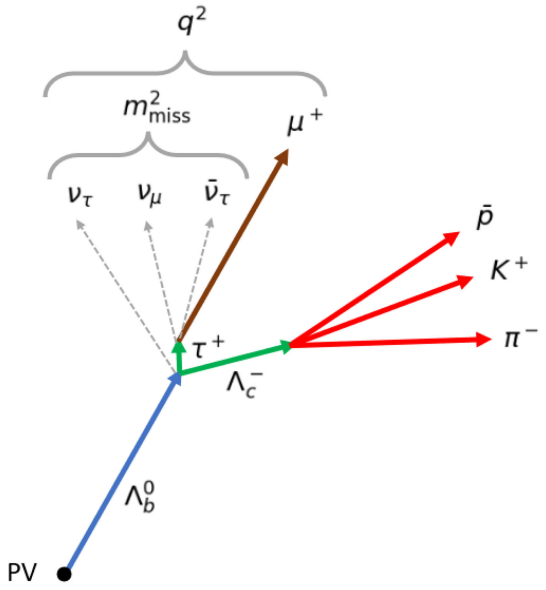

FIG. 11. Schematic of the $\Lambda_b^0 \to \Lambda_c^- \tau^+ \nu$ process. Similar to $R_{D_s^{(*)}}$ in that the lifetime of Λ_c^- here is longer compared to that of J/ψ in the $R_{J/\psi}$ measurement.

(1) Kinematics of the $\bar{p}K^+\pi^-\mu^+$ system:
  (a) Invariant mass: $m_{pK\pi\mu}$.
  (b) Energy and momentum of the reconstructed Λ_c and muon: $E_{\Lambda_c^-}$, $|\vec{p}_{\Lambda_c^-}|$, E_μ, $|\vec{p}_\mu|$.
(2) Observables of the reconstructed Λ_b^0:
  (a) Energy and momentum of the reconstructed Λ_b^0: $E_{\Lambda_b^0}$, $|\vec{p}_{\Lambda_b^0}|$.
  (b) Lorentz-invariant observables: m^2_{miss}, q^2.
(3) Vertex information:
  (a) Minimal distance between the Λ_c^- decay vertex and the muon track.
  (b) Minimal distance between the deduced Λ_b^0 decay vertex and the muon track (S_{SV}).
  (c) Minimal distance between the muon track and its closest track.
  (d) Minimal distance between the reconstructed Λ_c^- trajectory and its closest track.
  (e) Distance between the Λ_c^- decay vertex and the PV.
(4) Isolation observables:
  (a) Neutral particles: $I_N(0.3\text{ rad})$, $I_N(0.6\text{ rad})$.
  (b) Neutral hadrons: $I_H(0.3\text{ rad})$, $I_H(0.6\text{ rad})$.
  (c) Photons: $I_\gamma(0.3\text{ rad})$, $I_\gamma(0.6\text{ rad})$.
  (d) Charged particles: $I_T(0.3\text{ rad})$, $I_T(0.6\text{ rad})$.
  (e) Tracks from the PV: $I_{T,\text{PV}}(0.3\text{ rad})$, $I_{T,\text{PV}}(0.6\text{ rad})$.
  (f) Tracks not from the PV: $I_{T,\text{dis}}(0.3\text{ rad})$, $I_{T,\text{dis}}(0.6\text{ rad})$.

TABLE XI. Tera-Z yields for the preselected signals and the backgrounds in the R_{Λ_c} measurement. The preselection criteria are defined in the text.

Channel	Events at Tera-Z	$N(pK\pi\mu)$	$N(\Lambda_c^+)$	$N(\Lambda_b^0)$	Total eff. (%)
$\Lambda_b^0 \to \Lambda_c^- \tau^+ \nu_\tau$	4.46×10^6	3.52×10^6	2.96×10^6	2.22×10^6	49.89
$\Lambda_b^0 \to \Lambda_c^- \mu^+ \nu_\mu$	7.58×10^7	6.23×10^7	5.26×10^7	4.48×10^7	59.11
Inclusive bkg.	2.75×10^6	2.17×10^6	6.75×10^5	5.79×10^5	21.05
Cascade bkg.	1.03×10^6	8.05×10^5	4.05×10^5	2.18×10^5	21.19
Combinatoric bkg.	1.57×10^7	1.33×10^7	4.93×10^5	7.91×10^2	0.01
Mis-ID bkg.	$\epsilon_{\mu\pi} \times 1.36 \times 10^9$	$\epsilon_{\mu\pi} \times 5.43 \times 10^8$	$\epsilon_{\mu\pi} \times 4.05 \times 10^7$	$\epsilon_{\mu\pi} \times 1.52 \times 10^7$	1.12

(5) Impact parameter of the tracks in the signal hemisphere:
   (a) Maximum and sum of transverse impact parameters.
   (b) Maximum and sum of longitudinal impact parameters.
(6) Some other discriminators [59]:
   (a) $\Lambda_c^- \mu^+$ momentum transverse to the Λ_b^0 moving direction: $p_\perp(\Lambda_c^- \mu^+)$.
   (b) Corrected mass: $m_{\rm corr} = \sqrt{m^2(\Lambda_c^- \mu^+) + p_\perp^2(\Lambda_c^- \mu^+)} + p_\perp(\Lambda_c^- \mu^+)$.

B. Results

In Fig. 14, we show the distributions of BDT response in favor of $\Lambda_b^0 \to \Lambda_c^- \tau^+ \nu_\tau$ and $\Lambda_b^0 \to \Lambda_c^- \mu^+ \nu_\mu$. We summarize the event counts in the two signal regions in Table XII and the expected precisions of measuring R_{Λ_c} at Tera-Z ($10 \times$ Tera-Z) in Table XIII. The S/B ratios are high to avoid large background systematics similar to previous R_{H_c} measurements.

VI. IMPACTS OF DETECTOR PERFORMANCE AND EVENT SHAPE

A. Detector tracking resolution

In the analysis scheme developed above for measuring R_{H_c}, the H_b reconstruction significantly relies on the determination of the H_c decay vertex and the measurement

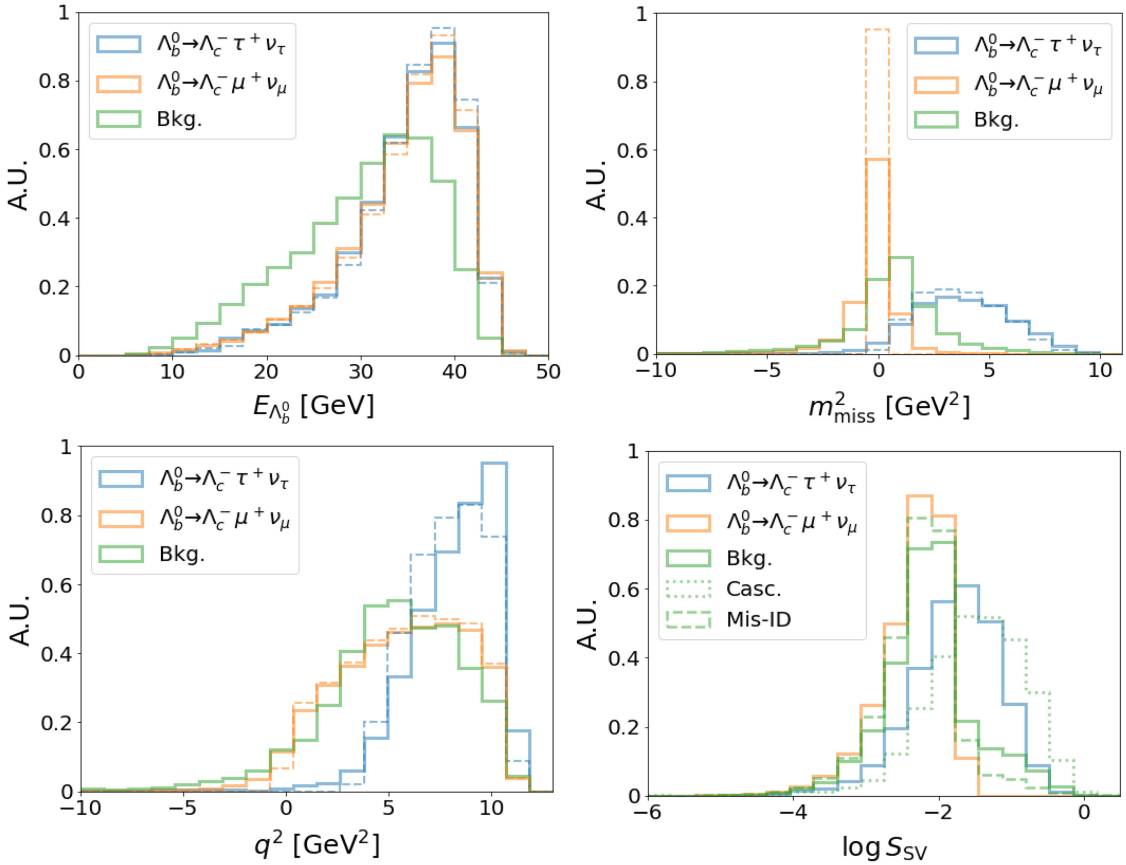

FIG. 12. Distributions of the reconstructed $E_{\Lambda_b^0}$, q^2, $m^2_{\rm miss}$, and $\log S_{\rm SV}$ in the R_{Λ_c} measurement. The solid and dashed lines represent the simulated and truth-level messages, respectively.

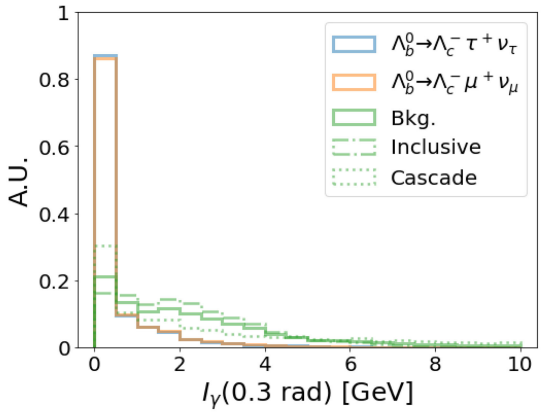

FIG. 13. Distribution of $I_\gamma(0.3\text{ rad})$ in the R_{Λ_c} measurement.

of the muon track originating from the H_b or τ decay. The precision of measuring R_{H_c} thus could be sensitive to the tracker resolution of impact parameters. To explore the potential improvement with a better tracker resolution and test the robustness of the presented results against a worse situation, one then needs to draw a picture of the variation of the precision of measuring R_{H_c} with the tracker resolution. In our previous analyses, we have simulated the tracker effects via the vertex noise and modeled it as a random vector with a reference magnitude of 10 μm. The noise is then injected to the H_c decay vertex and the muon track vertex independently, following a normal distribution $\mathcal{N}(0, 100/3)$ μm in each direction such that the overall noise respects the normal distribution $\mathcal{N}(0, 100)$ μm. To generate a global picture mentioned above, below we will perform a series of studies, with the noise level varying from a perfect tracker case to more conservative resolution scenarios.

Let us consider q^2, m^2_{miss}, and S_{SV}. As the tracker resolution correlates with the quality of H_b reconstruction, these event-level observables measure the impacts on event reconstruction and R_{H_c} sensitivities. We present the distributions of δq^2, δm^2_{miss} for the four R_{H_c} measurements in Figs. 15–18, with four benchmark vertex noise levels: 0, 5, 10, and 20 μm. The dependence of their root mean square on the vertex noise level is also shown in Fig. 19, where more benchmark noise levels are simulated. We have the following observations based on these figures:

(i) For the reconstruction of q^2 and m^2_{miss}, $B_c^+ \to J/\psi\tau^+\nu_\tau$ and $B_c^+ \to J/\psi\mu^+\nu_\mu$ tend to be more sensitive to the variation of vertex noise level, compared to the other signal channels. As J/ψ decays promptly, in these cases we have used the J/ψ decay vertex to approximate the b-hadron decay vertex. So, the b-hadron vertex reconstruction has a higher quality in an ideal detector, but is less robust against the vertex noise.

(ii) For the reconstruction of S_{SV}, the muon signal modes tend to be more sensitive to the variation of vertex noise level compared to the τ signal modes. At the truth level, we have $S_{\text{SV}} \equiv 0$ μm for all four muon signal channels. Especially, for $B_c^+ \to J/\psi\mu^+\nu_\mu$, its S_{SV} can be "perfectly" measured in an "ideal" detector, due to the high-quality reconstruction of the B_c^+ decay vertex. However, this also implies that the reconstruction of S_{SV} in this case is less robust than the other three muon channels. As for the τ signal modes, we have $S_{\text{SV}} \neq 0$ μm at the truth level as the muon track in these cases is generated from τ decay and hence displaced from the b-hadron vertex. Because of the extra complexity caused by τ decay, the error of reconstructing S_{SV} in these cases is generally big. However, as the B_c^+ vertex can be well reconstructed for the τ mode also, for $B_c^+ \to J/\psi\tau^+\nu_\tau$

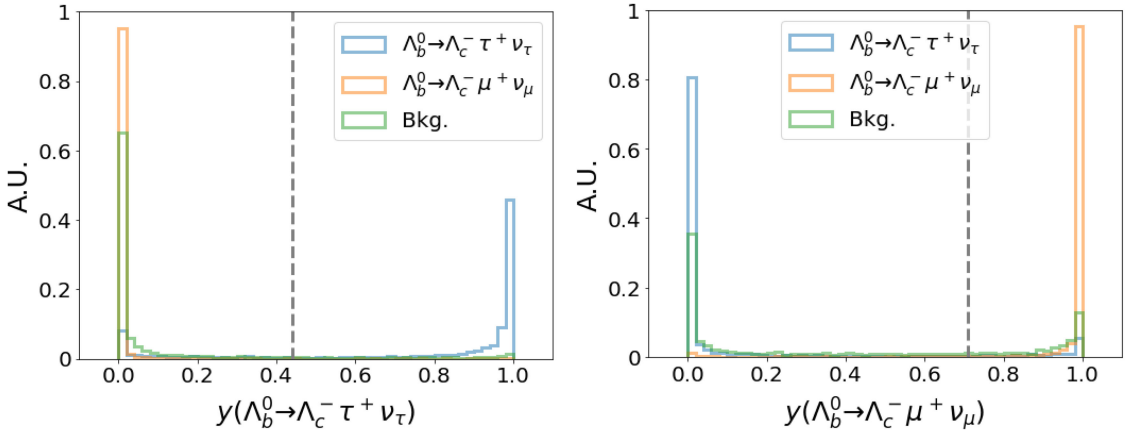

FIG. 14. Distributions of BDT response in favor of $\Lambda_b^0 \to \Lambda_c^-\tau^+\nu_\tau$ ($y^\tau_{\Lambda_c}$) and $\Lambda_b^0 \to \Lambda_c^-\mu^+\nu_\mu$ ($y^\mu_{\Lambda_c}$) in the $R_{J/\psi}$ measurement. The vertical dashed lines represent optimal thresholds for sensitivity analysis.

TABLE XII. Event counts in the signal regions of $\Lambda_b^0 \to \Lambda_c^- \tau^+ \nu_\tau$ and $\Lambda_b^0 \to \Lambda_c^- \mu^+ \nu_\mu$ for the R_{Λ_c} measurement at Tera-Z.

	$y^\tau_{\Lambda_c} \geq 0.44 \cap y^\mu_{\Lambda_c} < 0.71$	$y^\tau_{\Lambda_c} < 0.44 \cap y^\mu_{\Lambda_c} \geq 0.71$
$\Lambda_b^0 \to \Lambda_c^- \tau^+ \nu_\tau$	1.79×10^6	2.51×10^5
$\Lambda_b^0 \to \Lambda_c^- \mu^+ \nu_\mu$	5.34×10^5	4.26×10^7
Inclusive bkg.	4.84×10^4	2.57×10^5
Cascade bkg.	4.53×10^4	2.63×10^4
Combinatoric bkg.	$\lesssim 4.76 \times 10^2$	$\lesssim 4.76 \times 10^2$
Mis-ID bkg.	$\epsilon_{\mu\pi} \times 4.87 \times 10^5$	$\epsilon_{\mu\pi} \times 2.72 \times 10^6$

TABLE XIII. Expected BDT (relative) precisions of measuring R_{Λ_c} at Tera-Z ($10 \times$ Tera-Z).

	$\Lambda_b^0 \to \Lambda_c^- \tau^+ \nu_\tau$		$\Lambda_b^0 \to \Lambda_c^- \mu^+ \nu_\mu$		R_{Λ_c}
q^2 range	Rel. precision	S/B	Rel. precision	S/B	Rel. precision
$q^2 < 7.15$ GeV^2	2.01×10^{-3} (6.34×10^{-4})	1.63	2.22×10^{-4} (7.01×10^{-5})	71.81	2.02×10^{-3} (6.38×10^{-4})
$q^2 \geq 7.15$ GeV^2	1.10×10^{-3} (3.49×10^{-4})	3.74	2.86×10^{-4} (9.04×10^{-5})	77.94	1.14×10^{-3} (3.60×10^{-4})
Full q^2	9.61×10^{-4} (3.04×10^{-4})	2.83	1.75×10^{-4} (5.54×10^{-5})	75.98	9.77×10^{-4} (3.09×10^{-4})

the measurement of $S_{\rm SV}$ is as sensitive to the vertex noise as it is for the muon channels.

At last, we demonstrate the averaged relative precisions of measuring R_{H_c} in the bottom-right panel of Fig. 19, with varied vertex noise. Consisting with the observations above, the precision of measuring $R_{J/\psi}$ gets improved more with the reduced vertex noise, while the measurement of R_{Λ_c} tends to be more robust against the variation of vertex noise.

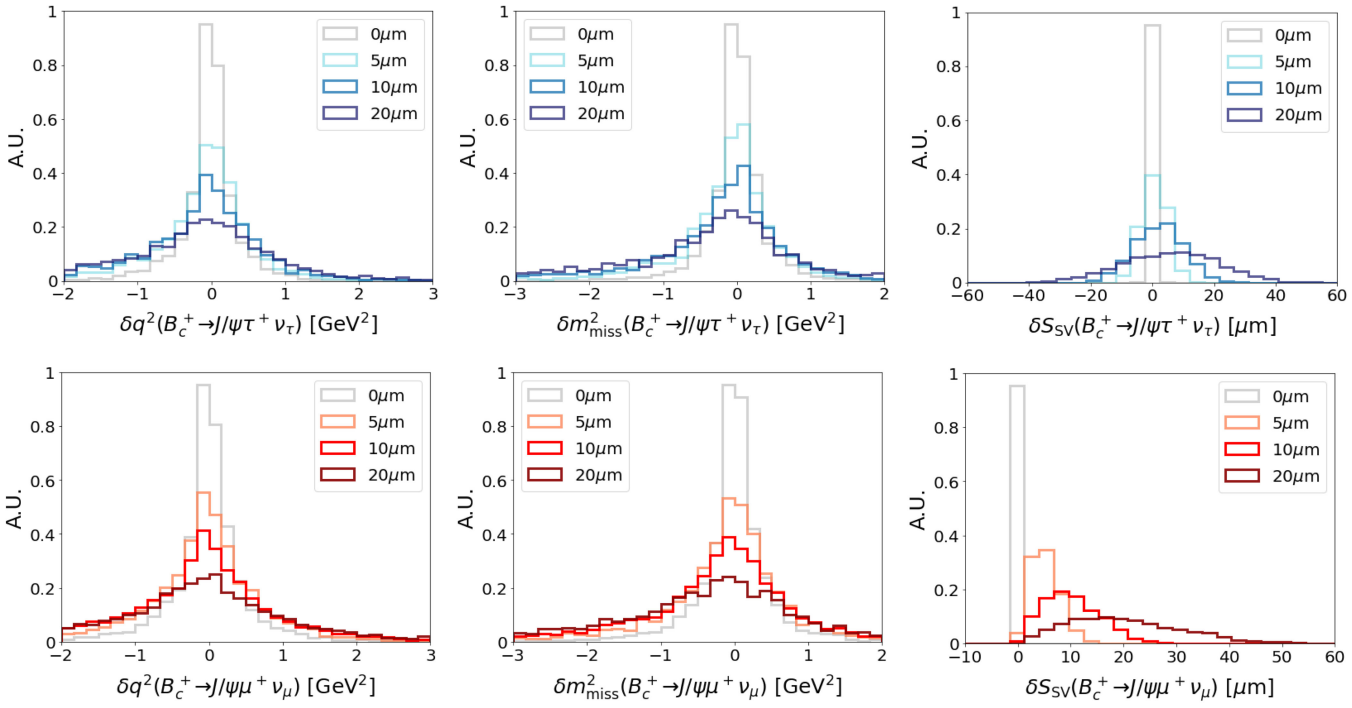

FIG. 15. Distributions of δq^2, $\delta m^2_{\rm miss}$, and $\delta S_{\rm SV}$ for $B_c^+ \to J/\psi \tau^+ \nu_\tau$ and $B_c^+ \to J/\psi \mu^+ \nu_\mu$, respectively.

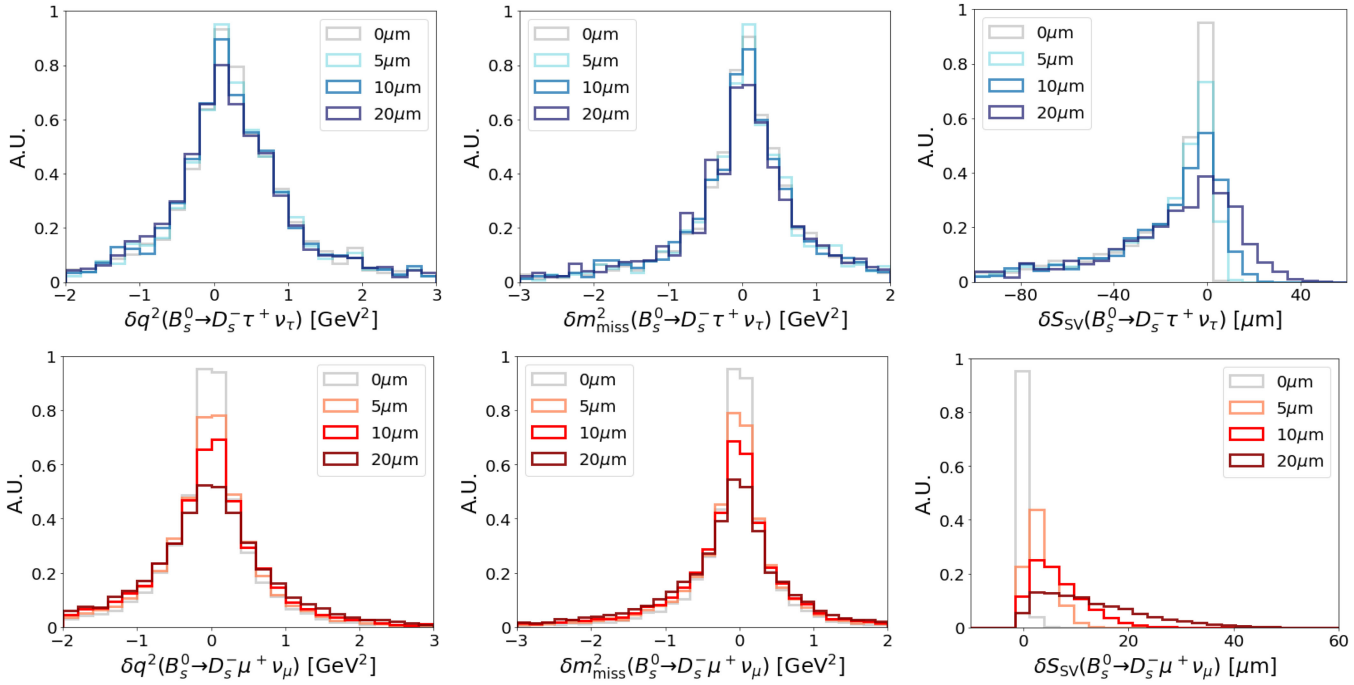

FIG. 16. Distributions of δq^2, $\delta m^2_{\rm miss}$, and $\delta S_{\rm SV}$ for $B_s^0 \to D_s^- \tau^+ \nu_\tau$ and $B_s^0 \to D_s^- \mu^+ \nu_\mu$, respectively.

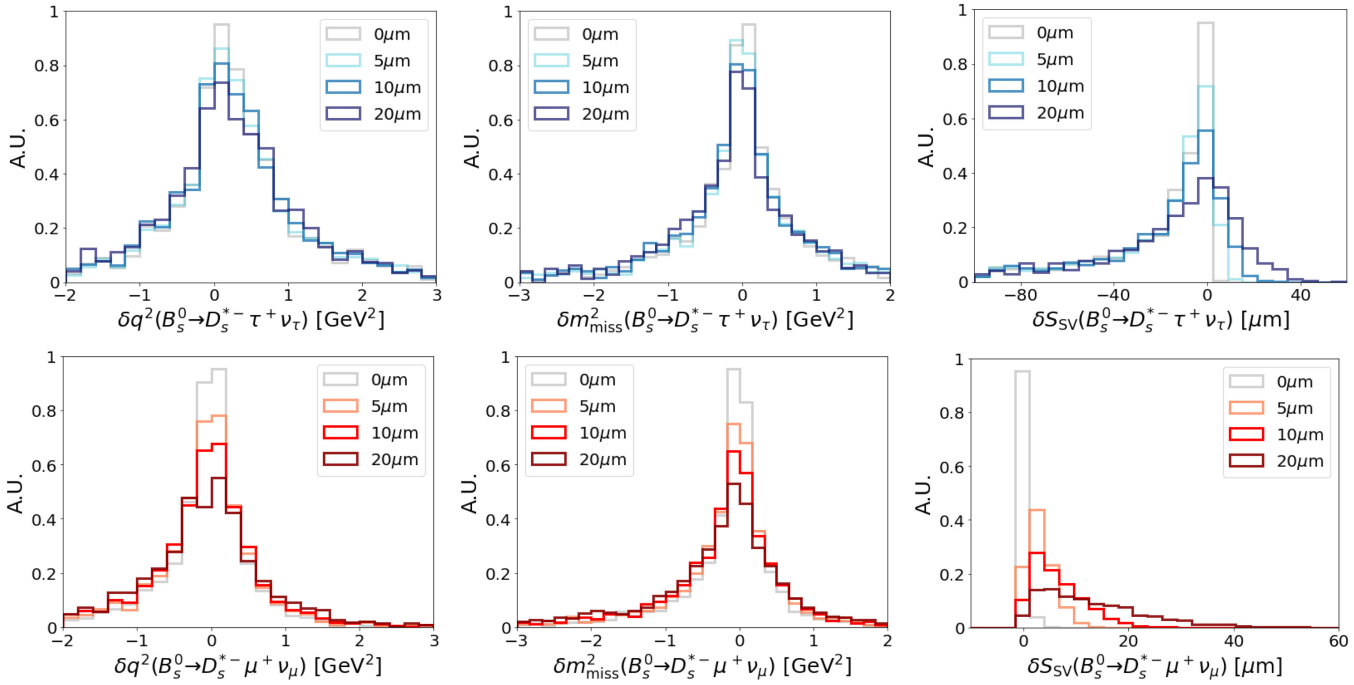

FIG. 17. Distributions of δq^2, $\delta m^2_{\rm miss}$, and $\delta S_{\rm SV}$ for $B_s^0 \to D_s^{*-} \tau^+ \nu_\tau$ and $B_s^0 \to D_s^{*-} \mu^+ \nu_\mu$, respectively.

B. ECAL energy threshold

As shown in the R_{D_s} and $R_{D_s^*}$ analyses in Sec. IV, the $B_s^0 \to D_s^- \tau^+ \nu_\tau (B_s^0 \to D_s^- \mu^+ \nu_\mu)$ and $B_s^0 \to D_s^{*-} \tau^+ \nu_\tau (B_s^0 \to D_s^{*-} \mu^+ \nu_\mu)$ events contribute mutually as one of the major backgrounds in their respective measurements. A natural discriminator between them could be the photon from the $D_s^{*-} \to D_s^- \gamma$ decay. So we have introduced a measure $\Delta m \equiv m(K^+K^-\pi^-\gamma) - m(K^+K^-\pi^-)$ in our analyses and reconstructed this photon as the one yielding a Δm value closest to $m_{D_s^{*-}} - m_{D_s^-} = 143.8$ MeV, among all ECAL photons in the signal hemisphere. The Δm defined for the reconstructed D_s^{*-} photon is then applied in the relevant BDT analyses.

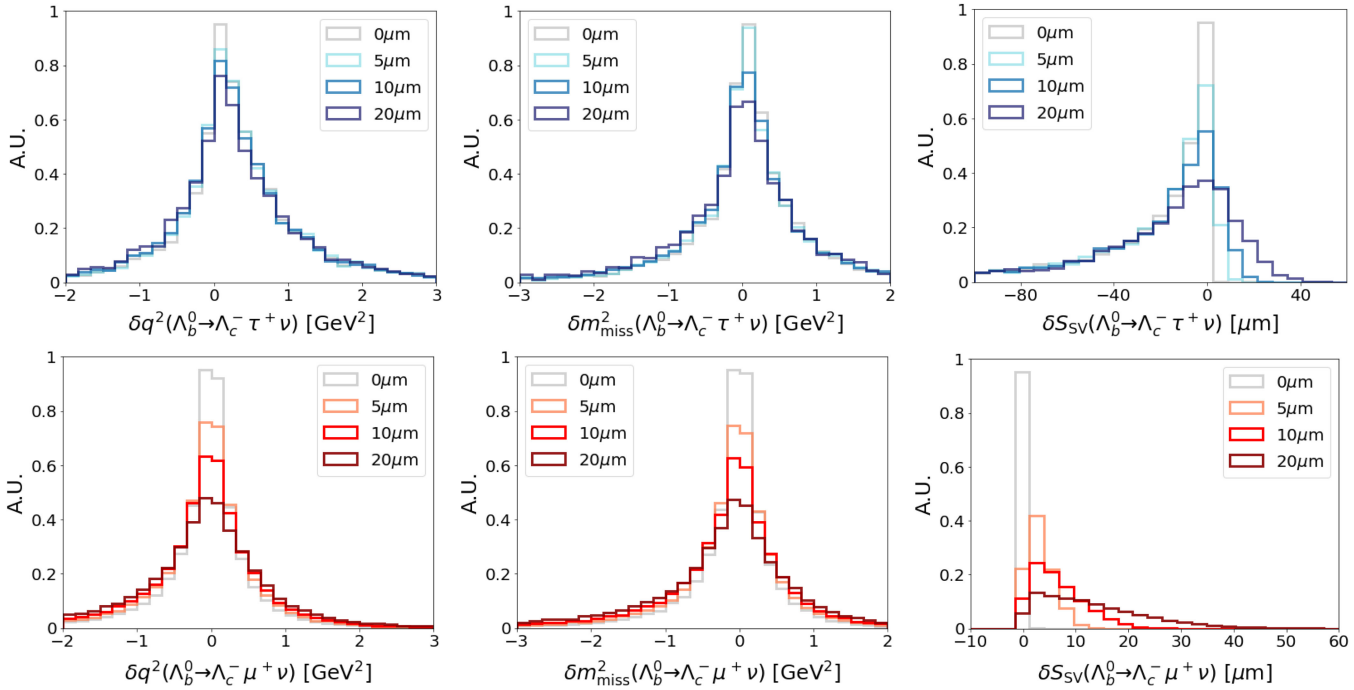

FIG. 18. Distributions of δq^2, $\delta m^2_{\rm miss}$, and $\delta S_{\rm SV}$ for $\Lambda_b^0 \to \Lambda_c^- \tau^+ \nu_\tau$ and $\Lambda_b^0 \to \Lambda_c^- \mu^+ \nu_\mu$, respectively.

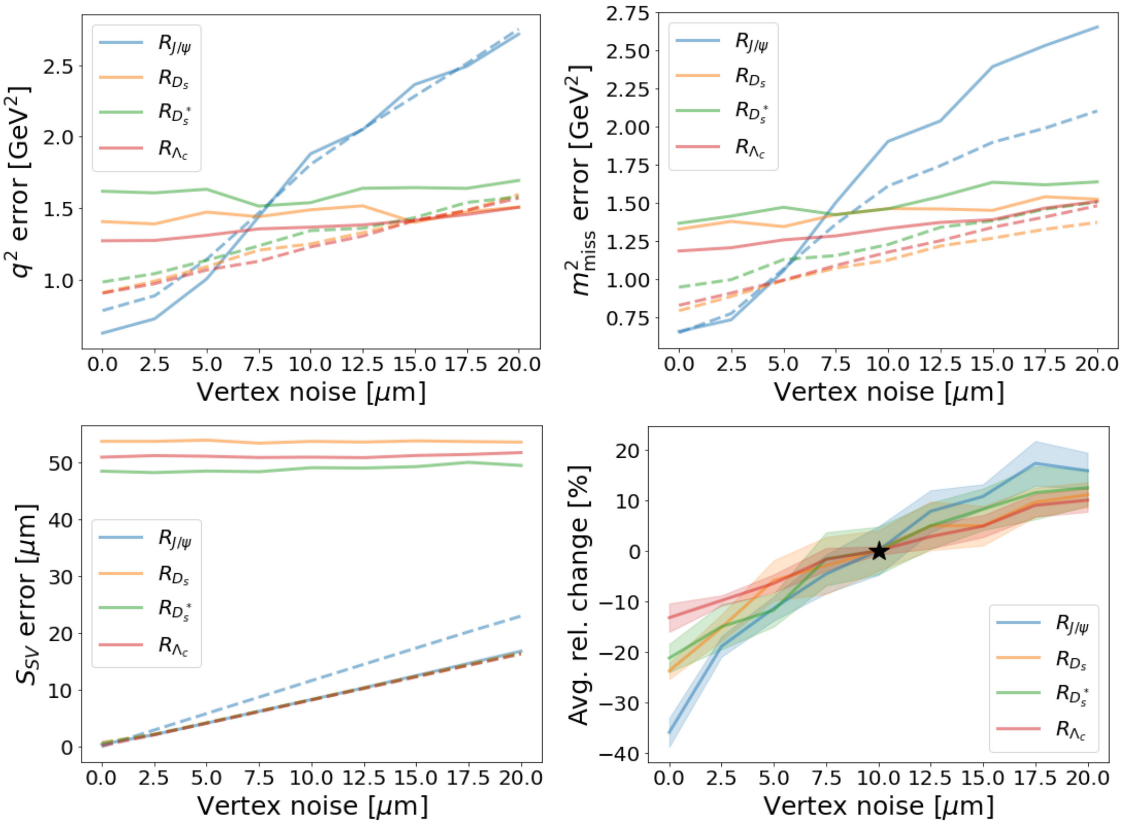

FIG. 19. Reconstruction error of q^2 (upper left), $m^2_{\rm miss}$ (upper right), $S_{\rm SV}$ (bottom left) and averaged relative changes to the reference precision of measuring R_{H_c} (bottom right), with varied vertex noise. In the first three panels, the reconstruction error is defined to be the root mean square of δX over the signal sample, with $X = q^2$, $m^2_{\rm miss}$, and $S_{\rm SV}$. The solid and dashed lines correspond to the τ and μ modes, respectively. Bottom right: we have trained ten BDT classifiers, with ten random separations of the training (50%) and testing (50%) datasets, respectively, in the full simulation data samples. The averaged relative changes to the measurement precisions and their variances are denoted as solid lines and shaded bands, respectively. The reference precisions are simulated with a vertex noise of 10 μm, denoted as a black star.

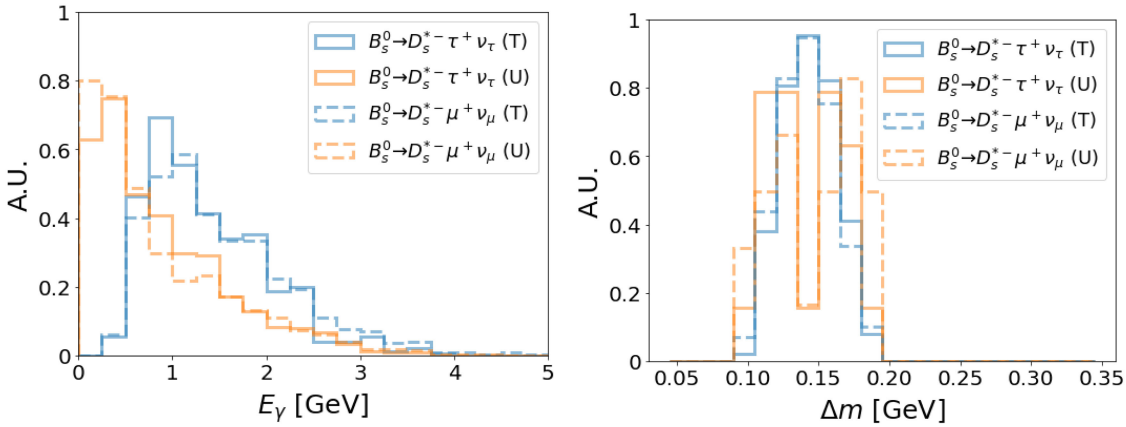

FIG. 20. Distributions of E_γ (left) for the truth-level D_s^{*-} photons and Δm (right) for the reconstructed photons satisfying the consistency condition in footnote 4, in $B_s^0 \to D_s^{*-}\tau^+\nu_\tau$ and $B_s^0 \to D_s^{*-}\mu^+\nu_\mu$. Photons tagged (T) by the detector simulation are shown as blue curves, while untagged (U) photons are shown in orange.

However, the D_s^{*-} photon tends to be soft, with energy typically $\lesssim \mathcal{O}(1)$ GeV. The performance of ECAL in detecting soft photons thus becomes highly crucial. The ECAL responds weakly to soft photons. Below some energy threshold ($E_{\rm th}$), the photons may not cause a response in the ECAL at all. We demonstrate this effect in the left panel of Fig. 20. We classify the $B_s^0 \to D_s^{*-}\tau^+\nu_\tau$ and $B_s^0 \to D_s^{*-}\mu^+\nu_\mu$ events into the "tagged" and "untagged" ones, with $E_{\rm th} = 0.5$ GeV, a default value in the Delphes model. In the former case, a D_s^{*-} photon that is consistent with the truth in kinematics[4] and additionally yields a Δm value closest to 143.8 MeV can be reconstructed, while in the latter case such a reconstruction fails. Following this criterion, we find that only ∼40% D_s^{*-} photons are reconstructed successfully. Most of them have a truth-level energy above $E_{\rm th}$ (despite a failure of reconstruction for some "energetic" D_s^{*-} photons due to, e.g., a collimation with other particles in the ECAL). In contrast, almost all $B_s^0 \to D_s^{*-}\tau^+\nu_\tau$ and $B_s^0 \to D_s^{*-}\mu^+\nu_\mu$ events containing a D_s^{*-} photon with its energy below $E_{\rm th}$ leave an empty entry in the ECAL and hence are untagged. In addition to $E_{\rm th}$, the reconstruction efficiency of D_s^{*-} photons can be impacted by the momentum resolution of the ECAL. This feature is shown in the right panel of Fig. 20, with a distribution of the tagged (T) and untagged (U) D_s^{*-} photons with respect to Δm. Clearly, the reconstruction quality of Δm tends to be lower for the untagged D_s^{*-} photons. However, as the fraction of such untagged D_s^{*-} photons is small in the pool, at a level of several percent only, we will focus on the effect of $E_{\rm th}$ below.

In Fig. 21, we demonstrate the impacts of $E_{\rm th}$ on the tagging efficiency of D_s^{*-} photons and the precisions of measuring R_{D_s} and $R_{D_s^*}$ (and the correlation between these precisions). Clearly, reducing the $E_{\rm th}$ value will improve both analyses. It yields a positive change up to tens of percent to the tagging efficiency, relative to its reference value simulated at $E_{\rm th} = 0.5$ GeV. Consistently, the expected BDT precisions of measuring R_{D_s} and $R_{D_s^*}$ also get improved. To end this subsection, we point out that reducing $E_{\rm th}$ from its reference value will weaken the correlation between the R_{D_s} and $R_{D_s^*}$ measurements significantly. This may further strengthen the constraints on the relevant SMEFT, a study to be performed in Sec. VII.

C. Event shape

In the analyses above, we have focused on the features of b-hadron decay products. However, the kinematics of particles at event level, namely, event shape [60], may carry extra information to distinguish the signals from their backgrounds. The B_c^+ production in the $R_{J/\psi}$ measurement is such an example. In this process, two bottom and two charm quarks are produced [61]. One charm quark and one bottom quark are then confined into a B_c^+ meson, while the second charm quark forms an extra c hadron, as illustrated in Fig. 1. We show the energy distribution of the second c hadron and the distribution of its included angle with the B_c^+ meson in Fig. 22. For many of these events, their second c hadron has energy more than 5 or even 10 GeVs, and its included angle with the B_c^+ meson can be quite big also. Such events have three hard or relatively hard heavy-flavored hadrons, i.e., B_c^+ and extra b and c hadrons, yielding a shape different from those of the back-to-back $2b$ events and the multiparton $4b$ events, where the heavy quarks stem from Z decay or QCD radiation rather than weak decays. The $2b$ events have been known to significantly contribute to the combinatoric and muon mis-ID backgrounds. The observables of event shape thus could be applied to further improve the sensitivity of measuring $R_{J/\psi}$

[4]The consistency here requires the η and ϕ separation between the reconstructed and truth-level D_s^{*-} photons to be less than 0.01 and the energy difference to be smaller than 30%.

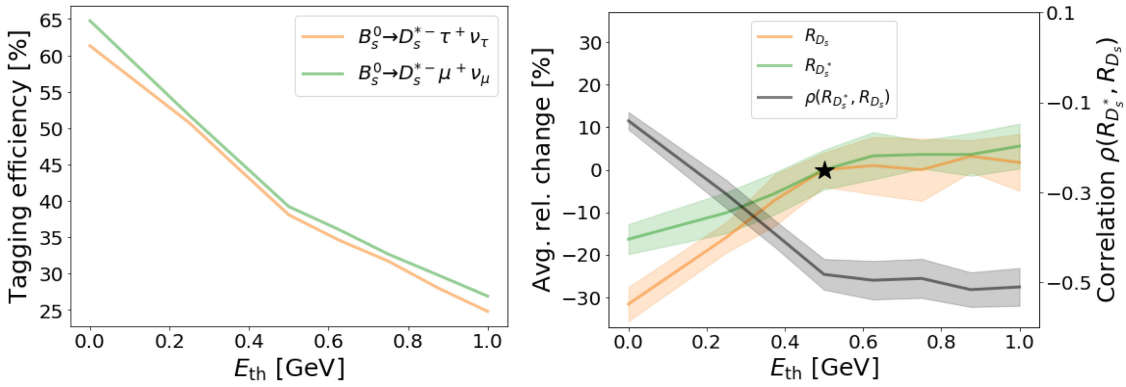

FIG. 21. Tagging efficiency of D_s^{*-} photons (left) and averaged relative change to the reference precisions of measuring R_{D_s} and $R_{D_s^*}$ (and the correlation between these precisions) (right), with a varied value of $E_{\rm th}$. Right: the averaged values (solid lines) and their variances (shaded bands) are calculated based on ten BDT analyses with their training and testing datasets defined in the caption of Fig. 19. The reference precisions are simulated with $E_{\rm th} = 0.5$ GeV, denoted as a black star.

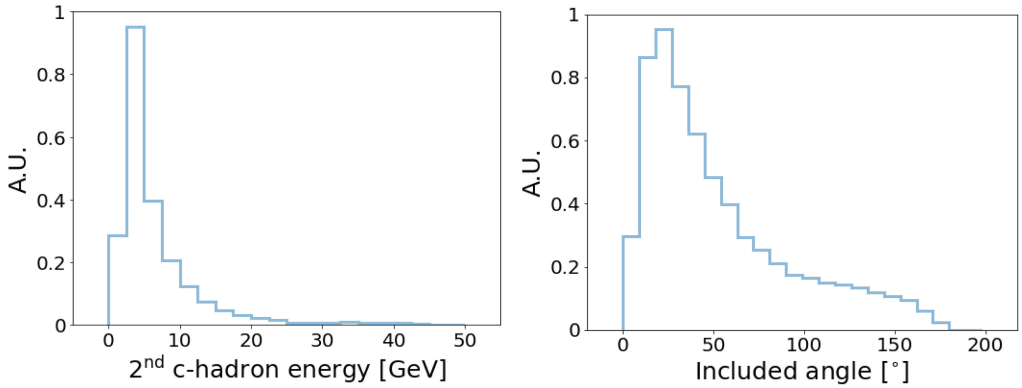

FIG. 22. Energy distribution of the second c hadron in a B_c^+ event (left) and distribution of its included angle with the B_c^+ meson (right).

by suppressing its backgrounds with the information beyond the B_c^+ decay.[5]

The event-level observables are highly suitable for the analyses at e^-e^+ colliders, given no generic contaminations in hadron collisions applied such as pileups and underlying events. Many event-level observables have been originally proposed for the e^-e^+ and e^-h events [62] rather than the hh ones [63]. Especially, the definiteness of the center of mass frame for the e^-e^+ collision events have motivated two of the authors in this paper to build up a dictionary between the Mollweide projection of individual e^-e^+ collision events and the all-sky cosmic microwave background (CMB) map (see Table 2 in [64]), where the event-level kinematics corresponds to the anisotropy of CMB, and accordingly a CMB-like observable scheme for collider events. In this observable scheme, the Fox-Wolfram (FW) moments [65] of individual events play a leading role, just like the CMB power spectrum. For simplicity, we only consider the FW moments of visible energy of particles which are defined as

$$\begin{aligned} H_{EE;l} &= \sum_{m=-l}^{l} H_{EE;l,m} \\ &= \frac{4\pi}{2l+1} \sum_{i,j} \frac{E_i E_j}{s} \sum_{m=-l}^{l} (Y_l^m(\Omega_i)^* Y_l^m(\Omega_j)) \\ &= \sum_{i,j} \frac{E_i E_j}{s} P_l(\cos\Omega_{ij}). \end{aligned} \tag{6.1}$$

Here $Y_l^m(\Omega_i)$ is spherical harmonics of degree l and order m, $P_l(\cos\Omega_{ij})$ is Legendre polynomials, and

$$\cos\Omega_{ij} = \cos\theta_i \cos\theta_j + \sin\theta_i \sin\theta_j \cos(\phi_i - \phi_j) \tag{6.2}$$

[5]Alternatively, one can require a successful reconstruction of extra D meson via the decays such as $D^0 \to K^- 2\pi^+\pi^-$, $D^0 \to K^+\pi^-$, and $D^+ \to K^- 2\pi^+$, to improve the quality of reconstructing the $R_{J/\psi}$ signal events. The clean environment of a Z factory will benefit this goal. However, the observables of event shape provide a more systematic and efficient way to look into the information beyond the B_c^+ decay. So we will focus on their performance in this paper.

is the cosine of the included angle between two visible particle i and j. In this summation, i and j run over all visible particles in each event.

We show the cumulative Mollweide projections for the $B_c^+ \to J/\psi\tau^+\nu_\tau$ and $B_c^+ \to J/\psi\mu^+\nu_\mu$ events and the $2b$ and $4b$ (and also $2b2c$) background events in Fig. 23. As the combinatoric background receives the contributions from multiple Z decay topologies, we require here all $2b$ (50.4%), $4b$ (17.4%), and $2b2c$ (32.3%) events to be from this type of background. As a comparison, the inclusive background has similar event shape as that of the signals, as both of them stem from the $Z \to B_c^+ + X$ production, while the mis-ID background is mainly from the $B \to J/\psi + \pi^+ + X$ decays and hence has a $2b$-like event shape. From this figure, one can see that the two bright spots in the projections are smeared more for the $4b$ and $2b2c$ events than the signal events and $2b$ events. This is consistent with our expectation. Based on such projections, we demonstrate the averaged FW moments $\langle H_{EE;l}\rangle$ (as a counterpart of the CMB power spectrum at the detector sphere [64]) with $l = 1, \ldots, \ldots, 10$ and the event distribution with respect to $H_{EE;2}$, for these signal and background events in Fig. 24. Note, the range of l matches well with the angular resolution needed to look into the structure of signal events which is indicated by the right panel of Fig. 22. Below are the main observations (for detailed discussions on the underlying physics of the $\langle H_{EE;l}\rangle$ spectrum, see [64]).

(i) Because of $P_l(-x) = (-1)^l P_l(x)$, the moments with odd l are zero for the parity-even events such as the back-to-back $2b$ ones, which yield a zigzag structure for the spectra.

(ii) The tail for the $4b$ spectrum is damped more, compared to the other ones. This is because the

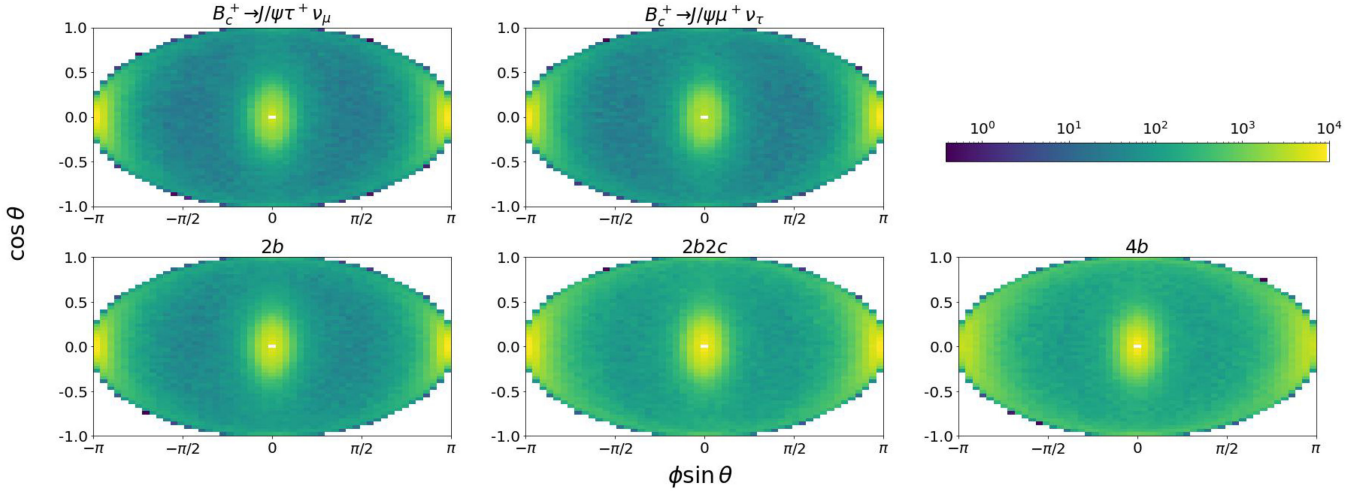

FIG. 23. Cumulative Mollweide projections (for details on such a projection, see Sec. 2.1 in [64]) for the $B_c^+ \to J/\psi\tau^+\nu_\tau$ and $B_c^+ \to J/\psi\mu^+\nu_\mu$ signal events (upper) and the $2b$, $4b$, and $2b2c$ combinatoric background events (bottom). In each panel, a total of 10000 events have been projected. The brightness of each cell is scaled with the total energy (GeV) of the particle hits received.

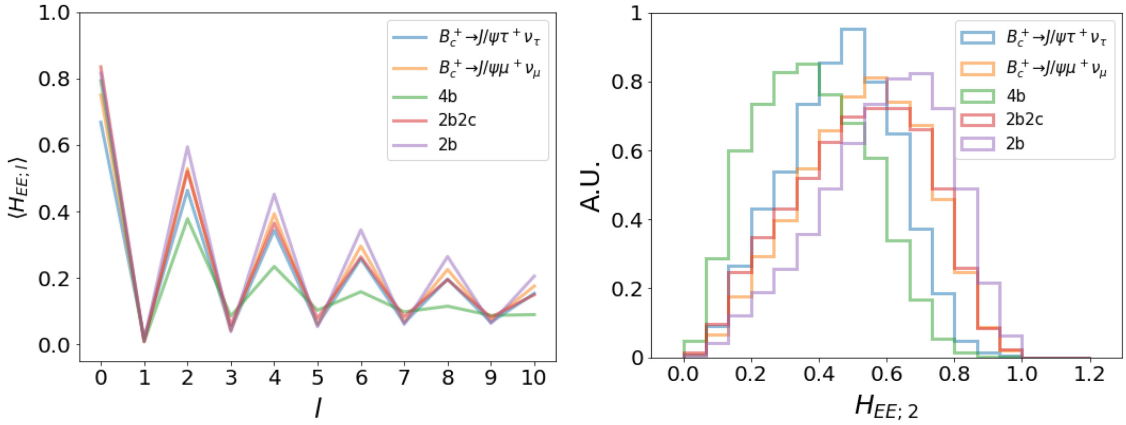

FIG. 24. Averaged FW moments $\langle H_{EE;l}\rangle$ with $l = 1, \ldots, \ldots, 10$ (left) and event distribution with respect to $H_{EE;2}$ (right), for the $B_c^+ \to J/\psi\tau^+\nu_\tau$ and $B_c^+ \to J/\psi\mu^+\nu_\mu$ signal events (upper) and the $2b$, $4b$, and $2b2c$ combinatoric background events.

parton shower yields more particles in the final state of this class of events. The democracy of allocating visible energy among these particles tends to reduce their self-correlation contribution (i.e., $H^{\rm self}_{EE;l} = \sum_i \frac{E_i^2}{s}$) to the FW moments (which is universal to all l) and hence damp the spectrum tail.

(iii) Note that $H_{EE;0} = \frac{(\sum_i E_i)^2}{s}$ denotes the squared share of the visible energy among the total in each event. The sorting of $\langle H_{EE;0}\rangle$ tells us that more missing energy tends to be produced for the $B_c^+ \to J/\psi\tau^+\nu_\tau$ events. The event distribution with respect to $H_{EE;2}$ in the right panel reminds us that, unlike the CMB power spectrum, the $\langle H_{EE;l}\rangle$ spectrum is free from the cosmic variance problem, because the collider data are ample.

(iv) The FW moments of $B_c^+ \to J/\psi\tau^+\nu_\tau$ and $B_c^+ \to J/\psi\mu^+\nu_\mu$ are close to those of the $2b2c$ events. This can be understood since these signal events are essentially the $2b2c$ events, except that they are produced with three heavy hadrons, while the combinatoric background events typically contain four ones.

Finally, let us consider the potential impacts of FW moments on the $R_{J/\psi}$ measurement. We perform an extra event selection with a BDT classifier developed with the $H_{EE;1-10}$ only before the BDT classifier based on the original set of observables is applied. The relevant analysis results are summarized in Table XIV. From this table, one can see that the inclusion of FW moments for event selection yields a suppression to the backgrounds universally faster than the reduction of signal events. Therein, the mis-ID backgrounds are suppressed most efficiently, by a factor of nearly 4. As a result, the S/B ratio for the τ and muon signal modes are enhanced by more than 10% and 30%, respectively, while the relative precision for measuring $R_{J/\psi}$ gets slightly improved. These outcomes suggest that the FW moments have worked as an independent discriminator beyond the kinematics of b-hadron decay, making this measurement more robust. Searching for other multi-heavy-flavor processes such as exotic states [66,67] may also benefit from such event-level observables. Notably, despite the gains from the FW moments, PYTHIA may not be accurate is simulating the event-level message, especially for the multi-heavy-flavor productions [61,68]. To be conservative, we have not included the FW moments or other event-shape observables in the analyses yielding the conclusions of this paper. We hope that an improved simulation tool for such an analysis will be available [69] in the near future.

VII. SMEFT INTERPRETATION

In this section, we will interpret in the SMEFT the projected sensitivities of measuring R_{H_c}, together with the observables involving the $b \to s\tau^+\tau^-$ [42] and $b \to s\nu\bar{\nu}$ [29] transitions, at the future Z factories. These measurements are performed at $\mu_b \sim m_b = 4.8$ GeV, an energy scale well below the SMEFT cutoff. So we need to include the effects of the renormalization group (RG) running in this analysis. Concretely, we will take RG running for the Wilson coefficients of SMEFT from the hypothesized new physics (NP) cutoff to the EW scale, match them with those of the low-energy EFT (LEFT) at this scale, and then run down the LEFT Wilson coefficients to μ_b such that they can interplay with the relevant measurements directly. Because of the generic symmetry requirement, the SMEFT Wilson coefficients are not fully independent. Their correlation is inherited by the LEFT Wilson coefficients, leaving an imprint in these measurements. Finally, the posterior distributions for the SMEFT Wilson coefficients will be analyzed by taking a Markov-chain Monte Carlo (MCMC) global fit.

TABLE XIV. Sensitivities of measuring $R_{J/\psi}$. All numbers in this table are generated by averaging the results of ten BDT analyses with their training and testing datasets defined in the caption of Fig. 19. In the "Original + FW moments" case, two BDT classifiers have been trained in each analysis: one is based on the FW moments only and another one uses the original set of observables as the inputs. Then the events are selected by the first BDT classifier before they are subject to the selection of the second BDT classifier.

	Original			Original + FW moments		
	Preselection	$y^\tau_{J/\psi} \geq 0.03$ $\cap$ $y^\mu_{J/\psi} < 0.97$	$y^\tau_{J/\psi} < 0.03$ $\cap$ $y^\mu_{J/\psi} \geq 0.97$	FW selection ($y_{B_c^+} > 0.05$)	$y^\tau_{J/\psi} \geq 0.03$ $\cap$ $y^\mu_{J/\psi} < 0.97$	$y^\tau_{J/\psi} < 0.03$ $\cap$ $y^\mu_{J/\psi} \geq 0.97$
$B_c^+ \to J/\psi\tau^+\nu_\tau$	3.08×10^3	2.77×10^3	2.06×10^2	2.88×10^3	2.60×10^3	1.81×10^2
$B_c^+ \to J/\psi\mu^+\nu_\mu$	8.40×10^4	4.33×10^3	7.64×10^4	6.56×10^4	3.83×10^3	5.95×10^4
Inclusive bkg.	3.90×10^3	4.44×10^2	3.67×10^2	2.31×10^3	3.76×10^2	2.54×10^2
Cascade bkg.	1.84×10^3	1.15×10^2	1.77×10^1	1.03×10^3	8.87×10^1	8.87×10^0
Combinatoric bkg.	7.78×10^4	1.98×10^3	1.60×10^2	3.93×10^4	1.61×10^3	1.51×10^2
Mis-ID bkg. ($\times\epsilon_{\mu\pi}$)	1.10×10^8	2.38×10^5	7.59×10^4	2.79×10^7	1.68×10^5	2.64×10^4
S/B	...	0.31	55.62	...	0.35	72.41
$R_{J/\psi}$ Rel. Precision		4.12×10^{-2}			4.06×10^{-2}	

TABLE XV. SM predictions for the relevant observables and relative precisions for their measurements at Belle II at 50 ab^{-1}, LHCb Upgrade II, Tera-Z, and 10 × Tera-Z.

Physical quantity	SM value	Tera-Z	10 × Tera-Z	Belle II	LHCb
$R_{J/\psi}$	0.289	4.25×10^{-2}	1.35×10^{-2}	⋯	⋯
R_{D_s}	0.393	4.09×10^{-3}	1.30×10^{-3}	⋯	⋯
$R_{D_s^*}$	0.303	3.26×10^{-3}	1.03×10^{-3}	⋯	⋯
R_{Λ_c}	0.334	9.77×10^{-4}	3.09×10^{-4}	⋯	⋯
$\mathrm{BR}(B_c \to \tau\nu)$	2.36×10^{-2} [41]	0.01 [41]	3.16×10^{-3}	⋯	⋯
$\mathrm{BR}(B^+ \to K^+\tau^+\tau^-)$	1.01×10^{-7}	7.92 [42]	2.48 [42]	198 [23]	⋯
$\mathrm{BR}(B^0 \to K^{*0}\tau^+\tau^-)$	0.825×10^{-7}	10.3 [42]	3.27 [42]	⋯	⋯
$\mathrm{BR}(B_s \to \phi\tau^+\tau^-)$	0.777×10^{-7}	24.5 [42]	7.59 [42]	⋯	⋯
$\mathrm{BR}(B_s \to \tau^+\tau^-)$	7.12×10^{-7}	28.1 [42]	8.85 [42]	⋯	702 [24]
$\mathrm{BR}(B^+ \to K^+\bar{\nu}\nu)$	4.6×10^{-6} [23]	⋯	⋯	0.11 [23]	⋯
$\mathrm{BR}(B^0 \to K^{*0}\bar{\nu}\nu)$	9.6×10^{-6} [23]	⋯	⋯	0.096 [23]	⋯
$\mathrm{BR}(B_s \to \phi\bar{\nu}\nu)$	9.93×10^{-6} [29]	1.78×10^{-2} [29]	5.63×10^{-3}	⋯	⋯

Here we have several comments. First, for the convenience of discussions, we assume that the LFU violation is possible for the third generation only, whereas the physics of other generations have been constrained to be highly consistent with the SM by the ongoing measurements or the measurements at the future Z factories. Second, we assume that the measured values for the relevant observables are centered at their SM predictions [70–76]. The expected measurement precisions are then summarized in Table XV. We also present the expected precisions of measuring the $b \to s\tau^+\tau^-$ [42], $b \to c\tau\nu$, and $b \to s\nu\bar{\nu}$ [29] transitions in Fig. 25, as a specific demonstration of the Z-factory performance in exploring the FCNC and FCCC physics with the third-generation leptons. Third, we ignore the systematics of measuring R_{H_c} and the errors of calculating R_{H_c}. The former is expected to be canceled to some extent since R_{H_c} denotes a ratio of two parallel measurements [this is also the reason that we apply the measurements of R_{H_c} instead of $\mathrm{BR}(H_b \to H_c\tau\nu_\tau)$ to constrain the SMEFT here]. However, the latter, which mainly arises from the uncertainty of the hadron decay form factors, is typically $\sim\mathcal{O}(10\%)$. This could be bigger than the statistical errors of the R_{H_c} measurements at the Z pole and hence downgrade their capability to probe the SMEFT. We hope that the theoretical and experimental developments later will bring these uncertainties down to a level comparable to or even below the statistical errors of these measurements by the time of operating the future Z factories.

A. Low-energy EFT

1. $b \to c\tau\nu$

In the 6D LEFT, the $b \to c\tau\nu$ transitions are described by

$$\mathcal{L}^{\mathrm{LE}}_{b\to c\tau\nu} = -\frac{4G_F V_{cb}}{\sqrt{2}}[(C^\tau_{V_L}|_{\mathrm{SM}} + \delta C^\tau_{V_L})O^\tau_{V_L} + C^\tau_{V_R}O^\tau_{V_R} + C^\tau_{S_L}O^\tau_{S_L} + C^\tau_{S_R}O^\tau_{S_R} + C^\tau_T O^\tau_T] + \mathrm{H.c.}, \quad (7.1)$$

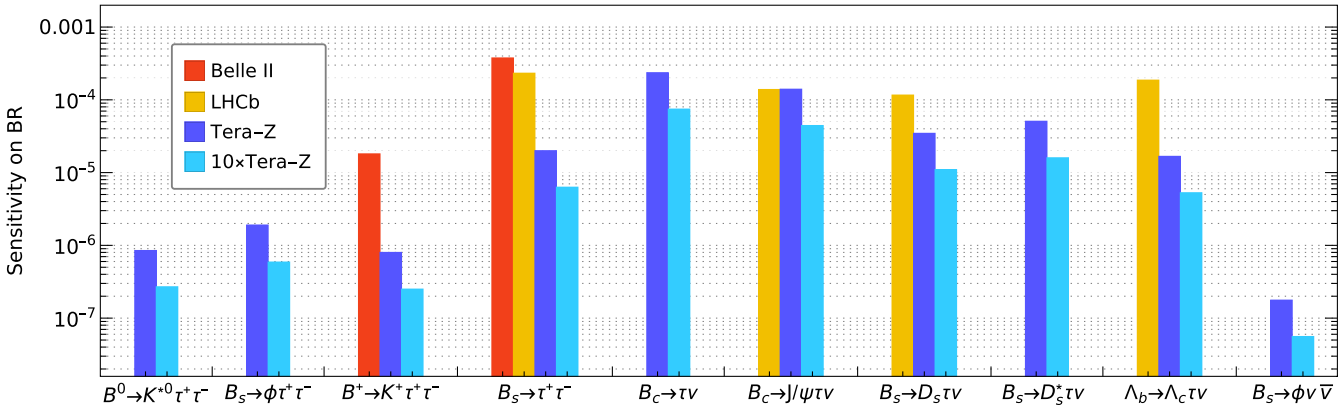

FIG. 25. Projected sensitivities of measuring the $b \to s\tau^+\tau^-$ [42], $b \to c\tau\nu(B_c \to \tau\nu)$ [77], $b \to c\tau\nu$ (this work), and $b \to s\nu\bar{\nu}$ [29] transitions at Tera-Z and 10 × Tera-Z. The sensitivities at Belle II at 50 ab^{-1} [23] and LHCb Upgrade II [24,78] have also been provided as a reference. Note that the sensitivities for each category might be based on different τ decay modes. For example, the LHCb sensitivities are generated by a combined analysis of $\tau^+ \to \pi^+\pi^-\pi^-(\pi^0)\nu$ and $\tau \to \mu\nu\bar{\nu}$.

where

$$O^{\tau}_{V_L} = [\bar{c}\gamma^{\mu}P_L b][\bar{\tau}\gamma_{\mu}P_L\nu], \qquad O^{\tau}_{V_R} = [\bar{c}\gamma^{\mu}P_R b][\bar{\tau}\gamma_{\mu}P_L\nu],$$
$$O^{\tau}_{S_L} = [\bar{c}P_L b][\bar{\tau}P_L\nu], \qquad O^{\tau}_{S_R} = [\bar{c}P_R b][\bar{\tau}P_L\nu],$$
$$O^{\tau}_{T} = [\bar{c}\sigma^{\mu\nu}b][\bar{\tau}\sigma_{\mu\nu}P_L\nu]. \tag{7.2}$$

The subscripts V_L, V_R, S_L, S_R, and T denote the left- and right-handed vector currents, left- and right-handed scalar currents, and the tensor current, respectively. Note, the SM contribution to the left-handed vector current is nontrivial due to W boson emission, leaving $C^{\tau}_{V_L}|_{\rm SM} = 1$ at $\mu_b = 4.8$ GeV. The superscript τ implies that any deviations of these Wilson coefficients from their SM predictions will violate the LFU explicitly.

Now we are able to calculate the LEFT predictions for R_{H_c}, which are given by (the details for these calculations are summarized in the Appendix)

$$\frac{R_{J/\psi}}{R^{\rm SM}_{J/\psi}} = 1.0 + {\rm Re}(0.12C^{\tau}_{S_L} + 0.034|C^{\tau}_{S_L}|^2 - 0.12C^{\tau}_{S_R} - 0.068C^{\tau}_{S_L}C^{\tau*}_{S_R} + 0.034|C^{\tau}_{S_R}|^2 - 5.3C^{\tau}_{T} + 13|C^{\tau}_{T}|^2 - 1.9C^{\tau}_{V_R}$$
$$- 0.12C^{\tau}_{S_L}C^{\tau*}_{V_R} + 0.12C^{\tau}_{S_R}C^{\tau*}_{V_R} + 5.8C^{\tau}_{T}C^{\tau*}_{V_R} + 1.0|C^{\tau}_{V_R}|^2 + 2.0\delta C^{\tau}_{V_L} + 0.12C^{\tau}_{S_L}\delta C^{\tau*}_{V_L} - 0.12C^{\tau}_{S_R}\delta C^{\tau*}_{V_L}$$
$$- 5.3C^{\tau}_{T}\delta C^{\tau*}_{V_L} - 1.9C^{\tau}_{V_R}\delta C^{\tau*}_{V_L} + 1.0|\delta C^{\tau}_{V_L}|^2), \tag{7.3}$$

$$\frac{R_{D_s}}{R^{\rm SM}_{D_s}} = 1.0 + {\rm Re}(1.6C^{\tau}_{S_L} + 1.2|C^{\tau}_{S_L}|^2 + 1.6C^{\tau}_{S_R} + 2.4C^{\tau}_{S_L}C^{\tau*}_{S_R} + 1.2|C^{\tau}_{S_R}|^2 + 1.4C^{\tau}_{T} + 1.4|C^{\tau}_{T}|^2 + 2.0C^{\tau}_{V_R} + 1.6C^{\tau}_{S_L}C^{\tau*}_{V_R}$$
$$+ 1.6C^{\tau}_{S_R}C^{\tau*}_{V_R} + 1.4C^{\tau}_{T}C^{\tau*}_{V_R} + 1.0|C^{\tau}_{V_R}|^2 + 2.0\delta C^{\tau}_{V_L} + 1.6C^{\tau}_{S_L}\delta C^{\tau*}_{V_L} + 1.6C^{\tau}_{S_R}\delta C^{\tau*}_{V_L} + 1.4C^{\tau}_{T}\delta C^{\tau*}_{V_L}$$
$$+ 2.0C^{\tau}_{V_R}\delta C^{\tau*}_{V_L} + 1.0|\delta C^{\tau}_{V_L}|^2), \tag{7.4}$$

$$\frac{R_{D^*_s}}{R^{\rm SM}_{D^*_s}} = 1.0 + {\rm Re}(0.085C^{\tau}_{S_L} + 0.026|C^{\tau}_{S_L}|^2 - 0.085C^{\tau}_{S_R} - 0.052C^{\tau}_{S_L}C^{\tau*}_{S_R} + 0.026|C^{\tau}_{S_R}|^2 - 4.6C^{\tau}_{T} + 15|C^{\tau}_{T}|^2 - 1.8C^{\tau}_{V_R}$$
$$- 0.085C^{\tau}_{S_L}C^{\tau*}_{V_R} + 0.085C^{\tau}_{S_R}C^{\tau*}_{V_R} + 6.4C^{\tau}_{T}C^{\tau*}_{V_R} + 1.0|C^{\tau}_{V_R}|^2 + 2.0\delta C^{\tau}_{V_L} + 0.085C^{\tau}_{S_L}\delta C^{\tau*}_{V_L} - 0.085C^{\tau}_{S_R}\delta C^{\tau*}_{V_L}$$
$$- 4.6C^{\tau}_{T}\delta C^{\tau*}_{V_L} - 1.8C^{\tau}_{V_R}\delta C^{\tau*}_{V_L} + 1.0|\delta C^{\tau}_{V_L}|^2), \tag{7.5}$$

$$\frac{R_{\Lambda_c}}{R^{\rm SM}_{\Lambda_c}} = 1.0 + {\rm Re}(0.39C^{\tau}_{S_L} + 0.34|C^{\tau}_{S_L}|^2 + 0.49C^{\tau}_{S_R} + 0.61C^{\tau}_{S_L}C^{\tau*}_{S_R} + 0.34|C^{\tau}_{S_R}|^2 + 1.1C^{\tau}_{T} + 12|C^{\tau}_{T}|^2 - 0.71C^{\tau}_{V_R}$$
$$+ 0.49C^{\tau}_{S_L}C^{\tau*}_{V_R} + 0.39C^{\tau}_{S_R}C^{\tau*}_{V_R} - 1.7C^{\tau}_{T}C^{\tau*}_{V_R} + 1.0|C^{\tau}_{V_R}|^2 + 2.0\delta C^{\tau}_{V_L} + 0.39C^{\tau}_{S_L}\delta C^{\tau*}_{V_L} + 0.49C^{\tau}_{S_R}\delta C^{\tau*}_{V_L}$$
$$+ 1.1C^{\tau}_{T}\delta C^{\tau*}_{V_L} - 0.71C^{\tau}_{V_R}\delta C^{\tau*}_{V_L} + 1.0|\delta C^{\tau}_{V_L}|^2). \tag{7.6}$$

We also include the measurement of ${\rm BR}(B_c \to \tau\nu)$ in this analysis. This channel is sensitive to the axial vector $(C^{\tau}_{V_L} - C^{\tau}_{V_R})$ and pseudoscalar $(C^{\tau}_{S_L} - C^{\tau}_{S_R})$ combinations only. Here we take the results reported in [41],

$$\frac{{\rm BR}(B_c \to \tau\nu)}{{\rm BR}(B_c \to \tau\nu)^{\rm SM}} = 1.0 + {\rm Re}(7.1C^{\tau}_{S_L} + 13|C^{\tau}_{S_L}|^2 - 7.1C^{\tau}_{S_R} - 26C^{\tau}_{S_L}C^{\tau*}_{S_R} + 13|C^{\tau}_{S_R}|^2 - 2.0C^{\tau}_{V_R} - 7.1C^{\tau}_{S_L}C^{\tau*}_{V_R} + 7.1C^{\tau}_{S_R}C^{\tau*}_{V_R}$$
$$+ 1.0|C^{\tau}_{V_R}|^2 + 2.0\delta C^{\tau}_{V_L} + 7.1C^{\tau}_{S_L}\delta C^{\tau*}_{V_L} - 7.1C^{\tau}_{S_R}\delta C^{\tau*}_{V_L} - 2.0C^{\tau}_{V_R}\delta C^{\tau*}_{V_L} + 1.0|\delta C^{\tau}_{V_L}|^2). \tag{7.7}$$

Notably, these channels represent four types of the $b \to c\tau\nu$ transitions: the vector type ($R_{J/\psi}$ and $R_{D^*_s}$), the pseudoscalar type (R_{D_s}), the baryon type (R_{Λ_c}), and the annihilation type [${\rm BR}(B_c \to \tau\nu)$]. The responses to the NP tend to be aligned for the channels of the same types, as indicated by Eqs. (7.3) and (7.5). The difference between them mainly arises from meson masses and decay form factors, which are usually small. So it is important to combine all four types of measurements for more accurate EFT interpretation.

2. $b \to s\tau^+\tau^-$

In the 6D LEFT, the $b \to s\tau^+\tau^-$ transitions are described by

$$\mathcal{L}^{\rm LE}_{b\to s\tau^+\tau^-} = \frac{4G_F V_{tb}V^*_{ts}}{\sqrt{2}}[(C^{\tau}_9|_{\rm SM} + \delta C^{\tau}_9)O^{\tau}_9$$
$$+ (C^{\tau}_{10}|_{\rm SM} + \delta C^{\tau}_{10})O^{\tau}_{10} + C'^{\tau}_9 O'^{\tau}_9 + C'^{\tau}_{10}O'^{\tau}_{10}$$
$$+ C^{\tau}_S O^{\tau}_S + C'^{\tau}_S O'^{\tau}_S + C^{\tau}_P O^{\tau}_P + C'^{\tau}_P O'^{\tau}_P$$
$$+ C^{\tau}_T O^{\tau}_T + C^{\tau}_{T5}O^{\tau}_{T5}] + {\rm H.c.}, \tag{7.8}$$

where

$$
\begin{aligned}
O^{\tau}_{9(10)} &= \frac{\alpha}{4\pi}[\bar{s}\gamma^{\mu}P_L b][\bar{\tau}\gamma_{\mu}(\gamma^5)\tau],\\
O'^{\tau}_{9(10)} &= \frac{\alpha}{4\pi}[\bar{s}\gamma^{\mu}P_R b][\bar{\tau}\gamma_{\mu}(\gamma^5)\tau],\\
O^{\tau}_{S(P)} &= \frac{\alpha}{4\pi}[\bar{s}P_R b][\bar{\tau}(\gamma^5)\tau],\\
O'^{\tau}_{S(P)} &= \frac{\alpha}{4\pi}[\bar{s}P_L b][\bar{\tau}(\gamma^5)\tau],\\
O^{\tau}_{T(T5)} &= \frac{\alpha}{4\pi}[\bar{s}\sigma_{\mu\nu} b][\bar{\tau}\sigma^{\mu\nu}(\gamma^5)\tau].
\end{aligned}
\tag{7.9}
$$

As it occurs to the left-handed vector current of $b \to c\tau\nu$, the SM contributes to O^{τ}_9 and O^{τ}_{10}. The contributions include the gluon penguin diagrams with extra quark loop and the radiative $b \to s\gamma^* \to s\tau^+\tau^-$ processes, yielding $C^{\tau}_{9(10)}|_{\rm SM} \approx 4.07(-4.31)$ at $\mu_b = 4.8$ GeV [79]. α is the running fine-structure constant. Note, we tolerate the abuse of notation here for the O^{τ}_T operator and its Wilson coefficient. This notation has been used for the tensor-current operator in the $b \to c\tau\nu$ LEFT defined in Eq. (7.1). We will see later that both O^{τ}_T and O^{τ}_{T5} in this Lagrangian are irrelevant to the SMEFT interpretation.

The LEFT predictions for $\mathrm{BR}(B^+ \to K^+\tau^+\tau^-)$, $\mathrm{BR}(B^0 \to K^{*0}\tau^+\tau^-)$, $\mathrm{BR}(B_s \to \phi\tau^+\tau^-)$, and $\mathrm{BR}(B_s \to \tau^+\tau^-)$ are given as follows[6]:

$$
\begin{aligned}
\frac{\mathrm{BR}(B^+ \to K^+\tau^+\tau^-)}{\mathrm{BR}(B^+ \to K^+\tau^+\tau^-)^{\rm SM}} = 1.0 &+ \mathrm{Re}(-0.35C'^{\tau}_{10} + 0.041|C'^{\tau}_{10}|^2 + 0.14C'^{\tau}_{9} + 0.019|C'^{\tau}_{9}|^2 - 0.34C^{\tau}_{P} + 0.079C'^{\tau}_{10}C^{\tau *}_{P}\\
&+ 0.043|C^{\tau}_{P}|^2 - 0.34C'^{\tau}_{P} + 0.079C'^{\tau}_{10}C'^{\tau *}_{P} + 0.086C^{\tau}_{P}C'^{\tau *}_{P} + 0.043|C'^{\tau}_{P}|^2 + 0.014|C^{\tau}_{S}|^2\\
&+ 0.027C^{\tau}_{S}C'^{\tau *}_{S} + 0.014|C'^{\tau}_{S}|^2 + 0.018|C^{\tau}_{T5}|^2 + 0.37C^{\tau}_{T} + 0.10C'^{\tau}_{9}C^{\tau *}_{T} + 0.15|C^{\tau}_{T}|^2\\
&- 0.35\delta C^{\tau}_{10} + 0.082C'^{\tau}_{10}\delta C^{\tau *}_{10} + 0.079C^{\tau}_{P}\delta C^{\tau *}_{10} + 0.079C'^{\tau}_{P}\delta C^{\tau *}_{10} + 0.041|\delta C^{\tau}_{10}|^2 + 0.14\delta C^{\tau}_{9}\\
&+ 0.038C'^{\tau}_{9}\delta C^{\tau *}_{9} + 0.10C^{\tau}_{T}\delta C^{\tau *}_{9} + 0.019|\delta C^{\tau}_{9}|^2),
\end{aligned}
\tag{7.10}
$$

$$
\begin{aligned}
\frac{\mathrm{BR}(B^0 \to K^{*0}\tau^+\tau^-)}{\mathrm{BR}(B^0 \to K^{*0}\tau^+\tau^-)^{\rm SM}} = 1.0 &+ \mathrm{Re}(0.13C'^{\tau}_{10} + 0.018|C'^{\tau}_{10}|^2 - 0.31C'^{\tau}_{9} + 0.059|C'^{\tau}_{9}|^2 - 0.057C^{\tau}_{P} - 0.013C'^{\tau}_{10}C^{\tau *}_{P}\\
&+ 0.0062|C^{\tau}_{P}|^2 + 0.057C'^{\tau}_{P} + 0.013C'^{\tau}_{10}C'^{\tau *}_{P} - 0.012C^{\tau}_{P}C'^{\tau *}_{P} + 0.0062|C'^{\tau}_{P}|^2 + 0.0014|C^{\tau}_{S}|^2\\
&- 0.0029C^{\tau}_{S}C'^{\tau *}_{S} + 0.0014|C'^{\tau}_{S}|^2 + 1.3C^{\tau}_{T5} - 0.39C'^{\tau}_{9}C^{\tau *}_{T5} + 0.77|C^{\tau}_{T5}|^2 + 0.22C^{\tau}_{T} + 0.068C'^{\tau}_{9}C^{\tau *}_{T}\\
&+ 0.24|C^{\tau}_{T}|^2 - 0.15\delta C^{\tau}_{10} - 0.030C'^{\tau}_{10}\delta C^{\tau *}_{10} + 0.013C^{\tau}_{P}\delta C^{\tau *}_{10} - 0.013C'^{\tau}_{P}\delta C^{\tau *}_{10} + 0.018|\delta C^{\tau}_{10}|^2\\
&+ 0.40\delta C^{\tau}_{9} - 0.090C'^{\tau}_{9}\delta C^{\tau *}_{9} + 0.39C^{\tau}_{T5}\delta C^{\tau *}_{9} + 0.068C^{\tau}_{T}\delta C^{\tau *}_{9} + 0.059|\delta C^{\tau}_{9}|^2),
\end{aligned}
\tag{7.11}
$$

$$
\begin{aligned}
\frac{\mathrm{BR}(B_s \to \phi\tau^+\tau^-)}{\mathrm{BR}(B_s \to \phi\tau^+\tau^-)^{\rm SM}} = 1.0 &+ \mathrm{Re}(0.14C'^{\tau}_{10} + 0.017|C'^{\tau}_{10}|^2 - 0.33C'^{\tau}_{9} + 0.060|C'^{\tau}_{9}|^2 - 0.057C^{\tau}_{P} - 0.013C'^{\tau}_{10}C^{\tau *}_{P}\\
&+ 0.0062|C^{\tau}_{P}|^2 + 0.057C'^{\tau}_{P} + 0.013C'^{\tau}_{10}C'^{\tau *}_{P} - 0.012C^{\tau}_{P}C'^{\tau *}_{P} + 0.0062|C'^{\tau}_{P}|^2 + 0.0014|C^{\tau}_{S}|^2\\
&- 0.0028C^{\tau}_{S}C'^{\tau *}_{S} + 0.0014|C'^{\tau}_{S}|^2 + 1.4C^{\tau}_{T5} - 0.41C'^{\tau}_{9}C^{\tau *}_{T5} + 0.80|C^{\tau}_{T5}|^2 + 0.17C^{\tau}_{T} + 0.054C'^{\tau}_{9}C^{\tau *}_{T}\\
&+ 0.21|C^{\tau}_{T}|^2 - 0.15\delta C^{\tau}_{10} - 0.031C'^{\tau}_{10}\delta C^{\tau *}_{10} + 0.013C^{\tau}_{P}\delta C^{\tau *}_{10} - 0.013C'^{\tau}_{P}\delta C^{\tau *}_{10} + 0.018|\delta C^{\tau}_{10}|^2\\
&+ 0.40\delta C^{\tau}_{9} - 0.097C'^{\tau}_{9}\delta C^{\tau *}_{9} + 0.41C^{\tau}_{T5}\delta C^{\tau *}_{9} + 0.054C^{\tau}_{T}\delta C^{\tau *}_{9} + 0.060|\delta C^{\tau}_{9}|^2),
\end{aligned}
\tag{7.12}
$$

$$
\begin{aligned}
\frac{\mathrm{BR}(B_s \to \tau^+\tau^-)}{\mathrm{BR}(B_s \to \tau^+\tau^-)^{\rm SM}} = 1.0 &+ \mathrm{Re}(0.46C'^{\tau}_{10} + 0.054|C'^{\tau}_{10}|^2 - 0.78C^{\tau}_{P} - 0.18C'^{\tau}_{10}C^{\tau *}_{P} + 0.15|C^{\tau}_{P}|^2 + 0.78C'^{\tau}_{P} + 0.18C'^{\tau}_{10}C'^{\tau *}_{P}\\
&- 0.31C^{\tau}_{P}C'^{\tau *}_{P} + 0.15|C'^{\tau}_{P}|^2 + 0.086|C^{\tau}_{S}|^2 - 0.17C^{\tau}_{S}C'^{\tau *}_{S} + 0.086|C'^{\tau}_{S}|^2 - 0.46\delta C^{\tau}_{10} - 0.11C'^{\tau}_{10}\delta C^{\tau *}_{10}\\
&+ 0.18C^{\tau}_{P}\delta C^{\tau *}_{10} - 0.18C'^{\tau}_{P}\delta C^{\tau *}_{10} + 0.054|\delta C^{\tau}_{10}|^2).
\end{aligned}
\tag{7.13}
$$

[6]These relations are slightly different from those in [80]. The main reason is that we have not taken a full consideration on the uncertainties of the decay form factors for simplicity. Moreover, unlike [80], where four LEFT operators are turned on, here we consider a total of 10 LEFT operators instead.

The collider phenomenology on the $b \to s\tau^+\tau^-$ transitions have been studied in various contexts [33,42,80]. Currently, the upper limits set by *BABAR* and LHCb for their branching ratios are $\sim\mathcal{O}(10^{-3})$ [81,82]. They are much higher than the SM predictions, which are typically $\sim\mathcal{O}(10^{-7})$. Recently, a systematic study performed in [42] indicates that these limits [except $\mathrm{BR}(B_s \to \tau^+\tau^-)$] can be improved to $\sim\mathcal{O}(10^{-7})$ at Tera-Z and even more for $10\times$ Tera-Z. The relevant sensitivity inputs on the $b \to s\tau^+\tau^-$ measurements at the Z pole will be mainly based on this paper.

3. $b \to s\bar{\nu}\nu$

In the 6D LEFT, the $b \to s\bar{\nu}\nu$ transitions are described by

$$\mathcal{L}^{\mathrm{LE}}_{b\to s\bar{\nu}\nu} = +\frac{4G_F V_{tb}V_{ts}^*}{\sqrt{2}}[(C_L^\nu|_{\mathrm{SM}} + \delta C_L^\nu)O_L^\nu + C_R^\nu O_R^\nu] + \mathrm{H.c.}, \tag{7.14}$$

where

$$O^\nu_{L(R)} = \frac{\alpha}{4\pi}[\bar{s}\gamma^\mu P_{L(R)} b][\bar{\nu}\gamma_\mu(1-\gamma^5)\nu]. \tag{7.15}$$

O_L^ν receives contributions from the SM at loop level. Combining the EW contributions and the next-to-leading-order QCD corrections yields $C_L^\nu|_{\mathrm{SM}} \approx -6.47$ [70]. Notably, the three flavors of neutrinos all contribute at colliders and are mutually indistinguishable. Here we assume a deviation from the SM prediction to be possible for the third generation only, as discussed above.

The LEFT predictions for $\mathrm{BR}(B^+ \to K^+\bar{\nu}\nu)$, $\mathrm{BR}(B^0 \to K^{*0}\bar{\nu}\nu)$, and $\mathrm{BR}(B_s \to \phi\bar{\nu}\nu)$ are given as follows [70]:

$$\begin{aligned}
\frac{\mathrm{BR}(B^+ \to K^+\bar{\nu}\nu)}{\mathrm{BR}(B^+ \to K^+\bar{\nu}\nu)^{\mathrm{SM}}} &= \frac{1}{3}[2 + (1-2\eta)\epsilon^2],\\
\frac{\mathrm{BR}(B^0 \to K^{*0}\bar{\nu}\nu)}{\mathrm{BR}(B^0 \to K^{*0}\bar{\nu}\nu)^{\mathrm{SM}}} &= \frac{1}{3}[2 + (1+\kappa_{K^{*0}}\eta)\epsilon^2],\\
\frac{\mathrm{BR}(B_s \to \phi\bar{\nu}\nu)}{\mathrm{BR}(B_s \to \phi\bar{\nu}\nu)^{\mathrm{SM}}} &= \frac{1}{3}[2 + (1+\kappa_{\phi}\eta)\epsilon^2],
\end{aligned} \tag{7.16}$$

where $\kappa_{K^{*0}} = 1.34$ [70], $\kappa_\phi = 1.56$ [29], and

$$\epsilon = \frac{\sqrt{|C_L^\nu|^2 + |C_R^\nu|^2}}{C_L^\nu|_{\mathrm{SM}}}, \qquad \eta = \frac{-\mathrm{Re}(C_L^\nu C_R^{\nu *})}{|C_L^\nu|^2 + |C_R^\nu|^2}. \tag{7.17}$$

At Belle II with 50 ab^{-1}, relative sensitivities up to 11% and 9.6% could be achieved for $\mathrm{BR}(B^+ \to K^+\bar{\nu}\nu)$ and $\mathrm{BR}(B^0 \to K^{*0}\bar{\nu}\nu)$, respectively [23]. The CEPC may constrain $\mathrm{BR}(B_s \to \phi\bar{\nu}\nu)$ with a relative sensitivity ~1.78%, as reported in [29].

B. SMEFT and matching

The SMEFT respects the SM gauge symmetries, namely, $SU(3)_c \times SU(2)_L \times U(1)_Y$. Its 6D operators contributing to the $b \to c\tau\nu$, $b \to s\tau^+\tau^-$, and $b \to s\bar{\nu}\nu$ transitions are given by [83,84]

$$\begin{aligned}
\mathcal{L}^{\mathrm{SM}} \supset \frac{1}{\Lambda^2}\sum_{i,j,k,l}&([C^{(1)}_{\ell q}]_{ijkl}[O^{(1)}_{\ell q}]_{ijkl} + [C^{(3)}_{\ell q}]_{ijkl}[O^{(3)}_{\ell q}]_{ijkl} + [C_{ed}]_{ijkl}[O_{ed}]_{ijkl} + [C_{\ell d}]_{ijkl}[O_{\ell d}]_{ijkl} + [C_{qe}]_{ijkl}[O_{qe}]_{ijkl}\\
&+ [C_{\ell edq}]_{ijkl}[O_{\ell edq}]_{ijkl} + [C^{(1)}_{\ell equ}]_{ijkl}[O^{(1)}_{\ell equ}]_{ijkl} + [C^{(3)}_{\ell equ}]_{ijkl}[O^{(3)}_{\ell equ}]_{ijkl}) + \mathrm{H.c.},
\end{aligned} \tag{7.18}$$

where

$$\begin{aligned}
[O^{(1)}_{\ell q}]_{ijkl} &= [\bar{L}_i\gamma_\mu L_j][\bar{Q}_k\gamma^\mu Q_l],\\
[O^{(3)}_{\ell q}]_{ijkl} &= [\bar{L}_i\gamma_\mu\sigma^a L_j][\bar{Q}_k\gamma^\mu\sigma^a Q_l],\\
[O_{ed}]_{ijkl} &= [\bar{\ell}_i\gamma_\mu\ell_j][\bar{d}_k\gamma^\mu d_l],\\
[O_{\ell d}]_{ijkl} &= [\bar{L}_i\gamma_\mu L_j][\bar{d}_k\gamma^\mu d_l],\\
[O_{qe}]_{ijkl} &= [\bar{\ell}_i\gamma_\mu\ell_j][\bar{Q}_k\gamma^\mu Q_l],\\
[O_{\ell edq}]_{ijkl} &= [\bar{L}^I_i\ell_j][\bar{d}_k Q^I_l],\\
[O^{(1)}_{\ell equ}]_{ijkl} &= [\bar{L}^I_i\ell_j]\epsilon_{IJ}[\bar{Q}^J_k u_l],\\
[O^{(3)}_{\ell equ}]_{ijkl} &= [\bar{L}^I_i\sigma_{\mu\nu}\ell_j]\epsilon_{IJ}[\bar{Q}^J_k\sigma^{\mu\nu}u_l],
\end{aligned} \tag{7.19}$$

with i, j, k, and l denoting the quark/lepton flavor and I and J representing the $SU(2)_L$ symmetry index. The scale

TABLE XVI. SMEFT operators that are relevant to this study. In the second column, the operators are shown in the down basis, where $Q_i = \{V^*_{ji}u_j, d_i\}$ and $L_i = \{\nu_i, \ell_i\}$.

SMEFT operators	SMEFT operators (down basis)
$[O^{(1)}_{lq}]_{3332}$	$[\bar{\nu}\gamma^\mu P_L\nu + \bar{\tau}\gamma^\mu P_L\tau][\bar{b}\gamma_\mu P_L s]$
$[O^{(3)}_{lq}]_{3332}$	$2V^*_{cs}[\bar{\nu}\gamma^\mu P_L\tau][\bar{b}\gamma_\mu P_L c] - [\bar{\nu}\gamma^\mu P_L\nu - \bar{\tau}\gamma^\mu P_L\tau][\bar{b}\gamma_\mu P_L s]$
$[O_{ed}]_{3332}$	$[\bar{\tau}\gamma^\mu P_R\tau][\bar{b}\gamma_\mu P_R s]$
$[O_{ld}]_{3332}$	$[\bar{\nu}\gamma^\mu P_L\nu + \bar{\tau}\gamma^\mu P_L\tau][\bar{b}\gamma_\mu P_R s]$
$[O_{qe}]_{3332}$	$[\bar{\tau}\gamma^\mu P_R\tau][\bar{b}\gamma_\mu P_L s]$
$[O_{ledq}]_{3332}$	$V^*_{cs}[\bar{\nu}P_R\tau][\bar{b}P_L c] + [\bar{\tau}P_R\tau][\bar{b}P_L s]$
$[O_{ledq}]_{3323}$	$[\bar{\tau}P_R\tau][\bar{s}P_L b]$
$[O^{(1)}_{lequ}]_{3332}$	$V^*_{cs}[\bar{\nu}P_R\tau][\bar{b}P_R c]$
$[O^{(3)}_{lequ}]_{3332}$	$V^*_{cs}[\bar{\nu}\sigma^{\mu\nu}P_R\tau][\bar{b}\sigma_{\mu\nu}P_R c]$

$\Lambda \gtrsim$ the electroweak scale is the cutoff of EFT, corresponding to the scale of new physics. For concreteness, we focus on the operators unsuppressed by the Cabibbo–Kobayashi–Maskawa elements, i.e., the ones containing exactly one bottom quark and one strange or one charm quark. As only the third-generation leptons are allowed to deviate their physics from the SM, there are nine 6D operators of SMEFT to consider in total. These operators are summarized in Table XVI.

We calculate the SMEFT and LEFT Wilson coefficients with RG running using the WILSON package [85]. These two theories are then matched at the scale of m_Z by demanding

$$\mathcal{L}^{\mathrm{SM}}(m_Z) = \mathcal{L}^{\mathrm{LE}}(m_Z). \tag{7.20}$$

The LEFT operators $O^{\tau}_{V_R}$ for $b \to c\tau\nu$ and O^{τ}_{T} and O^{τ}_{T5} for $b \to s\tau^+\tau^-$ are irrelevant to matching and hence are turned off. As for the left 14 LEFT operators, only nine are

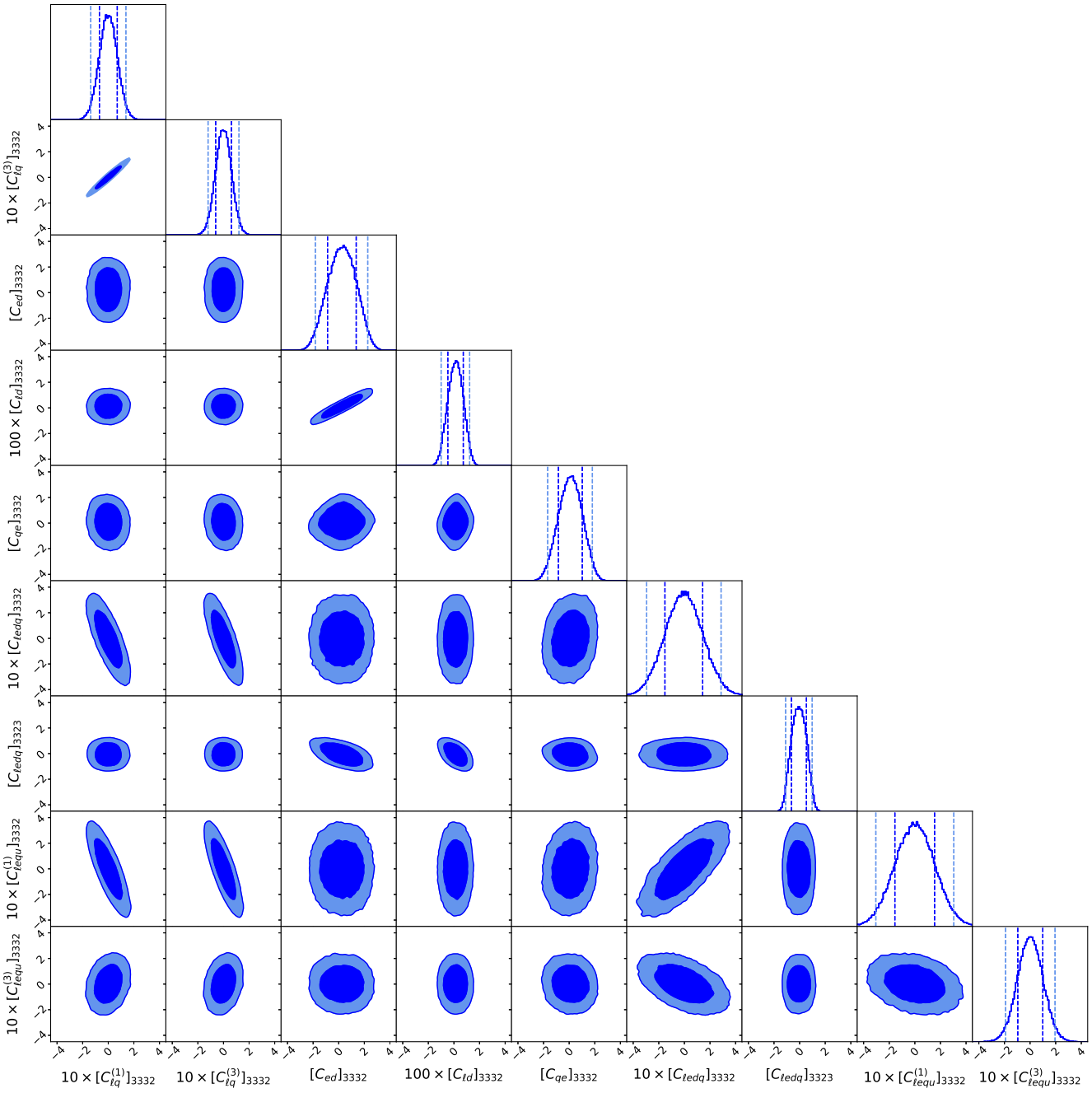

FIG. 26. 2D posterior distributions of the SMEFT Wilson coefficients (at $\Lambda = 10$ TeV) at Tera-Z, with 68% (dark blue) and 95% (light blue) confidence levels. The fitting inputs are summarized in Table XV.

independent due to the relations inherited from the SM gauge symmetries. We take $C^{\tau}_{S_L}$ and C^{τ}_{T} from Eq. (7.1), δC^{τ}_{9}, C'^{τ}_{9}, δC^{τ}_{10}, C'^{τ}_{10}, C^{τ}_{S}, C'^{τ}_{S} from Eq. (7.8), and δC^{ν}_{L} from Eq. (7.14) to define the basis of the constrained LEFT Wilson coefficients without losing any generality. Then we have

$$
\begin{aligned}
[C^{(i)*}_{\ell q}]_{3332} &= \frac{G_F \alpha V_{tb} V^*_{ts} \Lambda^2}{2\sqrt{2}\pi}(\delta C^{\tau}_{9} - \delta C^{\tau}_{10} \pm 2\delta C^{\nu}_{L}), \\
i &= \{1,3\}, \\
[C^{*}_{ed(\ell d)}]_{3332} &= \frac{G_F \alpha V_{tb} V^*_{ts} \Lambda^2}{\sqrt{2}\pi}(C'^{\tau}_{9} \pm C'^{\tau}_{10}), \\
[C^{*}_{qe}]_{3332} &= \frac{G_F \alpha V_{tb} V^*_{ts} \Lambda^2}{\sqrt{2}\pi}(\delta C^{\tau}_{9} + \delta C^{\tau}_{10}), \\
[C^{*}_{\ell edq}]_{3332} &= \frac{\sqrt{2} G_F \alpha V_{tb} V^*_{ts} \Lambda^2}{\pi} C^{\tau}_{S}, \\
[C_{\ell edq}]_{3323} &= \frac{\sqrt{2} G_F \alpha V_{tb} V^*_{ts} \Lambda^2}{\pi} C^{\tau\prime}_{S}, \\
[C^{(1)*}_{\ell equ}]_{3332} &= -\frac{4 G_F V_{cb} \Lambda^2}{\sqrt{2} V_{cs}} C^{\tau}_{S_L}, \\
[C^{(3)*}_{\ell equ}]_{3332} &= -\frac{4 G_F V_{cb} \Lambda^2}{\sqrt{2} V_{cs}} C^{\tau}_{T}.
\end{aligned}
\tag{7.21}
$$

At the matching scale around m_Z, the other LEFT Wilson coefficients then satisfy the following relations:

$$
\begin{aligned}
C^{\tau}_{S_R} &= -\frac{\alpha V_{tb} V^*_{ts} V_{cs}}{2\pi V_{cb}} C^{\tau}_{S}, \\
\delta C^{\tau}_{V_L} &= \frac{\alpha V_{tb} V^*_{ts} V_{cs}}{4\pi V_{cb}}(\delta C^{\tau}_{10} - \delta C^{\tau}_{9} + 2\delta C^{\nu}_{L}), \\
C^{\tau}_{P} &= -C^{\tau}_{S}, \qquad C'^{\tau}_{P} = C'^{\tau}_{S}, \\
C^{\nu}_{R} &= \frac{1}{2}(C'^{\tau}_{9} - C'^{\tau}_{10}).
\end{aligned}
\tag{7.22}
$$

C. SMEFT interpretation

To generate the posterior distributions of the SMEFT Wilson coefficients at the cutoff scale, we sample a total of 10^5 points in the space of $\mathcal{L}^{\rm LE}(\mu_b)$ with the EMCEE package [86] to fit the data in Table XV. These points are then projected to the space of $\mathcal{L}^{\rm SM}(\Lambda = 10\ \text{TeV})$, using the WILSON package for RG running [85], where marginalization is performed with the CORNER package [87]. For the convenience of analysis, we implement the matching conditions at the scale of μ_b instead [88]. The matching conditions are subject to an effect of RG running. However, the relations in Eq. (7.22) are preserved by the QCD effect [89,90], as the operators involved in each relation share identical quark spinor structures. At one-loop level, they are deformed by electroweak coupling and quadratic product of Wilson coefficients only. We thus take Eq. (7.22) to be an approximation of the matching conditions at μ_b. Numerical work indicates that, for the data sampling in such a manner, the caused deviation from Eq. (7.22) at the scale of m_Z is, at most, at a level of several percents.

We present the 2D posterior distributions of the SMEFT Wilson coefficients (at $\Lambda = 10$ TeV) at Tera-Z in Fig. 26 and their 1D posterior distributions at Tera-Z and $10\times$ Tera-Z in Fig. 27. These parameters are constrained to be $\lesssim\mathcal{O}(1)$ with 68% confidence level by the Tera-Z, but not at a comparable level. As summarized in Table XV (also see Fig. 25), the measurements of $b \to c\tau\nu$ transitions demonstrate a universally high precision [though the precisions for $R_{J/\psi}$ and $\mathrm{BR}(B_c \to \tau\nu)$ are one order of magnitude lower than those of $R_{D_s^{(*)}}$ and R_{Λ_c} due to the relatively low production rate of B_c mesons]. The relative precision for measuring $\mathrm{BR}(B_s \to \phi\bar{\nu}\nu)$ is also high, though the SM prediction for its absolute value is tiny. The three operators $[O_{ed}]_{3332}$, $[O_{qe}]_{3332}$, and $[O_{\ell edq}]_{3323}$ do not contribute to any of them except the $b \to s\tau\tau$ transitions. So the constraints

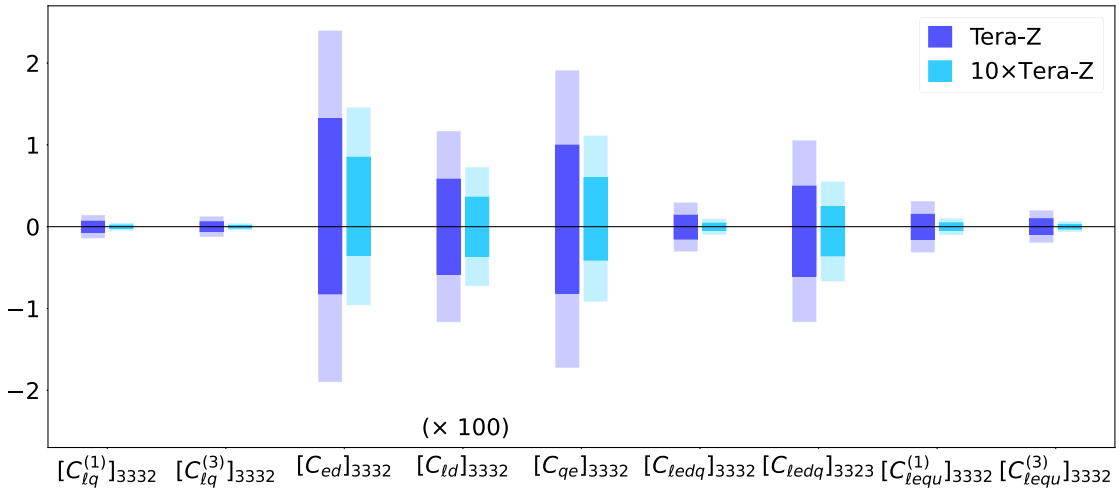

FIG. 27. 1D posterior distributions of the SMEFT Wilson coefficients (at $\Lambda = 10$ TeV) at Tera-Z and $10\times$ Tera-Z, with 68% (dark) and 95% (light) confidence levels. The fitting inputs are summarized in Table XV.

for their Wilson coefficients are a few times weaker than those of the other ones.

VIII. SUMMARY AND CONCLUSION

The LFU is one of the hypothetical principles in the SM and should be measured with a precision as high as possible such that the physics violating this principle can be fully tested. The future Z factories provide a great opportunity to perform this task. At Z pole, the b hadrons are produced to be highly boosted, with relatively few contaminations from the environment. A higher precision of measuring particle energy and vertex and efficiency for reconstructing the signal events thus can be achieved, compared to those at Belle II and LHCb. For the $H_b \to H_c\tau(\mu)\nu$ measurements studied in this paper, we have developed an algorithm to reconstruct H_c and H_b, where the total four-momentum of neutrinos or the missing momentum in each signal event can be inferred, by employing these advantages. Moreover, heavy b hadrons such as Λ_b can be produced at Z pole with significant statistics. This opens new avenues to test the LFU. If the LFU violation is observed, such a multiplicity of signal modes may greatly benefit exploring the nature of LFU-violating new physics, e.g., parity and spin of the relevant mediators.

The study performed in this paper was mainly based on the $b \to c\tau(\mu)\nu$ transitions. Concretely, we analyzed the sensitivity of measuring R_{H_c} in four representative scenarios: $B_c \to J/\phi\tau(\mu)\nu$, $B_s \to D_s^{(*)}\tau(\mu)\nu$, and $\Lambda_b \to \Lambda_c\tau(\mu)\nu$, with $\tau \to \mu\nu\bar{\nu}$. The statistics for all of them at Belle II are significantly lower than those expected to achieve at the future Z factories. Because of the relatively high efficiency for event reconstruction (see, e.g., the upper-left panel of Figs. 3, 7, and 12), we are allowed to introduce the invariant mass of off-shell W boson q^2 and missing momenta $m^2_{\rm miss}$ and the minimal distance between the μ_3 track and the H_b decay vertex $S_{\rm SV}$ to distinguish the μ- and τ-mode signal events which serve as mutual backgrounds in their respective measurements. These observables can be also applied to discriminate the signals from the universal backgrounds. The universal backgrounds have been classified into five categories in this study. Despite their multiplicity, these backgrounds tend to be less isolated compared to the signal B_c mesons. So we also turned on a set of isolation measures to further suppress these backgrounds. Finally, these observables and some others are integrated using the BDT tool in the sensitivity analysis, yielding $S/B \gtrsim 0.3$ for various relevant scenarios.

The algorithm developed for reconstructing H_c and H_b relies on the messages of tracks and decay vertex significantly. So we further explored the robustness of sensitivity against the tracker performance and the potential improvement with a better tracker resolution. We showed that the variation of tracker resolution, which is manifested as vertex noise, from a perfect case to more conservative scenarios causes a change of $\sim\mathcal{O}(10\%)$ to sensitivity. Specifically, the precision of measuring $R_{J/\psi}$ could be improved more with the reduced vertex noise, while the measurement of R_{Λ_c} tends to be more robust against the variation of vertex noise level. The reason is simple. Unlike the Λ_b one, the B_c vertex can be well-approximated by the H_c vertex. This leads to more accurate reconstruction for B_c, which in turn leaves smaller space to resolve the variation of vertex noise. In addition, we investigated the impacts of ECAL energy threshold on soft photon tagging. The latter plays a central role in the $R_{D_s^{(*)}}$ measurements, as the separation between D_s and D_s^* relies on the resonance reconstruction of $D_s^* \to D_s\gamma$. We found that, as the photon energy threshold decreases, the precisions of measuring $R_{D_s^{(*)}}$ could be improved by $\sim\mathcal{O}(10\%)$ and meanwhile the correlation between them gets weakened. Finally, for the first time we scrutinized the effect of event shape in distinguishing the signal and background events. We considered the $R_{J/\psi}$ measurement as an example, as multiple heavy-flavor quarks can be produced in the $Z \to B_c + X$ events. The message beyond the B_c decays indeed yields a suppression of the background events, especially the ones from the back-to-back $Z \to b\bar{b}$ decays. By including the FW moments as the inputs for the BDT analysis, we showed that the signal-to-background ratio is increased by several percents, and the signal significance can be slightly improved.

Finally, we have interpreted in the SMEFT the projected sensitivities of measuring R_{H_c}, together with the $b \to s\tau^+\tau^-$ and $b \to s\nu\bar{\nu}$ observables, at the future Z factories. These measurements are performed at an energy scale well below the SMEFT cutoff. So we included the effects of the RG running in this analysis, with the EW-scale matching conditions being implemented. Because of the generic constraints of symmetries for the SMEFT, these observables are entangled with each other. For example, the operator $[O_{lq}^{(3)}]_{3332}$ correlates the measurements of all three types of relevant FCNC/FCCC transitions (see Table XVI) at the low-energy scale. The MCMC posterior distributions for the SMEFT Wilson coefficients then indicate—for $\lesssim\mathcal{O}(1)$ Wilson coefficients—the LFU-violating physics can be probed up to a scale $\sim\mathcal{O}(10)$ TeV at Tera-Z.

Notably, to demonstrate the sensitivity potential of testing the LFU at the future Z factories, we have taken the $b \to c\tau\nu$ measurements with $\tau \to \mu\nu\bar{\nu}$ as a benchmark. Such a scenario is representative but not complete. Actually, the accuracy of electron identification in a Z factory is also high. One can thus generalize the analysis to the mode of $\tau \to e\nu\bar{\nu}$ straightforwardly, to further improve the measurement precision. Alternative decay modes for H_c could be also considered for the R_{H_c} measurements, if we can reconstruct the H_c hadron well. By including electron modes, we will double the effective statistics for the $R_{D_s^{(*)}}$ and R_{Λ_c} measurements and quadruple that for the

$R_{J/\psi}$ measurement. By including hadronic modes, we will gain more. A combination of these analyses will certainly generate positive impacts on the sensitivity reach of the LFU tests at the future Z factories. Moreover, the strategies developed here could be applied to other tasks at the Z pole also, such as the differential and CP measurements in semileptonic b-hadron decays. We leave these explorations to future work.

ACKNOWLEDGMENTS

We would like to thank Manqi Ruan for highly valuable and constructive comments on the studies performed in Sec. VI "Impacts of Detector Performance and Event Shape." We would also thank Lorenzo Calibbi, Jibo He, Fengkun Guo, and Wei Wang for useful discussions. This work is supported partly by the Area of Excellence (AoE) under the Grant No. AoE/P-404/18-3 and partly by the General Research Fund (GRF) under Grant No. 16304321. Both of the AoE and GRF grants are issued by the Research Grants Council of Hong Kong SAR. L. L. is also supported by the DOE Grant No. DE-SC-0010010.

APPENDIX: RELEVANT OBSERVABLES IN LOW-ENERGY EFT

The LEFT predictions for the $b \to c\tau\nu$, $b \to s\tau^+\tau^-$, and $b \to s\bar{\nu}\nu$ observables have been analytically or semianalytically studied in literature. However, to apply them to the SMEFT interpretation performed in Sec. VII, we need these predictions to be numerically calculated in terms of the LEFT Wilson coefficients first. Below is a summary of the analytical formulas that we have used for such a calculation (a summary of the parameter values used for this purpose can be found in Table XVII), which include the ones for $R_{J/\psi}$, $R_{D_s^{(*)}}$, R_{Λ_c} and $\mathrm{BR}(B^+ \to K^+\tau^+\tau^-)$, $\mathrm{BR}(B^0 \to K^{*0}\tau^+\tau^-)$, $\mathrm{BR}(B_s \to \phi\tau^+\tau^-)$, and $\mathrm{BR}(B_s \to \tau^+\tau^-)$. Note, the numerical formulas for $\mathrm{BR}(B^+ \to K^+\bar{\nu}\nu)$, $\mathrm{BR}(B^0 \to K^{*0}\bar{\nu}\nu)$, and $\mathrm{BR}(B_s \to \phi\bar{\nu}\nu)$ have been presented in [29,70]. So we quote them directly in the main text.

TABLE XVII. Parameter values used for numerically calculating the $b \to c\tau\nu$, $b \to s\tau\tau$, and $b \to s\bar{\nu}\nu$ observables in the LEFT.

$\alpha(\mu_b)$	1/133 [33,91]	G_F	1.166×10^{-5} GeV^{-2} [92]
m_μ	0.1057 GeV [92]	m_{Λ_c}	2.286 GeV [92]
m_τ	1.777 GeV [92]	m_{K^+}	0.4937 GeV [92]
m_b	4.8 GeV [92]	m_{K^*}	0.8917 GeV [92]
m_c	1.67 GeV [92]	m_ϕ	1.019 GeV [92]
m_s	0.093 GeV [92]	τ_{B^0}	1.519 ps [92]
m_{B^0}	5.279 GeV [92]	τ_{B_s}	1.516 ps [92]
m_{B^+}	5.279 GeV [92]	τ_{B^+}	1.638 ps [92]
m_{B_c}	6.274 GeV [92]	$\lvert V_{tb}\rvert$	1.013 [92]
m_{B_s}	5.367 GeV [92]	$\lvert V_{ts}\rvert$	0.0388 [92]
m_{Λ_b}	5.620 GeV [92]	$\lvert V_{cs}\rvert$	0.987 [92]
$m_{J/\psi}$	3.097 GeV [92]	$C_7^\tau\vert_{\mathrm{SM}}$	−0.292 [79]
m_{D_s}	1.968 GeV [92]	$C_9^\tau\vert_{\mathrm{SM}}$	4.07 [79]
$m_{D_s^*}$	2.112 GeV [92]	$C_{10}^\tau\vert_{\mathrm{SM}}$	−4.31 [79]
f_{B_s}	0.234 GeV [93]	$C_L^\nu\vert_{\mathrm{SM}}$	−6.47 [70]

1. $R_{J/\psi}$ and $R_{D_s^*}$

$R_{J/\psi}$ and $R_{D_s^*}$ involve the decay of the b meson with a vector meson. Their calculations in the LEFT are essentially the same. Consider $R_{D_s^*}$ as an example. We have (following [1])

$$\begin{aligned}\frac{d\Gamma_{B_s\to D_s^*\tau\nu}}{dq^2} = {}& \frac{G_F^2|V_{cb}|^2}{192\pi^3 m_{B_s}^3} q^2\sqrt{\lambda(q^2)}\left(1-\frac{m_\tau^2}{q^2}\right)^2\left\{(|1+\delta C_{V_L}^\tau|^2+|C_{V_R}^\tau|^2)\left[\left(1+\frac{m_\tau^2}{2q^2}\right)(H_{V_+}^2+H_{V_-}^2+H_{V_0}^2)+\frac{3m_\tau^2}{2q^2}H_{V_t}^2\right]\right.\\
&-2\mathrm{Re}[(1+\delta C_{V_L}^\tau)C_{V_R}^{\tau*}]\left[\left(1+\frac{m_\tau^2}{2q^2}\right)(H_{V_+}^2+2H_{V_-}H_{V_0})+\frac{3m_\tau^2}{2q^2}H_{V_t}^2\right]+\frac{3}{2}|C_{S_L}^\tau-C_{S_R}^\tau|^2H_S^2\\
&+8|C_T^\tau|^2\left(1+\frac{2m_\tau^2}{q^2}\right)(H_{V_+}^2+H_{V_-}^2+H_{V_0}^2)+3\mathrm{Re}[(1+\delta C_{V_L}^\tau-C_{V_R}^\tau)(C_{S_L}^{\tau*}-C_{S_R}^{\tau*})]\frac{m_\tau}{\sqrt{q^2}}H_SH_{V_t}\\
&-12\mathrm{Re}[(1+\delta C_{V_L}^\tau)C_T^{\tau*}]\frac{m_\tau}{\sqrt{q^2}}(H_{V_+}H_{T_+}-H_{V_-}H_{T_-}+H_{V_0}H_{T_0})\\
&\left.+12\mathrm{Re}(C_{V_R}^\tau C_T^{\tau*})\frac{m_\tau}{\sqrt{q^2}}(H_{V_-}H_{T_+}-H_{V_+}H_{T_-}+H_{V_0}H_{T_0})\right\},\end{aligned} \tag{A1}$$

with

$$\lambda(q^2) = [(m_{B_s}-m_{D_s^*})^2-q^2][(m_{B_s}+m_{D_s^*})^2-q^2]. \tag{A2}$$

Here the H quantities are hadronic helicity amplitudes, given by

$$H_{V_\pm} = (m_{B_s} + m_{D_s^*})A_1 \mp \frac{\lambda}{m_{B_s} + m_{D_s^*}} V, \tag{A3}$$

$$H_{V_0} = \frac{m_{B_s} + m_{D_s^*}}{2m_{D_s^*}\sqrt{q^2}}\left[-(m_{B_s}^2 - m_{D_s^*}^2 - q^2)A_1 + \frac{\lambda}{(m_{B_s} + m_{D_s^*})^2}A_2\right], \tag{A4}$$

$$H_{V_t} = -\sqrt{\frac{\lambda}{q^2}}A_0, \tag{A5}$$

$$H_S = -\frac{\sqrt{\lambda}}{m_b + m_c}A_0, \tag{A6}$$

$$H_{T_\pm} = \frac{1}{\sqrt{q^2}}[\pm(m_{B_s}^2 - m_{D_s^*}^2)T_2 + \sqrt{\lambda}T_1], \tag{A7}$$

$$H_{T_0} = \frac{1}{2m_{D_s^*}}\left[-(m_{B_s}^2 + 3m_{D_s^*}^2 - q^2)T_2 + \frac{\lambda}{m_{B_s}^2 - m_{D_s^*}^2}T_3\right]. \tag{A8}$$

$A_{0,1,2}(q^2)$, $V(q^2)$, and $T_{1,2,3}(q^2)$ are form factors. With the convention of $\epsilon^{0123} = +1$, they parametrize the relevant hadronic matrix elements as

$$\langle D_s^*(k,\varepsilon)|\bar{c}\gamma^\mu b|B_s(p)\rangle = \frac{2iV(q^2)}{m_{B_s} + m_{D_s^*}}\epsilon^{\mu\nu\rho\sigma}\varepsilon_\nu^* p_\rho k_\sigma, \tag{A9}$$

$$\langle D_s^*(k,\varepsilon)|\bar{c}\gamma^\mu\gamma^5 b|B_s(p)\rangle = 2m_{D_s^*}A_0(q^2)\frac{\varepsilon^*\cdot q}{q^2}q^\mu + (m_{B_s} + m_{D_s^*})A_1(q^2)\left(\varepsilon^{*\mu} - \frac{\varepsilon^*\cdot q}{q^2}q^\mu\right) - A_2(q^2)\frac{\varepsilon^*\cdot q}{m_{B_s} + m_{D_s^*}}\left(p^\mu + k^\mu - \frac{m_{B_s}^2 - m_{D_s^*}^2}{q^2}q^\mu\right), \tag{A10}$$

$$\langle D_s^*(k,\varepsilon)|\bar{c}\sigma^{\mu\nu}q_\nu b|B_s(p)\rangle = 2T_1(q^2)\epsilon^{\mu\nu\rho\sigma}\varepsilon_\nu^* p_\rho k_\sigma, \tag{A11}$$

$$\langle D_s^*(k,\varepsilon)|\bar{c}\sigma^{\mu\nu}\gamma^5 q_\nu b|B_s(p)\rangle = -T_2(q^2)\left[(m_{B_s}^2 - m_{D_s^*}^2)\varepsilon^{*\mu} - (\varepsilon^*\cdot q)(p+k)^\mu\right] - T_3(q^2)(\varepsilon^*\cdot q)\left[q^\mu - \frac{q^2}{m_{B_s}^2 - m_{D_s^*}^2}(p+k)^\mu\right], \tag{A12}$$

where [1]

$$T_1(q^2) = \frac{m_b + m_c}{m_{B_s} + m_{D_s^*}}V(q^2), \tag{A13}$$

$$T_2(q^2) = \frac{m_b - m_c}{m_{B_s} - m_{D_s^*}}A_1(q^2), \tag{A14}$$

$$T_3(q^2) = -\frac{m_b - m_c}{q^2}\{m_{B_s}[A_1(q^2) - A_2(q^2)] + m_{D_s^*}[A_2(q^2) + A_1(q^2) - 2A_0(q^2)]\}. \tag{A15}$$

In our analysis, we take the formulas of $A_{0,1,2}(q^2)$ and $V(q^2)$ from [8,94] (and their counterparts in the $R_{J/\psi}$ analysis from [4,5]). With $\frac{d\Gamma_{B_s\to D_s^*\mu\nu}}{dq^2}$ being calculated by replacing m_τ with m_μ and turning off all Wilson coefficients, finally we have

$$R_{D_s^*} = \frac{\int_{m_\tau^2}^{q^2_{\max}} dq^2 d\Gamma_{B_s\to D_s^*\tau\nu}/dq^2}{\int_{m_\mu^2}^{q^2_{\max}} dq^2 d\Gamma_{B_s\to D_s^*\mu\nu}/dq^2}, \tag{A16}$$

with $q^2_{\max} = (m_{B_s} - m_{D_s^*})^2$.

2. R_{D_s}

R_{D_s} involves the decay of the b meson with a pseudoscalar meson. Following [1], we have

$$\frac{d\Gamma_{B_s\to D_s\tau\nu}}{dq^2}=\frac{G_F^2|V_{cb}|^2}{192\pi^3 m_{B_s}^3}q^2\sqrt{\lambda(q^2)}\left(1-\frac{m_\tau^2}{q^2}\right)^2\left\{|1+\delta C_{V_L}^\tau+C_{V_R}^\tau|^2\left[\left(1+\frac{m_\tau^2}{2q^2}\right)H_{V_0}^{s\,2}+\frac{3m_\tau^2}{2q^2}H_{V_t}^{s\,2}\right]+\frac{3}{2}|C_{S_L}^\tau+C_{S_R}^\tau|^2H_S^{s\,2}\right.$$
$$+8|C_T^\tau|^2\left(1+\frac{2m_\tau^2}{q^2}\right)H_T^{s\,2}+3\mathrm{Re}[(1+\delta C_{V_L}^\tau+C_{V_R}^\tau)(C_{S_L}^{\tau*}+C_{S_R}^{\tau*})]\frac{m_\tau}{\sqrt{q^2}}H_S^sH_{V_t}^s$$
$$\left.-12\mathrm{Re}[(1+\delta C_{V_L}^\tau+C_{V_R}^\tau)C_T^{\tau*}]\frac{m_\tau}{\sqrt{q^2}}H_T^sH_{V_0}^s\right\}. \tag{A17}$$

Here the hadronic helicity amplitudes ($H_{V_0}^s$, $H_{V_t}^s$, H_S^s, and H_T^s) are given by [95]

$$H_{V_0}^s=\sqrt{\frac{\lambda}{q^2}}F_1, \tag{A18}$$

$$H_{V_t}^s=\frac{m_{B_s}^2-m_{D_s}^2}{\sqrt{q^2}}F_0, \tag{A19}$$

$$H_S^s=\frac{m_{B_s}^2-m_{D_s}^2}{m_b-m_c}F_0, \tag{A20}$$

$$H_T^s=-\frac{\sqrt{\lambda}}{m_{B_s}+m_{D_s}}F_T. \tag{A21}$$

The form factors (F_0, F_1, and F_T) parametrize the relevant matrix elements as [94]

$$\langle D_s(k)|\bar{c}\gamma^\mu b|B_s(p)\rangle=\left[(p+k)^\mu-q^\mu\frac{m_{B_s}^2-m_{D_s}^2}{q^2}\right]F_1(q^2)+q^\mu\frac{m_{B_s}^2-m_{D_s}^2}{q^2}F_0(q^2), \tag{A22}$$

$$\langle D_s(k)|\bar{c}\sigma^{\mu\nu}b|B_s(p)\rangle=-\frac{2i(p^\mu k^\nu-p^\nu k^\mu)}{m_{B_s}+m_{D_s}}F_T(q^2), \tag{A23}$$

$$\langle D_s(k)|\bar{c}b|B_s(p)\rangle=\frac{m_{B_s}^2-m_{D_s}^2}{m_b-m_c}F_0(q^2), \tag{A24}$$

where $F_1(0)=F_0(0)$ has been taken to cancel the divergence at $q^2=0$. In our analysis, we take the formulas for these form factors from [8]. With $\frac{d\Gamma_{B_s\to D_s\mu\nu}}{dq^2}$ being calculated by replacing m_τ with m_μ and turning off all Wilson coefficients, finally we have

$$R_{D_s}=\frac{\int_{m_\tau^2}^{q^2_{\max}}dq^2\,d\Gamma_{B_s\to D_s\tau\nu}/dq^2}{\int_{m_\mu^2}^{q^2_{\max}}dq^2\,d\Gamma_{B_s\to D_s\mu\nu}/dq^2}, \tag{A25}$$

with $q^2_{\max}=(m_{B_s}-m_{D_s})^2$.

3. R_{Λ_c}

R_{Λ_c} involves baryonic decay of the b hadron. Following [14,17,18], we have

$$\frac{d\Gamma_{\Lambda_b\to\Lambda_c\tau\nu}}{dq^2}=\frac{G_F^2|V_{cb}|^2}{384\pi^3 m_{\Lambda_b}^3}q^2\sqrt{\lambda(q^2)}\left(1-\frac{m_\tau^2}{q^2}\right)^2\times\left[A_1+\frac{m_\tau^2}{2q^2}A_2+\frac{3}{2}A_3+\frac{3m_\tau}{\sqrt{q^2}}A_4+2\left(1+\frac{2m_\tau^2}{q^2}\right)A_5+\frac{6m_\tau}{\sqrt{q^2}}A_6\right], \tag{A26}$$

where $A_{1,2,3,4}$ are contributed by scalar and vector operators [14,17], A_5 is contributed by tensor operators, and A_6 is contributed by both [18]. Explicitly, these A terms are given by

$$A_1=|H_{1/2,0}|^2+|H_{-1/2,0}|^2+|H_{1/2,1}|^2+|H_{-1/2,-1}|^2, \tag{A27}$$

$$A_2=A_1+3|H_{1/2,t}|^2+3|H_{-1/2,t}|^2, \tag{A28}$$

$$A_3=|H_{1/2,0}^{SP}|^2+|H_{-1/2,0}^{SP}|^2, \tag{A29}$$

$$A_4=\mathrm{Re}(H_{1/2,t}H_{1/2,0}^{SP\,*}+H_{-1/2,t}H_{-1/2,0}^{SP\,*}), \tag{A30}$$

$$A_5=|H_{1/2,t,0}^{(T)1/2}+H_{1/2,-1,1}^{(T)1/2}|^2+|H_{-1/2,t,-1}^{(T)1/2}+H_{-1/2,-1,0}^{(T)1/2}|^2+|H_{1/2,0,1}^{(T)-1/2}+H_{1/2,t,1}^{(T)-1/2}|^2+|H_{-1/2,-1,1}^{(T)-1/2}+H_{-1/2,t,0}^{(T)-1/2}|^2, \tag{A31}$$

$$A_6=\mathrm{Re}[H_{1/2,0}^*(H_{1/2,-1,1}^{(T)1/2}+H_{1/2,t,0}^{(T)1/2})]+\mathrm{Re}[H_{1/2,1}^*(H_{1/2,0,1}^{(T)-1/2}+H_{1/2,t,1}^{(T)-1/2})]+\mathrm{Re}[H_{-1/2,0}^*(H_{-1/2,-1,1}^{(T)-1/2}+H_{-1/2,t,0}^{(T)-1/2})]+\mathrm{Re}[H_{-1/2,-1}^*(H_{-1/2,-1,0}^{(T)1/2}+H_{-1/2,t,-1}^{(T)1/2})], \tag{A32}$$

with $H_{\lambda_{\Lambda_c},\lambda_W}=H_{\lambda_{\Lambda_c},\lambda_W}^V-H_{\lambda_{\Lambda_c},\lambda_W}^A$ and $H_{\lambda_{\Lambda_c},\lambda_{\rm NP}}^{SP}=H_{\lambda_{\Lambda_c},\lambda_{\rm NP}}^S+H_{\lambda_{\Lambda_c},\lambda_{\rm NP}}^P$. Here $H_{\lambda_{\Lambda_c},\lambda_W}^{V(A)}$, $H_{\lambda_{\Lambda_c},\lambda_{\rm NP}}^{S(P)}$, and $H_{\lambda_{\Lambda_c},\lambda,\lambda'}^{(T)\lambda_{\Lambda_b}}$ denote the (axial-)vector, (pseudo)scalar, and tensor helicity amplitudes, respectively. They are characterized by the helicities

of Λ_b (λ_{Λ_b}), Λ_c (λ_{Λ_c}), intermediate off-shell W boson (λ_W),[7] and new-physics particle ($\lambda_{\rm NP}$), and the possible tensor degrees of freedom (λ and λ') together. These helicity amplitudes are then found to be

$$H^V_{1/2,0} = (1+\delta C^\tau_{V_L} + C^\tau_{V_R})\frac{\sqrt{Q_-}}{\sqrt{q^2}}[(m_{\Lambda_b}+m_{\Lambda_c})f_1 - q^2 f_2], \tag{A33}$$

$$H^A_{1/2,0} = (1+\delta C^\tau_{V_L} - C^\tau_{V_R})\frac{\sqrt{Q_+}}{\sqrt{q^2}}[(m_{\Lambda_b}-m_{\Lambda_c})g_1 + q^2 g_2], \tag{A34}$$

$$H^V_{1/2,1} = (1+\delta C^\tau_{V_L} + C^\tau_{V_R})\sqrt{2Q_-}[f_1 - (m_{\Lambda_b}+m_{\Lambda_c})f_2], \tag{A35}$$

$$H^A_{1/2,1} = (1+\delta C^\tau_{V_L} - C^\tau_{V_R})\sqrt{2Q_+}[g_1 + (m_{\Lambda_b}-m_{\Lambda_c})g_2], \tag{A36}$$

$$H^V_{1/2,t} = (1+\delta C^\tau_{V_L} + C^\tau_{V_R})\frac{\sqrt{Q_+}}{\sqrt{q^2}}[(m_{\Lambda_b}-m_{\Lambda_c})f_1 + q^2 f_3], \tag{A37}$$

$$H^A_{1/2,t} = (1+\delta C^\tau_{V_L} - C^\tau_{V_R})\frac{\sqrt{Q_-}}{\sqrt{q^2}}[(m_{\Lambda_b}+m_{\Lambda_c})g_1 - q^2 g_3], \tag{A38}$$

$$H^S_{1/2,0} = (C^\tau_{S_L} + C^\tau_{S_R})\frac{\sqrt{Q_+}}{m_b - m_c}[(m_{\Lambda_b}-m_{\Lambda_c})f_1 + q^2 f_3], \tag{A39}$$

$$H^P_{1/2,0} = (C^\tau_{S_L} - C^\tau_{S_R})\frac{\sqrt{Q_-}}{m_b + m_c}[(m_{\Lambda_b}+m_{\Lambda_c})g_1 - q^2 g_3], \tag{A40}$$

$$H^{(T)-1/2}_{-1/2,t,0} = C^\tau_T(h_+\sqrt{Q_-} - \tilde{h}_+\sqrt{Q_+}), \tag{A41}$$

$$H^{(T)1/2}_{1/2,t,0} = C^\tau_T(h_+\sqrt{Q_-} + \tilde{h}_+\sqrt{Q_+}), \tag{A42}$$

$$H^{(T)-1/2}_{1/2,t,1} = -C^\tau_T\frac{\sqrt{2}}{\sqrt{q^2}}\Big[h_\perp(m_{\Lambda_b}+m_{\Lambda_c})\sqrt{Q_-} + \tilde{h}_\perp(m_{\Lambda_b}-m_{\Lambda_c})\sqrt{Q_+}\Big], \tag{A43}$$

$$H^{(T)1/2}_{-1/2,t,-1} = -C^\tau_T\frac{\sqrt{2}}{\sqrt{q^2}}\Big[h_\perp(m_{\Lambda_b}+m_{\Lambda_c})\sqrt{Q_-} - \tilde{h}_\perp(m_{\Lambda_b}-m_{\Lambda_c})\sqrt{Q_+}\Big], \tag{A44}$$

$$H^{(T)-1/2}_{1/2,0,1} = H^{(T)-1/2}_{1/2,t,1}, \tag{A45}$$

$$H^{(T)1/2}_{-1/2,0,-1} = -H^{(T)1/2}_{-1/2,t,-1}, \tag{A46}$$

$$H^{(T)1/2}_{1/2,1,-1} = -H^{(T)1/2}_{1/2,t,0}, \tag{A47}$$

$$H^{(T)-1/2}_{-1/2,1,-1} = -H^{(T)-1/2}_{-1/2,t,0}, \tag{A48}$$

where $Q_\pm = (m_{\Lambda_b} \pm m_{\Lambda_c})^2 - q^2$. In addition, some useful properties on these helicity amplitudes have also been applied, including

$$H^V_{\lambda_{\Lambda_c},\lambda_W} = H^V_{-\lambda_{\Lambda_c},-\lambda_W}, \tag{A49}$$

$$H^A_{\lambda_{\Lambda_c},\lambda_W} = -H^A_{-\lambda_{\Lambda_c},-\lambda_W}, \tag{A50}$$

$$H^S_{\lambda_{\Lambda_c},\lambda_{\rm NP}} = H^S_{-\lambda_{\Lambda_c},-\lambda_{\rm NP}}, \tag{A51}$$

$$H^P_{\lambda_{\Lambda_c},\lambda_{\rm NP}} = -H^P_{-\lambda_{\Lambda_c},-\lambda_{\rm NP}}, \tag{A52}$$

$$H^{(T)\lambda_{\Lambda_b}}_{\lambda_{\Lambda_c},\lambda,\lambda'} = -H^{(T)\lambda_{\Lambda_b}}_{\lambda_{\Lambda_c},\lambda',\lambda}. \tag{A53}$$

As for the ten form factors introduced in these calculations, fs and gs parametrize the vector and axial vector matrix elements as [14]

$$\langle\Lambda_c|\bar{c}\gamma^\mu b|\Lambda_b\rangle = \bar{u}_{\Lambda_c}(f_1\gamma^\mu + if_2\sigma^{\mu\nu}q_\nu + f_3 q^\mu)u_{\Lambda_b}, \tag{A54}$$

$$\langle\Lambda_c|\bar{c}\gamma^\mu\gamma^5 b|\Lambda_b\rangle = \bar{u}_{\Lambda_c}(g_1\gamma^\mu + ig_2\sigma^{\mu\nu}q_\nu + g_3 q^\mu)\gamma^5 u_{\Lambda_b}, \tag{A55}$$

and the scalar and pseudoscalar matrix elements as

$$\langle\Lambda_c|\bar{c}b|\Lambda_b\rangle = \frac{1}{m_b - m_c}\bar{u}_{\Lambda_c}(f_1\not{q} + f_3 q^2)u_{\Lambda_b}, \tag{A56}$$

$$\langle\Lambda_c|\bar{c}\gamma^5 b|\Lambda_b\rangle = \frac{-1}{m_b + m_c}\bar{u}_{\Lambda_c}(g_1\not{q} + g_3 q^2)\gamma^5 u_{\Lambda_b}, \tag{A57}$$

while h_+, $h_\perp$, $\tilde{h}_+$, and $\tilde{h}_\perp$ parametrize the tensor matrix elements as [18]

[7] $\lambda_W = 0$ is allowed for both $J_W = 0$ and 1. Here J_W is the angular momentum of the W boson. To distinguish these two cases, we follow [15] and use $\lambda_W = t$ for the $J_W = 0$ case and $\lambda_W = 0$ for the $J_W = 1$ case.

$$\langle\Lambda_c|\bar{c}i\sigma^{\mu\nu}b|\Lambda_b\rangle = \bar{u}_{\Lambda_c}\Big\{2h_+\frac{p^\mu_{\Lambda_b}p^\nu_{\Lambda_c}-p^\nu_{\Lambda_b}p^\mu_{\Lambda_c}}{Q_+}+h_\perp\Big[\frac{m_{\Lambda_b}+m_{\Lambda_c}}{q^2}(q^\mu\gamma^\nu-q^\nu\gamma^\mu)-2\Big(\frac{1}{q^2}+\frac{1}{Q_+}\Big)(p^\mu_{\Lambda_b}p^\nu_{\Lambda_c}-p^\nu_{\Lambda_b}p^\mu_{\Lambda_c})\Big]$$
$$+\tilde{h}_+\Big\{i\sigma^{\mu\nu}-\frac{2}{Q_-}\Big[m_{\Lambda_b}(p^\mu_{\Lambda_c}\gamma^\nu-p^\nu_{\Lambda_c}\gamma^\mu)-m_{\Lambda_c}(p^\mu_{\Lambda_b}\gamma^\nu-p^\nu_{\Lambda_b}\gamma^\mu)+p^\mu_{\Lambda_b}p^\nu_{\Lambda_c}-p^\nu_{\Lambda_b}p^\mu_{\Lambda_c}\Big]\Big\}$$
$$+\tilde{h}_\perp\frac{m_{\Lambda_b}-m_{\Lambda_c}}{q^2Q_-}[(m^2_{\Lambda_b}-m^2_{\Lambda_c}-q^2)(\gamma^\mu p^\nu_{\Lambda_b}-\gamma^\nu p^\mu_{\Lambda_b})-(m^2_{\Lambda_b}-m^2_{\Lambda_c}+q^2)(\gamma^\mu p^\nu_{\Lambda_c}-\gamma^\nu p^\mu_{\Lambda_c})$$
$$+2(m_{\Lambda_b}-m_{\Lambda_c})(p^\mu_{\Lambda_b}p^\nu_{\Lambda_c}-p^\nu_{\Lambda_b}p^\mu_{\Lambda_c})]\Big\}u_{\Lambda_b} \tag{A58}$$

(the parametrization of $\langle\Lambda_c|\bar{c}i\sigma^{\mu\nu}\gamma^5 b|\Lambda_b\rangle$ can be found using the relation $2i\sigma^{\mu\nu}\gamma^5=\epsilon^{\mu\nu\alpha\beta}\sigma_{\alpha\beta}$). In our analysis, we take the formulas for the form factors fs and gs from [16] and the other four from [18,96]. With $d\Gamma_{\Lambda_b\to\Lambda_c\mu\nu}/dq^2$ being calculated by replacing m_τ with m_μ and turning off all Wilson coefficients, finally we have

$$R_{\Lambda_c}=\frac{\int_{m_\tau^2}^{q^2_{\max}}dq^2\ d\Gamma_{\Lambda_b\to\Lambda_c\tau\nu}/dq^2}{\int_{m_\mu^2}^{q^2_{\max}}dq^2\ d\Gamma_{\Lambda_b\to\Lambda_c\mu\nu}/dq^2}, \tag{A59}$$

with $q^2_{\max}=(m_{\Lambda_b}-m_{\Lambda_c})^2$.

4. $\mathbf{BR}(B^+\to K^+\tau^+\tau^-)$

$\mathrm{BR}(B^+\to K^+\tau^+\tau^-)$ involves the b-meson decay into a pseudoscalar meson. According to [91,93], we have

$$\frac{d\Gamma_{B^+\to K^+\tau^+\tau^-}}{dq^2}=\frac{G_F^2\alpha^2|V_{tb}V_{ts}^*|^2}{256\pi^5m^3_{B^+}}\sqrt{\lambda(q^2)}\beta_\tau\Big(A+\frac{1}{3}C\Big), \tag{A60}$$

where

$$\beta_\tau=\sqrt{1-4\frac{m_\tau^2}{q^2}}, \tag{A61}$$

$$A=q^2(\beta_\tau^2|F_S|^2+|F_P|^2)+\frac{\lambda}{4}(|F_A|^2+|F_V|^2)+4m_\tau^2m^2_{B^+}|F_A|^2+2m_\tau(m^2_{B^+}-m^2_{K^+}+q^2)\mathrm{Re}(F_PF_A^*), \tag{A62}$$

$$C=q^2(\beta_\tau^2|F_T|^2+|F_{T5}|^2)-\frac{\lambda\beta_\tau^2}{4}(|F_A|^2+|F_V|^2)+2m_\tau\sqrt{\lambda}\beta_\tau\mathrm{Re}(F_TF_V^*). \tag{A63}$$

Here $F(q^2)$'s are given by

$$F_V=(C_9^\tau|_{\mathrm{SM}}+\delta C_9^\tau+C_9'^\tau)f_+ +\frac{2m_b}{m_{B^+}+m_{K^+}}\Big(C_7^\tau|_{\mathrm{SM}}+\frac{4m_\tau}{m_b}C_T^\tau\Big)f_T, \tag{A64}$$

$$F_A=(C_{10}^\tau|_{\mathrm{SM}}+\delta C_{10}^\tau+C_{10}'^\tau)f_+, \tag{A65}$$

$$F_S=(C_S^\tau+C_S'^\tau)\frac{m^2_{B^+}-m^2_{K^+}}{2m_b}f_0, \tag{A66}$$

$$F_P=(C_P^\tau+C_P'^\tau)\frac{m^2_{B^+}-m^2_{K^+}}{2m_b}f_0 -m_\tau(C_{10}^\tau|_{\mathrm{SM}}+\delta C_{10}^\tau+C_{10}'^\tau)\times\Big[f_+-\frac{m^2_{B^+}-m^2_{K^+}}{q^2}(f_0-f_+)\Big], \tag{A67}$$

$$F_T=2C_T^\tau\frac{\beta_\tau\sqrt{\lambda}}{m_{B^+}+m_{K^+}}f_T, \tag{A68}$$

$$F_{T5}=2C_{T5}^\tau\frac{\beta_\tau\sqrt{\lambda}}{m_{B^+}+m_{K^+}}f_T. \tag{A69}$$

$f_{+,0,T}$ are form factors that parametrize the relevant matrix elements as

$$\langle K^+(k)|\bar{s}\gamma^\mu b|B^+(p)\rangle=\Big[(p+k)^\mu-q^\mu\frac{m^2_{B^+}-m^2_{K^+}}{q^2}\Big]f_+(q^2)+q^\mu\frac{m^2_{B^+}-m^2_{K^+}}{q^2}f_0(q^2), \tag{A70}$$

$$\langle K^+(k)|\bar{s}\sigma^{\mu\nu}b|B^+(p)\rangle=-\frac{2i(p^\mu k^\nu-p^\nu k^\mu)}{m_{B^+}+m_{K^+}}f_T(q^2). \tag{A71}$$

In this analysis their, lattice-QCD-based values are taken from [97]. The branching ratio is finally given by

$$\mathrm{BR}(B^+\to K^+\tau^+\tau^-)=\tau_{B^+}\int_{q^2_{\min}}^{q^2_{\max}}dq^2\ d\Gamma_{B^+\to K^+\tau^+\tau^-}/dq^2, \tag{A72}$$

where τ_{B^+} is the lifetime of B^+ and q^2 ranges from 15 GeV^2 to $(m_{B^+} - m_{K^+})^2$.

5. $\mathbf{BR}(B^0 \to K^{*0}\tau^+\tau^-)$ and $\mathbf{BR}(B_s \to \phi\tau^+\tau^-)$

$\mathrm{BR}(B^0 \to K^{*0}\tau^+\tau^-)$ and $\mathrm{BR}(B_s \to \phi\tau^+\tau^-)$ involve the decay of the b meson into a vector meson. Here we consider $\mathrm{BR}(B^0 \to K^{*0}\tau^+\tau^-)$ and the calculation of $\mathrm{BR}(B_s \to \phi\tau^+\tau^-)$ is similar. Following [98,99], we have

$$\frac{d\Gamma_{B^0\to K^{*0}\tau^+\tau^-}}{dq^2} = 2J_{1s} + J_{1c} - \frac{2J_{2s} + J_{2c}}{3}, \tag{A73}$$

where

$$\begin{aligned} J_{1s} = {} & \frac{3(2+\beta_\tau^2)}{16}(|A_\perp^L|^2 + |A_\parallel^L|^2 + |A_\perp^R|^2 + |A_\parallel^R|^2) + \frac{3m_\tau^2}{q^2}\mathrm{Re}(A_\perp^L A_\perp^{R*} + A_\parallel^L A_\parallel^{R*}) \\ & + 3\beta_\tau^2(|A_{0\perp}|^2 + |A_{0\parallel}|^2) + 3(4-3\beta_\tau^2)(|A_{t\perp}|^2 + |A_{t\parallel}|^2) \\ & + \frac{6\sqrt{2}m_\tau}{q^2}\mathrm{Re}[(A_\parallel^L + A_\parallel^R)A_{t\parallel}^* + (A_\perp^L + A_\perp^R)A_{t\perp}^*], \end{aligned} \tag{A74}$$

$$\begin{aligned} J_{1c} = {} & \frac{3}{4}(|A_0^L|^2 + |A_0^R|^2 + \beta_\tau^2|A_S|^2) + \frac{3m_\tau^2}{q^2}[|A_t|^2 + 2\mathrm{Re}(A_0^L A_0^{R*})] + 6(2-\beta_\tau^2)|A_{t0}|^2 \\ & + 6\beta_\tau^2|A_{\parallel\perp}|^2 + \frac{12m_\tau}{\sqrt{q^2}}\mathrm{Re}[(A_0^L + A_0^R)A_{t0}^*], \end{aligned} \tag{A75}$$

$$J_{2s} = \frac{3\beta_\tau^2}{16}(|A_\perp^L|^2 + |A_\parallel^L|^2 + |A_\perp^R|^2 + |A_\parallel^R|^2) - 3\beta_\tau^2(|A_{t\perp}|^2 + |A_{t\parallel}|^2 + |A_{0\perp}|^2 + |A_{0\parallel}|^2), \tag{A76}$$

$$J_{2c} = \frac{3\beta_\tau^2}{4}[8(|A_{t0}|^2 + |A_{\parallel\perp}|^2) - |A_0^L|^2 - |A_0^R|^2], \tag{A77}$$

with $\beta_\tau = \sqrt{1 - 4\frac{m_\tau^2}{q^2}}$. Here all A quantities are transversity amplitudes. They are given by

$$A_\perp^{L,R} = N\sqrt{2\lambda}\left\{[(C_9^\tau|_{\mathrm{SM}} + \delta C_9^\tau + C_9'^\tau) \mp (C_{10}^\tau|_{\mathrm{SM}} + \delta C_{10}^\tau + C_{10}'^\tau)]\frac{V}{m_{B^0} + m_{K^{*0}}} + \frac{2m_b}{q^2}(C_7^\tau + C_7'^\tau)T_1\right\}, \tag{A78}$$

$$A_\parallel^{L,R} = -N\sqrt{2}(m_{B^0}^2 - m_{K^{*0}}^2)\left\{[(C_9^\tau|_{\mathrm{SM}} + \delta C_9^\tau - C_9'^\tau) \mp (C_{10}^\tau|_{\mathrm{SM}} + \delta C_{10}^\tau - C_{10}'^\tau)]\frac{A_1}{m_{B^0} - m_{K^{*0}}} + \frac{2m_b}{q^2}(C_7^\tau - C_7'^\tau)T_2\right\}, \tag{A79}$$

$$\begin{aligned} A_0^{L,R} = {} & -\frac{N}{2m_{K^{*0}}\sqrt{q^2}}\left\{[(C_9^\tau|_{\mathrm{SM}} + \delta C_9^\tau - C_9'^\tau) \mp (C_{10}^\tau|_{\mathrm{SM}} + \delta C_{10}^\tau - C_{10}'^\tau)]\left[(m_{B^0}^2 - m_{K^{*0}}^2 - q^2)(m_{B^0} + m_{K^{*0}})A_1 - \frac{\lambda A_2}{m_{B^0} + m_{K^{*0}}}\right]\right. \\ & \left. + 2m_b(C_7^\tau - C_7'^\tau)\left[(m_{B^0}^2 + 3m_{K^{*0}}^2 - q^2)T_2 - \frac{\lambda T_3}{m_{B^0}^2 - m_{K^{*0}}^2}\right]\right\}, \end{aligned} \tag{A80}$$

$$A_t = N\frac{\sqrt{\lambda}}{\sqrt{q^2}}\left[2(C_{10}^\tau|_{\mathrm{SM}} + \delta C_{10}^\tau - C_{10}'^\tau) + \frac{q^2(C_P^\tau - C_P'^\tau)}{m_\tau m_b}\right]A_0, \tag{A81}$$

$$A_S = -2N\sqrt{\lambda}\frac{C_S^\tau - C_S'^\tau}{m_b}A_0, \tag{A82}$$

$$A_{\parallel\perp(t0)} = \pm N\frac{C_{T(5)}^\tau}{m_{K^{*0}}}\left[(m_{B^0}^2 + 3m_{K^{*0}}^2 - q^2)T_2 - \frac{\lambda T_3}{m_{B^0}^2 - m_{K^{*0}}^2}\right], \tag{A83}$$

$$A_{t\perp(0\perp)} = \pm 2N\frac{\sqrt{\lambda}}{\sqrt{q^2}}C_{T(5)}^\tau T_1, \tag{A84}$$

$$A_{0\|(t\|)} = \pm 2N \frac{m_{B^0}^2 - m_{K^{*0}}^2}{\sqrt{q^2}} C_{T(5)}^{\tau} T_2, \tag{A85}$$

with

$$N = G_F \alpha V_{tb} V_{ts}^* \sqrt{\frac{q^2 \beta_\tau \sqrt{\lambda}}{3072\pi^5 m_{B^0}^3}}, \tag{A86}$$

$$\lambda(q^2) = [(m_{B^0} - m_{K^{*0}})^2 - q^2][(m_{B^0} + m_{K^{*0}})^2 - q^2]. \tag{A87}$$

$A_{0,1,2}(q^2)$, $V(q^2)$, and $T_{1,2,3}(q^2)$ are form factors. They parametrize the relevant matrix elements as [100]

$$\langle K^{*0}(k,\varepsilon)|\bar{c}\gamma^\mu b|B^0(p)\rangle = \frac{2iV}{m_{B^0} + m_{K^{*0}}} \epsilon^{\mu\nu\rho\sigma} \varepsilon_\nu^* p_\rho k_\sigma, \tag{A88}$$

$$\begin{aligned}\langle K^{*0}(k,\varepsilon)|\bar{c}\gamma^\mu\gamma^5 b|B^0(p)\rangle = {} & 2m_{K^{*0}} A_0 \frac{\varepsilon^* \cdot q}{q^2} q^\mu + (m_{B^0} + m_{K^{*0}}) A_1 \left(\varepsilon^{*\mu} - \frac{\varepsilon^* \cdot q}{q^2} q^\mu\right) \\ & - A_2 \frac{\varepsilon^* \cdot q}{m_{B^0} + m_{K^{*0}}} \left(p^\mu + k^\mu - \frac{m_{B^0}^2 - m_{K^{*0}}^2}{q^2} q^\mu\right),\end{aligned} \tag{A89}$$

$$\langle K^{*0}(k,\varepsilon)|\bar{c}\sigma^{\mu\nu} q_\nu b|B^0(p)\rangle = 2T_1 \epsilon^{\mu\nu\rho\sigma} \varepsilon_\nu^* p_\rho k_\sigma, \tag{A90}$$

$$\langle K^{*0}(k,\varepsilon)|\bar{c}\sigma^{\mu\nu}\gamma^5 q_\nu b|B^0(p)\rangle = -T_2 \left[(m_{B^0}^2 - m_{K^{*0}}^2)\varepsilon^{*\mu} - (\varepsilon^* \cdot q)(p+k)^\mu\right] - T_3(\varepsilon^* \cdot q)\left[q^\mu - \frac{q^2}{m_{B^0}^2 - m_{K^{*0}}^2}(p+k)^\mu\right]. \tag{A91}$$

In this analysis, their lattice-QCD-based values are taken from [101]. We then have

$$\mathrm{BR}(B^0 \to K^{*0}\tau^+\tau^-) = \tau_{B^0} \int_{q_{\min}^2}^{q_{\max}^2} dq^2 \frac{d\Gamma_{B^0 \to K^{*0}\tau^+\tau^-}}{dq^2}. \tag{A92}$$

Here τ_{B^0} is the lifetime of B^0 and q^2 ranges from 15 GeV^2 to $(m_{B^0} - m_{K^{*0}})^2$.

6. BR($B_s \to \tau^+\tau^-$)

As studied in [93], BR($B_s \to \tau^+\tau^-$) is given by

$$\begin{aligned}\mathrm{BR}(B_s \to \tau^+\tau^-) = {} & \tau_{B_s} f_{B_s}^2 m_{B_s}^3 \frac{G_F^2 \alpha^2}{64\pi^3} |V_{tb} V_{ts}^*| \beta_\tau(m_{B_s}^2) \left[\frac{m_{B_s}^2}{m_b^2} |C_S^\tau - C_S^{\prime\tau}|^2 \left(1 - \frac{4m_\tau^2}{m_{B_s}^2}\right)\right. \\ & \left. + \left|\frac{m_{B_s}}{m_b}(C_P^\tau - C_P^{\prime\tau}) + \frac{2m_\tau}{m_{B_s}}(C_{10}^\tau - C_{10}^{\prime\tau})\right|^2\right].\end{aligned} \tag{A93}$$

Here f_{B_s} is a form factor parametrizing the hadronic matrix element

$$\langle 0|\bar{s}\gamma^\mu P_L b|B_s(p)\rangle = \frac{i}{2} f_{B_s} p^\mu, \tag{A94}$$

τ_{B_s} is the lifetime of B_s, and $\beta_\tau(q^2)$ is a function of q^2, defined as

$$\beta_\tau(q^2) = \sqrt{1 - \frac{4m_\tau^2}{q^2}}. \tag{A95}$$

[1] Y. Sakaki, M. Tanaka, A. Tayduganov, and R. Watanabe, Testing leptoquark models in $\bar{B} \to D^{(*)}\tau\bar{\nu}$, Phys. Rev. D **88**, 094012 (2013).

[2] X.-Q. Hu, S.-P. Jin, and Z.-J. Xiao, Semileptonic decays $B/B_s \to (D^{(*)}, D_s^{(*)})l\nu_l$ in the PQCD approach with the lattice QCD input, Chin. Phys. C **44**, 053102 (2020).

[3] HFLAV Collaboration, Averages of b-hadron, c-hadron, and τ-lepton properties as of 2018, Eur. Phys. J. C **81**, 226 (2021).

[4] W.-F. Wang, Y.-Y. Fan, and Z.-J. Xiao, Semileptonic decays $B_c \to (\eta_c, J/\Psi)l\nu$ in the perturbative QCD approach, Chin. Phys. C **37**, 093102 (2013).

[5] R. Watanabe, New physics effect on $B_c \to J/\psi\tau\bar{\nu}$ in relation to the $R_{D^{(*)}}$ anomaly, Phys. Lett. B **776**, 5 (2018).

[6] P. Asadi and D. Shih, Maximizing the impact of new physics in $b \to c\tau\nu$ anomalies, Phys. Rev. D **100**, 115013 (2019).

[7] LHCb Collaboration, Measurement of the ratio of branching fractions $\mathcal{B}(B_c^+ \to J/\psi\tau^+\nu_\tau)/\mathcal{B}(B_c^+ \to J/\psi\mu^+\nu_\mu)$, Phys. Rev. Lett. **120**, 121801 (2018).

[8] Y.-Y. Fan, W.-F. Wang, and Z.-J. Xiao, Study of $\bar{B}_s^0 \to (D_s^+, D_s^{*+})l^-\bar{\nu}_l$ decays in the pQCD factorization approach, Phys. Rev. D **89**, 014030 (2014).

[9] Y. Zhang, T. Zhong, H.-B. Fu, W. Cheng, L. Zeng, and X.-G. Wu, Ratio $R(D_s)$ for $B_s \to D_s\ell\nu_\ell$ by using the QCD light-cone sum rules within the framework of heavy quark effective field theory, Phys. Rev. D **105**, 096013 (2022).

[10] R. N. Faustov and V. O. Galkin, Weak decays of B_s mesons to D_s mesons in the relativistic quark model, Phys. Rev. D **87**, 034033 (2013).

[11] C. J. Monahan, H. Na, C. M. Bouchard, G. P. Lepage, and J. Shigemitsu, $B_s \to D_s\ell\nu$ form factors and the fragmentation fraction ratio f_s/f_d, Phys. Rev. D **95**, 114506 (2017).

[12] R. Dutta and N. Rajeev, Signature of lepton flavor universality violation in $B_s \to D_s\tau\nu$ semileptonic decays, Phys. Rev. D **97**, 095045 (2018).

[13] N. R. Soni, A. Issadykov, A. N. Gadaria, Z. Tyulemissov, J. J. Patel, and J. N. Pandya, Form factors and branching fraction calculations for $B_s \to D_s^{(*)}\ell^+\nu_\ell$ in view of LHCb observation, Eur. Phys. J. Plus **138**, 163 (2023).

[14] S. Shivashankara, W. Wu, and A. Datta, $\Lambda_b \to \Lambda_c\tau\bar{\nu}_\tau$ decay in the Standard Model and with new physics, Phys. Rev. D **91**, 115003 (2015).

[15] T. Gutsche, M. A. Ivanov, J. G. Körner, V. E. Lyubovitskij, P. Santorelli, and N. Habyl, Semileptonic decay $\Lambda_b \to \Lambda_c + \tau^- + \overline{\nu_\tau}$ in the covariant confined quark model, Phys. Rev. D **91**, 074001 (2015).

[16] W. Detmold, C. Lehner, and S. Meinel, $\Lambda_b \to p\ell^-\overline{\nu}_\ell$ and $\Lambda_b \to \Lambda_c\ell^-\bar{\nu}_\ell$ form factors from lattice QCD with relativistic heavy quarks, Phys. Rev. D **92**, 034503 (2015).

[17] R. Dutta, $\Lambda_b \to (\Lambda_c, p)\tau\nu$ decays within Standard Model and beyond, Phys. Rev. D **93**, 054003 (2016).

[18] A. Datta, S. Kamali, S. Meinel, and A. Rashed, Phenomenology of $\Lambda_b \to \Lambda_c\tau\bar{\nu}_\tau$ using lattice QCD calculations, J. High Energy Phys. 08 (**2017**) 131.

[19] LHCb Collaboration, Observation of the decay $\Lambda_b^0 \to \Lambda_c^+\tau^-\bar{\nu}_\tau$, Phys. Rev. Lett. **128**, 191803 (2022).

[20] CEPC Study Group Collaboration, CEPC conceptual design report: Volume 2—physics & detector, arXiv:1811.10545.

[21] FCC Collaboration, FCC-ee: The lepton collider: Future circular collider conceptual design report volume 2, Eur. Phys. J. Spec. Top. **228**, 261 (2019).

[22] LCC Physics Working Group Collaboration, Tests of the standard model at the international linear collider, arXiv:1908.11299.

[23] Belle-II Collaboration, The Belle II physics book, Prog. Theor. Exp. Phys. **2019**, 123C01 (2019).

[24] LHCb Collaboration, Physics case for an LHCb Upgrade II—Opportunities in flavour physics, and beyond, in the HL-LHC era, arXiv:1808.08865.

[25] Y. Wang, S. Descotes-Genon, O. Deschamps, L. Li, S. Chen, Y. Zhu, and M. Ruan, Prospects for $B_{(s)}^0 \to \pi^0\pi^0$ and $B_{(s)}^0 \to \eta\eta$ modes and corresponding CP asymmetries at Tera-Z, J. High Energy Phys. 12 (2022) 135.

[26] N. Berger, M. Kiehn, A. Kozlinskiy, and A. Schöning, A new three-dimensional track fit with multiple scattering, Nucl. Instrum. Methods Phys. Res., Sect. A **844**, 135 (2017).

[27] S. Descotes-Genon, I. Plakias, and O. Sumensari, On the impact of meson mixing on $B_s \to \phi ee$ angular observables at low q^2, J. High Energy Phys. 02 (2023) 096.

[28] S. Descotes-Genon, S. Fajfer, J. F. Kamenik, and M. Novoa-Brunet, Probing CP violation in exclusive $b \to s\nu\bar{\nu}$ transitions, Phys. Rev. D **107**, 013005 (2023).

[29] L. Li, M. Ruan, Y. Wang, and Y. Wang, Analysis of $B_s \to \phi\nu\bar{\nu}$ at CEPC, Phys. Rev. D **105**, 114036 (2022).

[30] X. Li, M. Ruan, and M. Zhao, Prospect for measurement of CP-violation phase ϕ_s study in the $B_s \to J/\Psi\phi$ channel at future Z factory, arXiv:2205.10565.

[31] R. Aleksan, L. Oliver, and E. Perez, CP violation and determination of the bs flat unitarity triangle at an FCC-ee, Phys. Rev. D **105**, 053008 (2022).

[32] R. Aleksan, L. Oliver, and E. Perez, Study of CP violation in $B^\pm$ decays to $\overline{D^0}(D^0)K^\pm$ at FCCee, arXiv:2107.05311.

[33] J. F. Kamenik, S. Monteil, A. Semkiv, and L. V. Silva, Lepton polarization asymmetries in rare semi-tauonic $b \to s$ exclusive decays at FCC-ee, Eur. Phys. J. C **77**, 701 (2017).

[34] S. Monteil and G. Wilkinson, Heavy-quark opportunities and challenges at FCC-ee, Eur. Phys. J. Plus **136**, 837 (2021).

[35] M. Chrzaszcz, R. G. Suarez, and S. Monteil, Hunt for rare processes and long-lived particles at FCC-ee, Eur. Phys. J. Plus **136**, 1056 (2021).

[36] Q. Qin, Q. Li, C.-D. Lü, F.-S. Yu, and S.-H. Zhou, Charged lepton flavor violating Higgs decays at future e^+e^- colliders, Eur. Phys. J. C **78**, 835 (2018).

[37] T. Li and M. A. Schmidt, Sensitivity of future lepton colliders to the search for charged lepton flavor violation, Phys. Rev. D **99**, 055038 (2019).

[38] L. Calibbi, X. Marcano, and J. Roy, Z lepton flavour violation as a probe for new physics at future e^+e^- colliders, Eur. Phys. J. C **81**, 1054 (2021).

[39] M. Dam, Tau-lepton physics at the FCC-ee circular e^+e^- collider, SciPost Phys. Proc. **1**, 041 (2019).

[40] D. Yu, M. Ruan, V. Boudry, H. Videau, J.-C. Brient, Z. Wu, Q. Ouyang, Y. Xu, and X. Chen, The measurement of the $H \to \tau\tau$ signal strength in the future e^+e^- Higgs factories, Eur. Phys. J. C **80**, 7 (2020).

[41] T. Zheng, J. Xu, L. Cao, D. Yu, W. Wang, S. Prell *et al.*, Analysis of $B_c \to \tau\nu_\tau$ at CEPC, arXiv:2007.08234.

[42] L. Li and T. Liu, $b \to s\tau^+\tau^-$ physics at future Z factories, J. High Energy Phys. 06 (**2021**) 064.

[43] Y. Amhis, M. Hartmann, C. Helsens, D. Hill, and O. Sumensari, Prospects for $B_c^+ \to \tau^+\nu_\tau$ at FCC-ee, J. High Energy Phys. 12 (2021) 133.

[44] LHCb Collaboration, Measurement of lepton universality parameters in $B^+ \to K^+\ell^+\ell^-$ and $B^0 \to K^{*0}\ell^+\ell^-$ decays, Phys. Rev. D **108**, 032002 (2023).

[45] A. Crivellin, D. Müller, and T. Ota, Simultaneous explanation of $R(D^{(*)})$ and $b \to s\mu^+\mu^{--}$: The last scalar leptoquarks standing, J. High Energy Phys. 09 (2017) 040.

[46] A. Crivellin, D. Müller, and F. Saturnino, Flavor phenomenology of the leptoquark singlet-triplet model, J. High Energy Phys. 06 (2020) 020.

[47] Particle Data Group, Review of particle physics, Prog. Theor. Exp. Phys. **2020**, 083C01 (2020).

[48] T. Sjostrand, S. Mrenna, and P. Z. Skands, A brief introduction to PYTHIA8.1, Comput. Phys. Commun. **178**, 852 (2008).

[49] S. Jadach, B. F. L. Ward, and Z. Was, Coherent exclusive exponentiation for precision Monte Carlo calculations, Phys. Rev. D **63**, 113009 (2001).

[50] S. Jadach, B. F. L. Ward, and Z. Was, The precision Monte Carlo event generator KK for two fermion final states in e^+e^- collisions, Comput. Phys. Commun. **130**, 260 (2000).

[51] W. Kilian, T. Ohl, and J. Reuter, WHIZARD: Simulating multi-particle processes at LHC and ILC, Eur. Phys. J. C **71**, 1742 (2011).

[52] DELPHES 3 Collaboration, DELPHES3, A modular framework for fast simulation of a generic collider experiment, J. High Energy Phys. 02 (**2014**) 057.

[53] C. Chen, X. Mo, M. Selvaggi, Q. Li, G. Li, M. Ruan *et al.*, Fast simulation of the CEPC detector with Delphes, arXiv:1712.09517.

[54] RD-FA Collaboration, IDEA: A detector concept for future leptonic colliders, Nuovo Cimento Soc. Ital. Fis. **43C**, 27 (2020).

[55] D. Yu, T. Zheng, and M. Ruan, Lepton identification performance in Jets at a future electron positron Higgs Z factory, J. Instrum. **16**, P06013 (2021).

[56] FCC Collaboration, FCC physics opportunities, Eur. Phys. J. C **79**, 474 (2019).

[57] LHCb Collaboration, Measurement of $|V_{cb}|$ with $B_s^0 \to D_s^{(*)-}\mu^+\nu_\mu$ decays, Phys. Rev. D **101**, 072004 (2020).

[58] LHCb Collaboration, Measurement of the shape of the $\Lambda_b^0 \to \Lambda_c^+\mu^-\bar{\nu}_\mu$ differential decay rate, Phys. Rev. D **96**, 112005 (2017).

[59] LHCb Collaboration, Measurement of $|V_{cb}|$ with $B_s^0 \to D_s^{(*)-}\mu^+\nu_\mu$ decays, Phys. Rev. D **101**, 072004 (2020).

[60] S. W. Bosch, M. Neubert, and G. Paz, Subleading shape functions in inclusive B decays, J. High Energy Phys. 11 (2004) 073.

[61] C.-H. Chang and Y.-Q. Chen, The production of B_c or $\bar{B}_c$ meson associated with two heavy quark jets in Z^0 boson decay, Phys. Rev. D **46**, 3845 (1992).

[62] M. Dasgupta and G. P. Salam, Event shapes in e^+e^- annihilation and deep inelastic scattering, J. Phys. G **30**, R143 (2004).

[63] A. Banfi, G. P. Salam, and G. Zanderighi, Phenomenology of event shapes at hadron colliders, J. High Energy Phys. 06 (2010) 038.

[64] L. Li, Y.-Y. Li, T. Liu, and S.-J. Xu, Learning physics at future e^-e^+ colliders with machine, J. High Energy Phys. 10 (2020) 018.

[65] G. C. Fox and S. Wolfram, Observables for the analysis of event shapes in e^+e^- annihilation and other processes, Phys. Rev. Lett. **41**, 1581 (1978).

[66] A. Ali, J. S. Lange, and S. Stone, Exotics: Heavy pentaquarks and tetraquarks, Prog. Part. Nucl. Phys. **97**, 123 (2017).

[67] Q. Qin and F.-S. Yu, Discovery potentials of double-charm tetraquarks, Chin. Phys. C **45**, 103106 (2021).

[68] X.-C. Zheng, C.-H. Chang, T.-F. Feng, and Z. Pan, NLO QCD corrections to $B_c(B*_c)$ production around the Z pole at an e^+e^- collider, Sci. China Phys. Mech. Astron. **61**, 031012 (2018).

[69] C.-H. Chang, X.-Y. Wang, and X.-G. Wu, BCVEGPY2.2: A newly upgraded version for hadronic production of the meson Bc and its excited states, Comput. Phys. Commun. **197**, 335 (2015).

[70] A. J. Buras, J. Girrbach-Noe, C. Niehoff, and D. M. Straub, $B \to K^{(*)}\nu\bar{\nu}$ decays in the standard model and beyond, J. High Energy Phys. 02 (**2015**) 184.

[71] A. Angelescu, D. Bečirević, D. A. Faroughy, and O. Sumensari, Closing the window on single leptoquark solutions to the B-physics anomalies, J. High Energy Phys. 10 (2018) 183.

[72] F. Feruglio, P. Paradisi, and O. Sumensari, Implications of scalar and tensor explanations of $R_{D^{(*)}}$, J. High Energy Phys. 11 (2018) 191.

[73] Q.-Y. Hu, X.-Q. Li, and Y.-D. Yang, $b \to c\tau\nu$ transitions in the standard model effective field theory, Eur. Phys. J. C **79**, 264 (2019).

[74] L. Alasfar, A. Azatov, J. de Blas, A. Paul, and M. Valli, B anomalies under the lens of electroweak precision, J. High Energy Phys. 12 (2020) 016.

[75] S. Fajfer, J. F. Kamenik, and M. Tammaro, Interplay of new physics effects in $(g-2)_\ell$ and $h \to \ell^+\ell^{--}$—lessons from SMEFT, J. High Energy Phys. 06 (2021) 099.

[76] C. Cornella, D. A. Faroughy, J. Fuentes-Martín, G. Isidori, and M. Neubert, Reading the footprints of the B-meson flavor anomalies, J. High Energy Phys. 08 (2021) 050.

[77] T. Zheng, J. Xu, L. Cao, D. Yu, W. Wang, S. Prell, Y.-K. E. Cheung, and M. Ruan, Analysis of $B_c \to \tau\nu_\tau$ at CEPC, Chin. Phys. C **45**, 023001 (2021).

[78] S. Bifani, S. Descotes-Genon, A. Romero Vidal, and M.-H. Schune, Review of lepton universality tests in B decays, J. Phys. G **46**, 023001 (2019).

[79] S. Descotes-Genon, D. Ghosh, J. Matias, and M. Ramon, Exploring new physics in the C7-C7' plane, J. High Energy Phys. 06 (2011) 099.

[80] B. Capdevila, A. Crivellin, S. Descotes-Genon, L. Hofer, and J. Matias, Searching for new physics with $b \to s\tau^+\tau^-$ processes, Phys. Rev. Lett. **120**, 181802 (2018).
[81] *BABAR* Collaboration, Search for $B^+ \to K^+\tau^+\tau^-$ at the *BABAR* experiment, Phys. Rev. Lett. **118**, 031802 (2017).
[82] LHCb Collaboration, Search for the decays $B_s^0 \to \tau^+\tau^-$ and $B^0 \to \tau^+\tau^-$, Phys. Rev. Lett. **118**, 251802 (2017).
[83] B. Grzadkowski, M. Iskrzynski, M. Misiak, and J. Rosiek, Dimension-six terms in the standard model Lagrangian, J. High Energy Phys. 10 (**2010**) 085.
[84] A. Azatov, D. Bardhan, D. Ghosh, F. Sgarlata, and E. Venturini, Anatomy of $b \to c\tau\nu$ anomalies, J. High Energy Phys. 11 (2018) 187.
[85] J. Aebischer, J. Kumar, and D. M. Straub, WILSON: A PYTHON package for the running and matching of Wilson coefficients above and below the electroweak scale, Eur. Phys. J. C **78**, 1026 (2018).
[86] D. Foreman-Mackey, D. W. Hogg, D. Lang, and J. Goodman, EMCEE: The MCMC hammer, Publ. Astron. Soc. Pac. **125**, 306 (2013).
[87] D. Foreman-Mackey, CORNER.PY: Scatterplot matrices in PYTHON, J. Open Source Software **1**, 24 (2016).
[88] C. Murgui, A. Peñuelas, M. Jung, and A. Pich, Global fit to $b \to c\tau\nu$ transitions, J. High Energy Phys. 09 (2019) 103.
[89] J. Aebischer, M. Fael, C. Greub, and J. Virto, B physics beyond the standard model at one loop: Complete renormalization group evolution below the electroweak scale, J. High Energy Phys. 09 (**2017**) 158.
[90] E. E. Jenkins, A. V. Manohar, and P. Stoffer, Low-energy effective field theory below the electroweak scale: Anomalous dimensions, J. High Energy Phys. 01 (2018) 084.
[91] C. Bobeth, G. Hiller, and G. Piranishvili, Angular distributions of $\bar{B} \to \bar{K}\ell^+\ell^-$ decays, J. High Energy Phys. 12 (2007) 040.
[92] Particle Data Group, Review of particle physics, Phys. Rev. D **98**, 030001 (2018).
[93] D. Becirevic, N. Kosnik, F. Mescia, and E. Schneider, Complementarity of the constraints on new physics from $B_s \to \mu^+\mu^-$ and from $B \to Kl^+l^-$ decays, Phys. Rev. D **86**, 034034 (2012).
[94] W. Wang, Y.-L. Shen, and C.-D. Lu, Covariant light-front approach for B_c transition form factors, Phys. Rev. D **79**, 054012 (2009).
[95] M. Tanaka and R. Watanabe, New physics in the weak interaction of $\bar{B} \to D^{(*)}\tau\bar{\nu}$, Phys. Rev. D **87**, 034028 (2013).
[96] W. Detmold and S. Meinel, $\Lambda_b \to \Lambda\ell^+\ell^-$ form factors, differential branching fraction, and angular observables from lattice QCD with relativistic b quarks, Phys. Rev. D **93**, 074501 (2016).
[97] J. A. Bailey *et al.*, $B \to Kl^+l^-$ decay form factors from three-flavor lattice QCD, Phys. Rev. D **93**, 025026 (2016).
[98] C. Bobeth, G. Hiller, and D. van Dyk, The benefits of $\bar{B} \to \bar{K}^*l^+l^-$ decays at low recoil, J. High Energy Phys. 07 (2010) 098.
[99] C. Bobeth, G. Hiller, and D. van Dyk, General analysis of $\bar{B} \to \bar{K}^{(*)}\ell^+\ell^-$ decays at low recoil, Phys. Rev. D **87**, 034016 (2013).
[100] R. R. Horgan, Z. Liu, S. Meinel, and M. Wingate, Lattice QCD calculation of form factors describing the rare decays $B \to K^*\ell^+\ell^-$ and $B_s \to \phi\ell^+\ell^-$, Phys. Rev. D **89**, 094501 (2014).
[101] R. R. Horgan, Z. Liu, S. Meinel, and M. Wingate, Rare B decays using lattice QCD form factors, Proc. Sci. LATTICE2014 (**2015**) 372 [arXiv:1501.00367].